

Z-SCHEME $\text{BaFe}_2\text{O}_4/\text{BiOCl}$ HETEROJUNCTION
COMPOSITES FOR PHOTOCATALYTIC PALM
OIL MILL EFFLUENT DEGRADATION AND
BACTERIA INACTIVATION

TAN JIN HAN

MASTER OF ENGINEERING SCIENCE

FACULTY OF ENGINEERING AND GREEN
TECHNOLOGY
UNIVERSITI TUNKU ABDUL RAHMAN
NOV 2023

**Z-SCHEME BaFe₂O₄/BiOCl HETEROJUNCTION COMPOSITES FOR
PHOTOCATALYTIC PALM OIL MILL EFFLUENT DEGRADATION
AND BACTERIA INACTIVATION**

By
TAN JIN HAN

A thesis submitted to the Faculty of Engineering and Green Technology,
Universiti Tunku Abdul Rahman,
in partial fulfillment of the requirements for the degree of
Master of Engineering Science
NOV 2023

Z-SCHEME BaFe₂O₄/BiOCl HETEROJUNCTION COMPOSITES FOR PHOTOCATALYTIC PALM OIL MILL EFFLUENT DEGRADATION AND BACTERIA INACTIVATION

ABSTRACT

In recent years, organic pollution and biological hazards have become indisputable considerable environmental issues. Such as a raising POME production led by the surging demand and supply of palm oil. Semiconductor-based photocatalysis has been regarded as a promising and sustainable solution in minimizing the negative impacts of these matters. Therefore, a two-step precipitation-hydrothermal method was employed to fabricate novel Z-scheme BaFe₂O₄/BiOCl composites as efficient visible light-driven photocatalysts. The physicochemical properties and morphological characteristics of the fabricated composites were investigated via XRD, FTIR, FESEM, EDX, TEM, XPS, VSM, UV-vis DRS, Mott-Schottky, TPR, EIS and specific surface area characterization methods. The XRD spectra shown BiOCl as tetragonal structure, while additional diffraction peak is from the orthorhombic structure of BaFe₂O₄ in the composite. While the FTIR spectra of BaFe₂O₄/BiOCl composite, it demonstrated that the characteristic peaks of BaFe₂O₄ and BiOCl occurs simultaneously. The FESEM displayed that the 5 wt% BaFe₂O₄/BiOCl shows the aggregated BaFe₂O₄ particles cover the surface of sheet structure BiOCl to form a tightly contacted heterostructure while EDX analysis confirmed the successful synthesis of 5 wt% BaFe₂O₄/BiOCl composite. Whereas the TEM images displayed the lattice fringes in the 5 wt%

BaFe₂O₄/BiOCl corresponded to the (110) plane of BiOCl and the (212) plane of BaFe₂O₄, with spacings of 0.275 nm and 0.334 nm, respectively. In addition, the XPS findings further validated the coexistence of BiOCl and BaFe₂O₄ within composite, agreeing well with the XRD, FTIR and EDX findings. Via a VSM analysis, the composite demonstrated a symmetrical S-shaped of magnetization curve, revealing the ferromagnetic behavior of the 5 wt% BaFe₂O₄/BiOCl. The BiOCl nanosheets loaded with 5 wt% BaFe₂O₄ particles (5 wt% BaFe₂O₄/BiOCl) demonstrated the best visible light photoactivity with a palm oil mill effluent (POME) decomposition efficiency of 61% within 210 min. The photocatalytic enhancement benefited from the creation of Z-scheme heterojunction coupling BaFe₂O₄ with BiOCl, hence accelerating the interfacial charge transfer and maintaining strong redox potential for active radical generation. We also studied the operating parameter such as photocatalyst loading, solution pH and initial POME concentration and the optimum parameter discovered is 0.5 g/L of photocatalyst loading, 50 ppm of POME and solution pH of 2. Moreover, by regulating the pH value of photoreaction system, more superior POME degradation efficiency was attained and reached 85% at the same duration. With the assist of H₂O₂, the POME decomposition was greatly improved and reached 98% with a rate constant of 0.222 min⁻¹ in the same duration. Interestingly, the 5 wt% BaFe₂O₄/BiOCl composite also possessed a convenient catalyst separation along with good recyclability with only 7% loss in efficiency after four successive runs. Additionally, the band structure of 5 wt% BaFe₂O₄/BiOCl was evaluated using UV-vis DRS, and Mottschottky analysis. The TPR and EIS shown that the 5 wt% BaFe₂O₄/BiOCl with enhanced separation of photoexcited carriers. Based on the active species

scavenging experiment, superoxide radical was found as the eminent active species during the POME treatment. On the other hand, we used the Langmuir-Hinshelwood model to study the kinetics of photocatalytic degradation of POME over the as-synthesized products, finding that the photocatalytic reactions of POME conformed to the pseudo-first-order kinetics of Langmuir-Hinshelwood model, with the highest apparent rate constant determined to be 0.0222 corresponding to 3 mmol/L of H₂O₂ concentration. In addition, the electrical energy consumption per order was determined with value of 54.54 kWh/m³ order with the operation cost of RM 23.83 per m³ order. Phytotoxicity tests showed that the POME exhibited reduced phytotoxicity from 85% to 78% after undergoing photodecomposition, with longer radical length observed than before degradation. In addition to the investigation of POME treatment, the fabricated 5 wt% BaFe₂O₄/BiOCl composite was also successfully employed to inactivate the *E. coli* and *B. cereus*. This study revealed that the as-fabricated BaFe₂O₄/BiOCl composite had great potential applications to degrade various organics and to inactivate bacteria from wastewater.

ACKNOWLEDGEMENTS

I would like to express my sincere gratitude to all those who have supported and assisted me throughout my research project. I am particularly grateful to my research supervisor, Dr. Sin Jin Chung, for his unwavering guidance and motivation throughout the entire process. His encouragement were a constant source of inspiration during moments of difficulty. I would also like to extend my appreciation to Dr. Lam Sze Mun for her support.

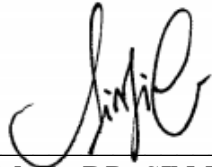
I am deeply indebted to Universiti Tunku Abdul Rahman (UTAR), specifically the Faculty of Engineering and Green Technology, for providing me with the necessary financial and academic resources to conduct my research. I would like to express my heartfelt thanks to all the lab officers who tirelessly supported and ensured my safety during my research, especially during my bacterial works.

Lastly, I would like to acknowledge my family and friends for their unwavering support throughout this research project. I would like to thank Chin Ying Hui, Jeffrey Yong Zi Jun, Janice Liew, Zhao Liang, Choong Mun Kit, Wong Yi Hang, Tan Sin Ying, Soo Pei Ling, Wong Rou Hui and Tanveer for their invaluable assistance, including delivering precious experiences in handling equipment, and providing joy and support during difficult moments. As the famous saying goes, "We often get so focused on the destination that we forget to appreciate the journey, especially the people we meet along the way." I am grateful for all the amazing people who have been a part of my journey.

APPROVAL SHEET

This thesis entitled "Z-SCHEME BaFe₂O₄/BiOCl HETEROJUNCTION COMPOSITES FOR PHOTOCATALYTIC PALM OIL MILL EFFLUENT DEGRADATION AND BACTERIA INACTIVATION" was prepared by TAN JIN HAN and submitted as partial fulfillment of the requirements for the degree of Master of Engineering Science at Universiti Tunku Abdul Rahman.

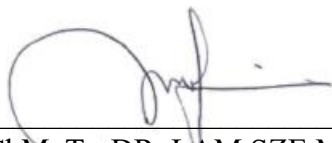
Approved by:



(ChM. Ts. DR. SIN JIN CHUNG)

Date: 21-11-2023

Supervisor
Department of Petrochemical Engineering
Faculty of Engineering and Green Technology
Universiti Tunku Abdul Rahman



(ChM. Ts. DR. LAM SZE MUN)

Date: 21-11-2023

Co-supervisor
Department of Environmental Engineering
Faculty of Engineering and Green Technology
Universiti Tunku Abdul Rahman

FACULTY OF ENGINEERING AND GREEN TECHNOLOGY

UNIVERSITI TUNKU ABDUL RAHMAN

Date: 21-11-2023

SUBMISSION OF THESIS

It is hereby certified that **TAN JIN HAN** (ID No: **20AGM05443**) has completed this thesis is entitled “Z-SCHEME BaFe₂O₄/BiOCl HETEROJUNCTION COMPOSITES FOR PHOTOCATALYTIC PALM OIL MILL EFFLUENT DEGRADATION AND BACTERIA INACTIVATION” under the supervision of ChM. Ts. DR. SIN JIN CHUNG (Supervisor) from the Department of Petrochemical Engineering, Faculty of Engineering and Green Technology, and ChM. Ts. DR. LAM SZE MUN (Co-Supervisor) from the Department of Environmental Engineering, Faculty of Engineering and Green Technology.

I understand that University will upload softcopy of my thesis in pdf format into UTAR Institutional Repository, which may be made accessible to UTAR community and public.

Yours truly,



(TAN JIN HAN)

DECLARATION

I, Tan Jin Han hereby declare that the thesis is based on my original work except for quotations and citations which have been duly acknowledged. I also declare that it has not been previously or concurrently submitted for any other degree at UTAR or other institutions.



(TAN JIN HAN)

Date 21-11-2023

TABLE OF CONTENTS

	Page
ABSTRACT	ii
ACKNOWLEDGEMENT	v
APPROVAL SHEET	vi
SUBMISSION SHEET	vii
DECLARATION SHEET	viii
TABLE OF CONTENTS	ix
LIST OF TABLES	xiv
LIST OF FIGURES	xv
LIST OF SYMBOLS	xvii
LIST OF ABBREVIATIONS	xviii
CHAPTERS	
1. INTRODUCTION	1
1.1 Background of Study	1
1.2 Problem Statement	3
1.3 Objectives	6
1.4 Scope of Study	7
1.5 Organization of Thesis	8
2. LITERATURE REVIEW	11
2.1 Palm Oil Mill Effluent (POME)	11
2.1.1 Origin of POME	12
2.1.2 Characteristics of POME	12
2.1.3 Conventional Treatment of POME	14

2.1.4	Polishing Processes of Treated POME	17
2.2	Advanced Oxidation Processes (AOPs)	19
2.3	Photocatalysis	21
2.3.1	BiOCl As A Photocatalyst	25
2.3.2	Z-scheme Heterojunction Photocatalyst	27
2.3.3	Barium Spinel Ferrite, BaFe ₂ O ₄	30
2.4	Photocatalytic Pre-Treated POME Treatment	33
2.5	Operating parameter studies	34
2.5.1	Photocatalyst loading	35
2.5.2	Solution pH	39
2.5.3	Initial Contaminant Concentration	43
2.6	Influence of H ₂ O ₂ Introduction	47
2.7	Photocatalytic Inactivation on Microorganism	52
2.8	Summary of Literature Review	56
3.	Methodology	57
3.1	Flowchart	57
3.2	Materials and Chemical Listing	58
3.3	Photocatalysis Experiment Setup	60
3.4	Preparation of Photocatalysts	62
3.4.1	Preparation of BaFe ₂ O ₄	62
3.4.2	Preparation of BaFe ₂ O ₄ /BiOCl and BiOCl	63
3.5	Characterization of as-prepared photocatalysts	64
3.5.1	X-ray Diffraction (XRD)	64
3.5.2	Fourier Transform Infrared Reflectance (FTIR)	65

3.5.3	Field Emission Scanning Electron Microscopy (FESEM) and Energy Dispersive X-ray (EDX)	65
3.5.4	Transmission Electron Microscopy (TEM)	66
3.5.5	X-ray Photoelectron Spectroscopy (XPS)	67
3.5.6	Vibrating Sample Magnetometer (VSM)	68
3.5.7	Zeta Potential Measurement	68
3.5.8	Ultraviolet-Visible Diffuse Reflectance Spectroscopy (UV-vis DRS)	69
3.5.9	Photoelectrochemical experiments	69
3.5.10	Specific Surface Area (SSA)	70
3.5.11	Mott-Schottky	70
3.6	Photocatalytic Pre-Treat POME Treatment Under Visible Light Irradiation and Sunlight	71
3.6.1	Effect of BaFe ₂ O ₄ Loading	72
3.6.2	Effect of Photocatalyst Loading	73
3.6.3	Effect of Solution pH	73
3.6.4	Effect of Initial POME Concentration	73
3.6.5	Photocatalyst Reusability	74
3.6.6	Effect of H ₂ O ₂ Addition	74
3.6.7	Screening of Reactive Oxygen Species (ROS)	74
3.7	Phytotoxicity	75
3.8	Photocatalytic Antibacterial Experiment	76
4.	RESULT AND DISCUSSION	77
4.1	Characterization Studies Of Developed Photocatalysis	78
4.1.1	XRD Characterization	78

4.1.2	FTIR Examination	79
4.1.3	FESEM, TEM and EDX Analyses	81
4.1.4	XPS Investigation	83
4.1.5	VSM ANALYSIS	85
4.2	Photocatalytic Pre-Treated POME Treatment	86
4.2.1	Screening of As-Synthesized Photocatalysts Over Pre-Treated POME Decomposition.	86
4.2.2	Effect of Photocatalyst Loading	88
4.2.3	Effect of solution pH	91
4.2.4	Effect of Initial Pre-treated POME Concentration	93
4.3	Photocatalyst Recyclability And Phytotoxicity Studies	96
4.4	The Role of H ₂ O ₂ As Electron Acceptor in Photocatalytic POME Treatment	99
4.5	Kinetic Study	102
4.5.1	Determination of Kinetic Model	102
4.5.2	Langmuir-Hinshelwood Model	105
4.6	Electrical Energy Consumption	108
4.7	Photocatalytic Activity Under Sunlight Irradiation	110
4.8	Photocatalytic Mechanism	113
4.8.1	UV-vis DRS and Mott-Schottky Analyses	113
4.8.2	Photoelectrochemical Analyses	115
4.8.3	SSA Analysis	116
4.8.4	Active Species Detection	118
4.8.5	Photocatalytic Enhancement Mechanism of BaFe ₂ O ₄ /BiOCl Composite	120

4.9 Antibacterial Activity	123
5. CONCLUSION AND RECOMMENDATION	126
5.1 Conclusion	126
5.2 Recommendation	128
REFERENCES	129
APPENDIX	156
LIST OF PUBLICATIONS	157

LIST OF TABLES

Table		Page
2.1	General properties of untreated POME in palm oil mills	13
2.2	Regulatory discharge limit for POME in Malaysia	15
2.3	Redox potential for selected generic oxidants in AOPs	22
2.4	List of pollutants decomposed during photocatalysis.	23
2.5	Photocatalytic decomposition efficiency of various pollutants based on different photocatalyst loadings	36
2.6	Influence of solution pH on photocatalytic decomposition efficiency of various pollutant using different photocatalytic	40
2.7	Effect of pollutant initial contaminant concentration on the photocatalytic decomposition of various organic pollutant	45
2.8	Effect of hydrogen peroxide dosage on the photocatalytic decomposition performance pollutant	50
2.9	Brief comparison of organic pollutants and microorganism inactivation over difference Bi-Based photocatalysts.	55
3.1	List of Chemicals Utilized	58
4.1	Reaction order with their relative rate law and integrated equation.	103
4.2	The rate constant and their corresponding determination coefficient obtained from reaction order plotting graphs.	105
4.3	Electrical energy consumption estimation using LED light as light source.	109

LIST OF FIGURES

Figure		Page
3.1	Flowchart of involved research methods in this study	57
3.2	Schematic diagram of photocatalytic system under visible light irradiation	61
3.3	Schematic diagram of photocatalytic system under sunlight irradiation	62
3.4	Schematic illustration of the synthesis path for BaFe ₂ O ₄ /BiOCl composite preparation.	64
4.1	XRD patterns of BiOCl, BaFe ₂ O ₄ and 5 wt% BiOCl/BaFe ₂ O ₄ composite.	79
4.2	FTIR spectra of BiOCl, BaFe ₂ O ₄ and 5 wt% BiOCl/BaFe ₂ O ₄ composite.	80
4.3	FESEM images of (a) BaFe ₂ O ₄ , (b) BiOCl and (c) 5 wt% BiOCl/BaFe ₂ O ₄ composite. (d) TEM image, (e) HRTEM image and (f) EDX spectrum of 5 wt% BiOCl/BaFe ₂ O ₄ composite. Inset of (f) is the EDX mapping images of 5 wt% BiOCl/BaFe ₂ O ₄ composite.	82
4.4	XPS spectra of (a) Bi 4f, (b) Cl 2p, (c) O 1s, (d) Ba 3d and (e) Fe 2p in 5 wt% BaFe ₂ O ₄ /BiOCl.	84
4.5	Magnetization curves of 5 wt% BaFe ₂ O ₄ /BiOCl composite. Inset is the image for the separation of the composite using a magnet.	85
4.6	Photocatalytic pre-treated POME treatment over different photocatalysts ([pre-treated POME] = 50 mg/L; photocatalyst loading = 0.5 g/L; solution pH = 7).	88
4.7	Effects of 5 wt% BiOCl/BaFe ₂ O ₄ loading ([pre-treated POME] = 50 mg/L; solution pH = 7) on pre-treated POME treatment.	89
4.8	(a) Effects of solution pH with 5 wt% BiOCl/BaFe ₂ O ₄ ([pre-treated POME] = 50 mg/L; photocatalyst loading = 0.5 g/L) on the pre-treated POME treatment; (b) Zeta potential measurement plot for 5 wt% BaFe ₂ O ₄ /BiOCl.	92
4.9	Photocatalytic decomposition performance of different initial pre-treated POME concentration (ppm) under	94

	(photocatalyst loading = 0.5 g/L; solution pH = 2) on the pre-treated POME treatment.	
4.10	(a) Cyclic use of 5 wt% BaFe ₂ O ₄ /BiOCl for four successive runs under (photocatalyst loading = 0.5 g/L; solution pH = 2; [pre-treat POME] = 50 ppm) on the pre-treated POME treatment; (b) Phytotoxicity of pre-treated POME before and after the 5 wt% BaFe ₂ O ₄ /BiOCl photocatalysis.	98
4.11	Photocatalytic decomposition of pre-treated POME at optimal conditions with different concentration of H ₂ O ₂ .	100
4.12	Plot of (a) zero order reaction, (b) first order reaction, (c) second order reaction, and (d) third order reaction. Conditions: BaFe ₂ O ₄ /BiOCl loading= 0.5 g/L; pre-treated POME concentration = 50 ppm, solution pH= 2.0 and H ₂ O ₂ concentration= 3.0 mmol/L.	104
4.13	Kinetic profile for photodecomposition of pre-treated POME with different H ₂ O ₂ concentration.	107
4.14	Photocatalytic decomposition of pre-treated POME under sunlight irradiation with conditions: (Photocatalyst loading = 0.5 g/L, solution pH = 2.0, pre-treated POME concentration = 50 ppm and H ₂ O ₂ concentration = 3 mmol/L)	111
4.15	(a) UV–vis DRS spectra of BiOCl, BaFe ₂ O ₄ and 5 wt% BiOCl/ BaFe ₂ O ₄ composite. Tauc plots of (b) BiOCl and (c) BaFe ₂ O ₄ . (d) Mott-Schottky analysis of BiOCl and BaFe ₂ O ₄ .	114
4.16	(a) Transient photocurrent response curves and (b) EIS spectra of as-synthesized samples.	116
4.17	Nitrogen adsorption-desorption isotherms of pristine BiOCl, BaFe ₂ O ₄ and 5 wt% BaFe ₂ O ₄ /BiOCl composite.	117
4.18	Photocatalytic pre-treated POME treatment over 5 wt% BaFe ₂ O ₄ /BiOCl in the presence of different scavengers.	119
4.19	Plausible photocatalytic mechanism of BiOCl/BaFe ₂ O ₄ composite.	122
4.20	Inhibition zones of BiOCl, BaFe ₂ O ₄ and 5 wt% BaFe ₂ O ₄ /BiOCl composite towards <i>E. coli</i> and <i>B. cereus</i> on the agar plates.	124

LIST OF SYMBOLS

Symbol	Description	Unit
C_P	Concentration of pre-treated POME at reaction time t	ppm
C_{P0}	initial concentration of pre-treated POME	ppm
E_{EO}	Energy consumption per cubic meter	kWh/m ³ ·order
E_g	Band gap energy	eV
E_{VB}	Valence band energy	eV
E_{CB}	Conduction band energy	eV
$h\nu$	Activation energy	eV
k	Rate constant	L/min
K_{app}	apparent rate constant	mg/L·min
P	Power consumed by LED	kWh
$-r$	Rate of reaction	-
R_C	Radicle length of control	cm
R_S	Radicle length of samples	cm
S	Cost of electricity	RM/m ³ ·order
t	reaction time	min
V	Volume of the solution	L

LIST OF ABBREVIATIONS

AgNbO ₃	Silver niobate
•OH	Hydroxyl radicals
e_{CB}^-	Photoexcited electron at conduction band
h_{VB}^+	Photoexcited hole at valence band
•OOH	Hydroperoxyl radicals
AOPs	Advanced oxidation processes
Au	Gold
<i>B. anthracis</i>	<i>Bacillus anthracis</i>
<i>B. cereus</i>	<i>Bacillus cereus</i>
<i>B. cytotoxicus</i>	<i>Bacillus cytotoxicus</i>
<i>B. mycoides</i>	<i>Bacillus mycoides</i>
<i>B. toyonensis</i>	<i>Bacillus toyonensis</i>
Ba(NO ₃) ₂	Barium nitrate
BaFe ₂ O ₄	Barium ferrite
BiOBr	Bismuth oxybromide
BiOCl	Bismuth oxychloride
BiVO ₄	Bismuth vanadium oxide
BOD	Biological oxygen demand
BQ	p-benzoquinone
CB	Conduction band
CdS	Cadmium sulphide
CeO ₂	Cerium(IV) oxide
CeVO ₄	Cerium orthovanadate

CIP	Ciprofloxacin
CO ₂	Carbon dioxide
COD	Chemical oxygen demand
CPO	Crude palm oil
CQDs	Carbon quantum dots
CuO	Copper oxide
CuONs	Copper oxide nanostructures
DNA	Deoxyribonucleic acid
DOE	Department of environment
<i>E. coli</i>	<i>Escherichia coli</i>
EDTA-2Na	Ethylenediaminetetraacetic acid sodium salt
EDX	Energy dispersive X-ray
EEC	Electrical energy consumption
EIS	Electrochemical impedance spectra
EQA	Environmental quality act
Fe ₃ O ₄	Iron (II, III) oxide
FESEM	Field-emission scanning electron microscopy
FeTiO ₃	Iron metatitanate
FFB	Fresh fruit bunches
FSZr	Fibrous silica zirconia
FTIR	Fourier transform infrared
g-C ₃ N ₄	Graphitic carbon nitride
GO	Graphene oxide
H ₂ O	Water
H ₂ O ₂	Hydrogen peroxide

IPA	Isopropanol
KCl	Potassium chloride
K-M	Kubelka Munk
KOH	Potassium hydroxide
LED	Light emitting diode
L-H	Langmuir Hinshelwood
Mg	Magnesium
Mn	Manganese
MO	Methyl Orange
MoS ₂	Molybdenum disulfide
MPOB	Malaysian palm oil board
MPOC	Malaysian palm oil council
MSPO	Malaysian sustainable palm oil
Na ₂ CO ₃	Sodium carbonate
Na ₂ S ₂ O ₈	Sodium persulfate
NaCl	Sodium chloride
NaNBO ₃	Sodium niobate
NaOH	Sodium hydroxide
NaOH	Sodium hydroxide
Nb ₂ O ₅	Niobium oxide
NH ₃ -N	Ammoniacal nitrogen
NHE	Normal hydrogen electrode
Ni	Nickel
O&G	Oil and grease
O ₂	Oxygen

$O_2^{\cdot-}$	Superoxide anion
O_3	Ozone
OH^-	Hydroxide ions
PEG	Polyethylene Glycol
PL	Photoluminescence spectroscopy
POME	Palm oil mill effluent
Pt	Platinum
Pzc	Point of zero charge
R_C	Radicle length of control
RhB	Rhodamine B
ROS	Reactive oxygen species
<i>S. aureus</i>	<i>Staphylococcus aureus</i>
SiO_2	Silicon dioxide
Sn_3O_4	Tin oxide
SOP	Standard operating procedure
$SrTiO_3$	Strontium titanate
SS	Suspended solid
TEM	Transmission electron microscopy
TiO_2	Titanium dioxide
TPR	Transient photocurrent response
TS	Total suspended solid
UV	Ultraviolet
UV-vis DRS	Ultraviolet-Visible Diffuse Reflectance Spectroscopy
VB	Valence band

VS	Volatile solids
VSM	Vibrating sample magnetometer
WO ₃	Tungsten oxide
WO ₃	Tungsten oxide
XPS	X-ray photoelectron spectroscopy
XRD	X-ray diffraction
ZnFe ₂ O ₄	Zinc spinel ferrite
ZnO	Zinc oxide
ZnS	Zinc sulfide
ZnWO ₄	Wolframite-tungsten
ZOI	Zone of inhibition
zpc	Zero-point charge

CHAPTER 1

INTRODUCTION

1.1 Background of Study

Malaysia's oil palm industry has a long history, dating back to the early 20th century when the first oil palm trees were introduced to the country (Mutsaers, 2019). Since then, it has grown to become one of the largest producers and exporters of palm oil in the world. According to the Malaysian Palm Oil Board (MPOB), the country produced 19.15 million tons of palm oil in 2020, accounting for nearly 30% of the world's palm oil production.

However, the rapid expansion of the palm oil industry has also led to environmental and social issues. Generation of massive quantity of crude palm oil consumed a lot of water and thus resulted to large quantity of thick brownish palm oil mill effluent (POME). Additionally, each tonne of palm oil has been estimated to produce 2.5-3.75 tonne of POME. This thick brownish effluent is greatly contaminating wastewater which can cause serious water pollution. Several species of pathogens can be harmful to humans and can be associated with the oil palm industry in Malaysia (Murphy et al., 2021). Some of these include bacteria such as *B. cereus* and *E. coli*. These pathogens can cause a range of health issues, including food poisoning, respiratory infections, and skin

infections (Ehling-Schulz et al., 2019; Colaco et al., 2021; Cormontagne et al., 2021; Alharbi et al., 2019). The oil palm industry in Malaysia needs to have proper measures in place to minimize the risk of pathogen contamination and ensure the safety of their workers and consumers.

Despite the challenges, there have been efforts to address these issues and promote sustainability in the industry. In recent years, the Malaysian government has introduced sustainability regulations and certification programs such as the Malaysian Sustainable Palm Oil (MSPO) standard. The industry has also embraced practices such as conservation agriculture and responsible waste management to reduce its impact on the environment. The conventional methods for treating Palm Oil Mill Effluent (POME), such as physical, chemical, and biological treatments, have several disadvantages. One major disadvantage is their high operational cost, which results from the use of expensive chemicals, energy, and maintenance (Mahmod et al., 2023 and Yashni et al., 2020). Another drawback is the limited efficiency of these methods in removing pollutants from the POME. In some cases, these treatments may even generate new pollutants that pose a threat to the environment and human health (Alazaiza et al., 2022). The physical and chemical treatments also tend to generate large amounts of sludge, which requires proper disposal to prevent contamination of soil and water (Nguyen et al., 2022). Additionally, these methods are not always effective in controlling the growth of pathogenic microorganisms, such as bacteria and viruses, which can harm human health (Tirapanampai et al., 2022). Currently, conventional open ponding system was widely used by palm oil industry. While conventional methods have the advantage of being established

and widely used, they have significant drawbacks that need to be addressed. In overall, while the oil palm industry is a significant contributor to Malaysia's economy, it is important to ensure environmental sustainability development to ensure long-term industry health.

1.2 Problem Statement

Palm oil mill effluent (POME) is a major environmental problem caused by the palm oil industry. POME is the wastewater generated from the production of palm oil and it contains a high level of organic pollutants and pathogens, which are harmful to the environment and human health (Rosdi et al., 2022; Imo et al., 2021). The consequences of discharging untreated POME directly into water bodies and the surrounding environment can be severe imposed water pollution leading to the loss of biodiversity and the deterioration of the quality of life for both humans and animals (Ogusina and George, 2020; Jafri et al. 2021; Shakib et al., 2019). The organic components in POME can also contribute to the growth of harmful microorganisms, leading to the proliferation of disease-causing pathogens (Khadaroo et al., 2019).

To address these environmental problems, advanced oxidation processes (AOPs) such as heterogeneous photocatalysis have been proposed as one of the solutions. Photocatalysis is a process in which a semiconductor material, such as titanium dioxide (TiO_2), bismuth vanadium oxide (BiVO_4), tungstate oxide (WO_3) and zinc oxide (ZnO) was used as a catalyst to oxidize and decompose

organic pollutants and pathogens in POME (Ng et al., 2019; Ng K.H., 2021; Saputera et al., 2021; Fernandes et al., 2022). This process is highly efficient, environmentally friendly, and cost-effective, making it a promising alternative to conventional methods. In addition, photocatalysis is a green technology that can be used to reduce the environmental impact of the palm oil industry, to improve the quality of life for the surrounding communities, and to preserve the environment for future generations.

BiOCl has attracted significant interest due to its unique layered structure, excellent chemical stability, and high photoactivity (Yang et al., 2021; Ma et al., 2022; Shi et al., 2021). However, the application of pure BiOCl as a photocatalyst is limited by factors such as fast charge carrier recombination, poor visible light harvesting ability, and difficulty in catalyst recovery (Sharma et al., 2022; Zhang et al., 2021). As a result, the development of an active BiOCl photocatalyst is an important research direction for current researchers.

Combining BiOCl with other semiconductors to form a heterojunction composite has been found to be an effective method of improving its photocatalytic performance. One such composite is the Z-scheme heterojunction, which effectively separates charge carriers and maintains strong redox ability (Deng et al., 2023; Niu et al., 2020). For example, the Z-scheme Bi₃NbO₇/BiOCl heterojunction photocatalysts demonstrated highly efficient visible light photoactivity for ciprofloxacin degradation and Cr(VI) reduction (Y. Liu et al., 2021). Zhang et al, (2021) developed a Z-scheme BiOI/BiOCl composite through a one-pot solvothermal approach that efficiently degraded

rhodamine B and tetracycline hydrochloride. BaFe_2O_4 , with its strong visible light absorption efficiency and high stability, has been extensively used to produce composite photocatalysts (Kenfoud, Nasrallah, Baaloudj, Belabed, et al., 2022a; Kenfoud, Nasrallah, Baaloudj, Derridj, et al., 2022a; A. Singh & Mishra, 2022a). The superparamagnetic attribute of BaFe_2O_4 resolved the recovery problem of BiOCl in practical applications using an external magnetic field (Mandizadeh et al., 2017a; A. Singh & Mishra, 2022a). Therefore, combining BaFe_2O_4 with BiOCl is of great interest for its practical applicability in the field of photocatalysis. To the best of our knowledge, there is no study on the synthesis of $\text{BaFe}_2\text{O}_4/\text{BiOCl}$ composites as photocatalysts. Besides, there is no photocatalytic test has been conducted for pre-treated POME treatment using $\text{BaFe}_2\text{O}_4/\text{BiOCl}$ composites.

1.3 Objectives

This research aimed to produce BaFe₂O₄/BiOCl composites, which are capable to decompose the pre-treated POME under visible light irradiation (including sunlight). The aims of this study are:

1. To fabricate BiOCl/BaFe₂O₄ composites employing a precipitation-hydrothermal method.
2. To analyze the physical, optical and chemical properties of the newly developed photocatalysts using various characterization methods.
3. To optimize the photocatalytic performance of developed photocatalysts on the decomposition of pre-treated POME.
4. To study the kinetics, electrical energy efficiencies as well as mechanism involved in photodecomposition of pre-treated POME.
5. To examine the antibacterial activities of developed photocatalysts against *E. coli* and *B. cereus*.

1.4 Scope of Study

In the current study, BiOCl semiconductors with different BaFe₂O₄ loadings are synthesized using a precipitation-hydrothermal method. The optical and physicochemical properties of the as-synthesized photocatalysts are then studied using X-ray diffraction (XRD), Fourier transform infrared (FTIR), energy-dispersive X-ray spectroscopy (EDX), field emission scanning electron microscopy (FESEM), Transmission electron microscope (TEM), X-ray photoelectron spectroscopy (XPS), zeta potential measurement, vibrating sample magnetometer (VSM), specific surface analysis (SSA), ultraviolet-visible diffuse reflectance spectroscopy (UV-vis DRS), Mott-Schottky (M-S), transient photocurrent response (TPR) and electrochemical impedance spectra (EIS). The photocatalytic performances of as-synthesized BaFe₂O₄/BiOCl composites are analysed via decomposition of pre-treated POME and inactivation of pathogen bacteria such as *E. coli* as well as *B. cereus*.

Process parameters such as catalyst loading (0.25g/L, 0.50g/L, 0.75 g/L and 1.00g/L), solution pH (2.0, 4.0, 7.0 and 9.0), and initial POME concentration (50ppm, 75ppm, 100ppm, and 150ppm) are analyzed in this study. The investigated range in the process parameters is elected according to previous reports and through trial-and-error techniques. Active species trapping tests are performed to justify the role and importance of reactive oxygen species (ROS) that participated in photocatalytic reactions. To measure the stability of developed photocatalysts, the recycling experiment is conducted on visible light decomposition of pre-treated POME. Then, the kinetic study is evaluated using

a Langmuir-Hinshelwood (L-H) first-order kinetic model to investigate the photocatalytic reaction of developed photocatalysts. In addition, the electrical energy consumption per order of 5wt%BaFe₂O₄/BiOCl is determined. The phytotoxicity experiment of the 5wt%BaFe₂O₄/BiOCl is analyzed using *vigna radiata* on pre-treated POME before and after the photocatalytic performance. Antibacterial studies such as the zone of inhibition (ZOI) towards developed BaFe₂O₄/BiOCl against gram-positive *B. cereus* and gram-negative *E. coli* are investigated.

1.5 Organization of Thesis

They are mainly five chapters in total in this research thesis.

Chapter 1 presents the comprehensive framework and organization of the research, covering the topics of POME pollution, the limitations of conventional wastewater treatment methods, and the introduction of heterogeneous photocatalysis. The problem statement highlights the severe impact of POME on the environment and the limitations of individual photocatalysts. The objectives of the research are clearly defined, and the scope of the study and the structure of the thesis are outlined and summarized. The study also highlights the various strategies implemented through modification to overcome the challenges faced in the photocatalytic treatment of POME.

Chapter 2 comprises a comprehensive review of the relevant literature about this research. It presents an overview of the formation and characteristics of palm oil mill effluent (POME), conventional remediation techniques, and the background and fundamentals of heterogeneous photocatalysis. Additionally, the chapter provides an in-depth examination of the mechanism of metal oxides coupling with BiOCl, as well as a presentation of case studies related to the aforementioned bismuth composites. The chapter concludes with a discussion of the impact of operational parameters on photocatalytic performance.

Chapter 3 outlines the synthesis pathways of the BaFe₂O₄/BiOCl composites and the characterization of the resulting products, focusing on their physical, chemical, and optical properties. Additionally, this chapter provides a comprehensive overview of the experimental setup and conditions used for the degradation of POME, as well as the analytical procedures employed.

Chapter 4 presents a comprehensive analysis of the research findings and outcomes, offering reasonable explanations for the results obtained. This chapter includes a thorough analysis of the characterization results, including X-ray diffraction (XRD), Fourier transform infrared (FTIR), energy-dispersive X-ray spectroscopy (EDX), field emission scanning electron microscopy (FESEM), Transmission electron microscope (TEM), X-ray photoelectron spectroscopy (XPS), vibrating sample magnetometer (VSM), zeta potential measurement, specific surface analysis (SSA), ultraviolet-visible diffuse reflectance spectroscopy (UV-vis DRS), Mott-Schottky (M-S), transient photocurrent response (TPR) and electrochemical impedance spectra (EIS)

studies of the as-synthesized catalyst. Further, the photocatalytic activity of the catalyst on the decomposition of palm oil mill effluent (POME) is discussed concerning various operating parameters. The results of decomposition tests, scavenger tests, cyclic experiments, phytotoxicity tests as well as *B. cereus* and *E. coli* clearance experiments are also evaluated. This chapter also accompanied with a kinetic analysis and electrical energy consumption (EEC) of the photocatalytic process.

Chapter 5 presents the conclusions of the study, including a summary of the research findings and their implications, as well as recommendations for future work in the area. The chapter also offers suggestions for improving the methodology and application of the results, highlighting the key contributions of the study and its significance to the field.

CHAPTER 2

LITERATURE REVIEW

2.1 Palm Oil Mill Effluent (POME)

POME is a type of wastewater generated from the palm oil production process. It is comprised of a mixture of organic matter, water, and various chemicals used in the production process. The study of POME is critical due to its potential to cause significant environmental pollution, as well as its negative impact on human health and ecosystems (Hayawin et al., 2022). The high levels of organic matter, nutrients, and other pollutants in POME can lead to the eutrophication of water bodies, reducing the oxygen levels and leading to the death of aquatic life (Ding et al., 2020). Additionally, the discard of untreated POME can also result in the release of greenhouse gases and contributed to climate change (Suksaroj et al., 2020) It is therefore essential to understand the properties and behaviours of POME to develop effective treatment methods to mitigate its environmental impacts.

2.1.1 Origin of POME

The production of palm oil mill effluent (POME) is a result of the extraction process of crude palm oil from oil palm fruit. During the production of crude palm oil, large amounts of water and organic matters are generated as by-products (Awual, 2019). These organic matters, mixed with water, is referred to as POME. The characteristics of POME are highly dependent on the type of palm oil extraction process used, but in general, it is characterized as a dark brown coloured effluent with a strong odour (Lau et al., 2021; Zahra et al., 2020). POME is a complex mixture of organic compounds, including fatty acids, proteins, and carbohydrates, along with suspended solids and inorganic ions (Ahmad & Ghufuran, 2022; Rachmadona et al., 2021). It is a highly polluting material that is toxic to aquatic life and can cause severe environmental degradation if not treated properly (Wahyono et al., 2020).

2.1.2 Characteristics of POME

Each tonne of POME produces 28m³ of methane gas (CH₄). Inadequate control and release of CH₄ can attribute to global warming as it is the second most anthropogenic greenhouse gas within the atmosphere, below than CO₂ (Tan et al., 2021). Raw POME from mill appears to be viscous heavily coloured colloidal solution at temperature as low as 353 K up to 373 K. The darkish brown colour of POME solution is caused by humic acid and fulvic acid-like

components, including tannin and lignin (Lee et al., 2019; Syahin et al., 2020). It has an unpleasant and undesirable odour. POME comprises ~96% of water, ~4% of total solids (included ~2% of suspended solids) and ~0.7% of oils (Ahmad et al., 2022; Dashti et al., 2020). The chemical oxygen demand (COD) and biochemical oxygen demand (BOD) are 51,000ppm and 25,000ppm, respectively. It is acidic with pH of approximately 4.5 due to the content of organic acids in complex form. **Table 2.1** shows the characteristics of POME produced from each palm oil extraction stages. Regards it's non-toxic in nature is because of non-chemical extraction process, the organic content is considering high for POME to be discharged into water region thus POME treatment is needed (Lokman et al., 2021).

Table 2.1: General properties of untreated POME in palm oil mills (Lee et al., 2021; Naidua et al., 2021; Nasrullah et al., 2020)

Parameter	Mean	Range
Temperature	-	80 – 90
pH	4.2	3.4 – 5.2
BOD	25,000	10,250 – 43,750
COD	51,000	15,000 – 100,000
TS	40,000	11,500 – 79,000
SS	18,000	5,000 – 54,000
Volatile Solids (VS)	34,000	9,000 – 72,000
Oil and Grease (O&G)	6,000	130 – 18,000
Ammoniacal Nitrogen (NH ₃ -N)	35	4 – 80
Total Nitrogen	750	180 – 1,400

*All parameters are expressed in mg/L, except temperature (°C) and pH.

Typically, the quality and quantity of POME can be altered by batches from day to days and different processing factories, relying on the oil palm cropping seasonal and operation of palm oil mill for example shut down of palm oil mill, quality control, operation of individual mills and occasional public holiday (Mahmod et al., 2022).

High organic components of POME can cause tremendous jeopardy to the ecosystem. The disposal of POME into nearby water bodies could pollute and worsen the water quality available for consumption (Tan & Lim, 2019). The brownish POME also prevented sunlight from penetration and declined the photosynthesis activity in receiving water (Owodunni & Ismail, 2021). In addition, POME may release possibly hazardous components including ammonia and halogen that can bring negative impacts on aquatic living system (Ghosh et al., 2021; Vítězová et al., 2020). POME also consisting of variant of bacteria such as *Staphylococcus aureus* (*S. aureus*), *Bacillus spp.*, and *Escherichia coli* (*E. coli*) could also impose severe damage to environment (Karim et al., 2019; Shahid-ul-Islam et al., 2019; Wong et al., 2019a). Thus, it is significant to treat the POME via an appropriate treatment to minimize its impact to the environment.

2.1.3 Conventional Treatment of POME

With the fast development of industry sector and uplifted public concern of environmental protection, the industry is obliged both aesthetically and

publicly to treat its effluent before committing discharging it to the environment. Thus, the Department of Environment (DoE), Malaysia has established standards for POME disposal into water bodies through Environmental Quality (Prescribed Premises) (Crude Palm Oil) Regulations, 1977 under the act of Environmental Quality Act (EQA) 1974. Day after all palm oil mills is compulsory to treat their effluent before discharging it into the environment. Then, the discharge limit of BOD value has been amended from 100 mg/L to 20 mg/L for palm oil mills in several critical region in Sabah and Sarawak due to the continuous high rising of the pollutants (Tan et al., 2019) Apart from the BOD reading, COD is another indicator for oxygen content analysis. The COD of the released wastewater needs to be maintained beneath 50 mg/L following to Malaysia Sewage and Industrial Effluent Discharge Standard to avoid pollution and protect the environment (Kuok et al., 2022). **Table 2.2** demonstrated the regulatory discharge limit of POME in Malaysia.

Table 2.2: Regulatory discharge limit for POME in Malaysia (Kuok et al., 2022; Tan et al., 2019)

Parameters	Regulatory Discharge Standards
pH	5.0 – 9.0
BOD	100 (20 in Sabah and Sarawak)
COD	50
TS	1,500
SS	400
O&G	50
NH ₃ -N	150
Total Nitrogen	200

*All parameters are expressed in mg/L, except pH.

Conventional treatment methods for POME are widely applied to reduce its environmental impact. The most used methods are physical, chemical, and biological treatments, such as sedimentation, flocculation, and aerobic/anaerobic digestion (Aravind Kumar et al., 2022; Cheng et al., 2021; Soo et al., 2022). Sedimentation is a widely used conventional treatment method for the treatment of POME. It involves the settling of suspended solids in wastewater, which leads to the separation of solid and liquid phases. This method is commonly used in the preliminary treatment of POME before it is subjected to further treatment processes. During sedimentation, the POME is allowed to settle in a large tank, and the solids that settle at the bottom are then removed (Mohamad et al., 2021).

Flocculation is another conventional treatment process used for the treatment of POME. It is a process that enhances the settling of suspended solids in wastewater. In this process, flocculants, such as alum or polyelectrolytes, are added to the POME to promote the formation of larger and denser particles. The resulting flocs are then separated from the liquid phase through sedimentation. This method is commonly used in combination with sedimentation to achieve more efficient solids separation (Huzir et al., 2019).

Aerobic and anaerobic digestion are both biological treatment methods for POME. Aerobic digestion, which occurs in the presence of oxygen, is employed to degrade the organic constituents in POME through the action of microorganisms. In this process, the microorganisms use the organic matters in the POME as a source of energy and converted them into carbon dioxide and water. Anaerobic digestion, on the other hand, takes place in the absence of

oxygen and is used to break down the organic matter in POME through the action of anaerobic microorganisms. This process is typically used in large-scale wastewater treatment plants and resulted in the production of biogas, which can be used as a source of energy (Chan et al., 2023).

However, these conventional methods have limitations in terms of effectiveness, cost, and energy consumption. For example, sedimentation and flocculation are limited in their ability to remove high molecular weight organic compounds and suspended solids, while aerobic/anaerobic digestion required significant energy inputs and produced large amounts of sludge. Moreover, these conventional methods do not completely eliminate pollutants, as they typically only reduce their concentration rather than completely removing them.

Therefore, there is a need to explore alternative methods for treating POME that are more efficient, cost-effective, and environmentally friendly. Photocatalysis, a type of advanced oxidation process (AOP), has emerged as a promising alternative for treating POME, offering the potential for the complete removal of organic compounds without producing hazardous by-products.

2.1.4 Polishing Processes of Treated POME

There are several polishing methods that are commonly used to treat POME in order to reduce its harmful impact on the environment. Some of the most used polishing methods include membrane filtration, adsorption, reverse

osmosis, constructed wetland and Advanced oxidation processes (AOPs) are commonly used polishing methods for the treatment of using industrial effluents (Kamali et al., 2019; Rahman et al., 2020; Teow et al., 2021). Membrane filtration is a physical separation process that removed suspended solids, colloids, and dissolved substances from the wastewater using membranes. This method is effective in removing contaminants, but it is expensive and required frequent maintenance. Moreover, adsorption and reverse osmosis are another physical treatment processes. However, they also suffered from limitations by the availability of the adsorbent materials as well as the need of high temperature and pressure (Ho et al., 2021).

The AOPs, on the other hand, are chemical processes that used strong oxidants to break down contaminants in the wastewater. AOPs have several advantages over the other polishing methods, including high degradation efficiency, low production of toxic by-products, and low energy consumption. Moreover, AOPs are flexible and can be applicable in treating wide range of environmental pollutants, making it an attractive option for POME treatment (Aris et al., 2019). In conclusion, AOP stands out as one of the most effective and efficient option for the treatment of industrial effluents, with its combination of high degradation efficiency, low production of toxic by-products, and low energy consumption.

2.2 ADVANCED OXIDATION PROCESSES (AOPs)

AOPs are water treatment processes that used the oxidation power of highly reactive species to remove pollutants from contaminated water. The technology has evolved over time, with several milestones achieved along the way.

In the early 1990s, the first AOP was developed using light radiation and hydrogen peroxide (H_2O_2) as the oxidant. The light/ H_2O_2 process was simple, efficient, and produced environmentally friendly by-products. It was seen as an improvement over traditional oxidation processes, which often generated toxic by-products (Garrido-Cardenas et al., 2019). In the late 1990s and early 2000s, researchers began exploring other oxidants, such as ozone (O_3) and hydrogen peroxide/ozone ($\text{H}_2\text{O}_2/\text{O}_3$). These processes showed promise but were limited by the need for high energy inputs and the difficulty of controlling ozone generation (Fan et al., 2020; Xiao et al., 2020). Thus, the researchers turned their attention back to the light/ H_2O_2 process, refining the technology and making it more efficient. They improved the process by optimizing the conditions for generating hydroxyl radicals, the main oxidizing species in the process. Today, the light/ H_2O_2 process is considered one of the best options in AOPs due to its simplicity, efficiency, and low environmental impact. The process is now widely used in industrial and municipal wastewater treatment, with millions of cubic meters of contaminated water being treated every day (Nemiwal et al., 2021; Y.

Wang et al., 2020). Furthermore, the mechanism of AOP typically involves four steps:

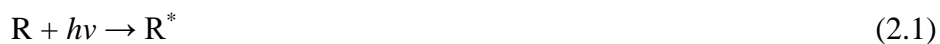
1. Generation of active radicals: In this step, the reactive radicals such as hydroxyl radical and superoxide anion radicals are generated through various methods such as UV light, heat, and electrical discharge.
2. Transfer of reactive radicals to the pollutant: In this step, the reactive radicals are transported to the pollutant molecule, where they react with it, oxidizing and breaking it down.
3. Formation of Intermediate Products: During the oxidation process, intermediate products are formed. These intermediate products included organic acids, aldehydes, and alcohols.
4. Mineralization of Intermediate Products: In this step, the intermediate products are further degraded and mineralized into simpler, less harmful compounds such as carbon dioxide (CO₂), water (H₂O), and other inorganic compounds.

The overall mechanism of AOP is based on the powerful oxidation ability of reactive radicals, which allows for the degradation of a wide range of pollutants including organic compounds, bacteria, viruses, and pathogens. This makes AOPs as effective and efficient polishing method for POME and other types of wastewater.

2.3 PHOTOCATALYSIS

Photocatalysis is a phenomenon that has gained significant attentions in the scientific community. Theoretical advancements in the field of photocatalysis continued throughout the with the development of the theories of band structures, carrier dynamics, and the interaction between light and matter (Efros & Brus, 2021; Lu et al., 2019).The widespread use of titanium dioxide as photocatalyst in applications such as air purification, self-cleaning surfaces, and water treatment has since demonstrated the potential of photocatalysis as a means of environmental remediation.

In the following decades, the advancement of photocatalysis has been driven by the discovery and development of new materials and mechanisms (Li et al., 2020). The application of photocatalysis to environmental remediation has also grown, with increasing attention being paid to the development of advanced oxidation processes (AOPs) that incorporate photocatalytic reactions (Liu et al., 2020). The ongoing evolution of photocatalysis has resulted in a range of highly efficient materials and techniques that have the potential to solve a range of environmental challenges, from water purification to air remediation. The field of photocatalysis is poised for continued growth and expansion in the coming years, as new materials, mechanisms, and applications continue to emerge. The general chemical equation for photocatalysis can be represented as follows: (Zhang, et al., 2020).



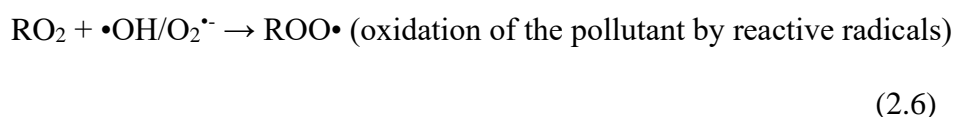
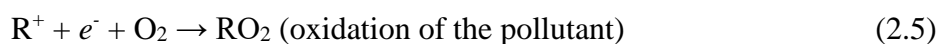
Where "R" is the pollutant species, " $h\nu$ " represents the photon energy of light, and "R*" represents the excited state of the pollutant.

In the presence of a photocatalyst, the excited state "R*" of the pollutant can participate in the oxidation-reduction reactions, resulting in the degradation of the pollutant. The electron transfer from the activated form of the pollutant to the photocatalyst's conduction band results in the formation of reactive oxygen species, such as $\bullet OH$, $\bullet O_2^-$, and hydrogen peroxide (H_2O_2). These reactive oxygen species are highly oxidative and can break down pollutants into simple and non-toxic compounds (Shi & Lang, 2020).

Table 2.3: Redox potential for selected generic oxidants used in AOPs. (Sun et al., 2019)

Species	Chemical Structure	Redox Potential (V vs NHE)
Superoxide radical	$\bullet O_2^-$	-0.33
Hydroperoxyl radical	$HOO\bullet$	-0.05
Hydrogen peroxide	H_2O_2	0.682
Hydroxyl radical	$\bullet OH$	2.72

In summary, photocatalysis involves the utilization of light energy and a photocatalyst to generate reactive oxygen species, which can then oxidize and degrade organic pollutants. The chemical formula for the photocatalytic oxidation of pollutants using photocatalyst and light can be represented as:



Photocatalysis is started with the absorption of light by the photocatalyst, leading to the generation of electron-hole pairs. The photogenerated electrons occupied the conduction band, creating a surplus of holes in the valence band. Subsequently, these holes acted as oxidizing agents, facilitating the direct oxidation of organic pollutants present in the wastewater or indirectly oxidize the hydroxyl radical into $\bullet\text{OH}$. On the other hand, the electrons in the conduction band participated in the reduction of oxidizing species like oxygen resulting in the formation of $\bullet\text{O}_2^-$. These reactive radicals then attacked the pollutants, causing them to break down into smaller and less harmful compounds. The list of contaminants that can be degraded by heterogeneous photocatalysis shown in Table 2.4.

Table 2.4: List of pollutants decomposed during photocatalysis. (Continue)

Class of organics	Pollutant	Photocatalyst	Reference
Dyes	Rhodamine B	TiO ₂	(Xu & Ma, 2021)
	Methylene Blue	ZnO	(Smazna et al., 2019)
	Acid red 88	ZnFe ₂ O ₄	(Surendra et al., 2020)
	Congo Red	CdS/BiOBr	(Hu et al., 2022)
Phenols	<i>p</i>-cresol	AgO/FSZr	(Aziz et al., 2021)
	Phenol	FeTiO ₃ /GO	(Moradi et al., 2021)
	Bisphenol A	CeO ₂ /g-C ₃ N ₄	(Zhao et al., 2021)
Aromatic compounds	Benzene	ZnWO ₄	(Ma et al., 2021)
	Toluene	CeO ₂	(Wei et al., 2022)
	Naphthalene	CeVO ₄	(Lu et al., 2020)
Pesticide	Carbofuran	NaNbO ₃ -Au-Sn ₃ O ₄	(Li et al., 2020)
	Chlorpyrifos	CuO/TiO ₂ /PANI	(Nekooie et al., 2021)

Table 2.4: List of pollutants decomposed during photocatalysis.

Class of organics	Pollutant	Photocatalyst	Reference
Pharmaceuticals	Ibuprofen	CdS/Fe ₃ O ₄ /TiO ₂	(Zhou et al., 2020)
	Carbamazepine	Fe ₃ O ₄ /BiOBr/CQDs	(Xie et al., 2021)
	Diclofenac	ZnO-WO ₃	(Mugunthan et al., 2019)
Industrial wastewater	POME	TiO ₂	(Ng, 2021)
	Textile wastewater	Ag-ZnO	(Oda et al., 2019)
	Pulp and paper wastewater	Fe-TiO ₂	(Puri & Verma, 2022)

2.3.1 BiOCl As A Photocatalyst

The utilization of photocatalysis has proven to offer numerous benefits to human society, including alternative energy sources and environmental remediation. Semiconductors are considered as the most promising materials for these applications, owing to their ability to facilitate interactions between light and molecules, as well as their favorable band gap energies and well-defined electronic configurations. Some notable examples of semiconductors utilized in photocatalysis included ZnO, WO₃, CdS, SrTiO₃, ZnS, CdTe, and AgNbO₃, as

highlighted in various studies (Duong et al., 2019; Li et al., 2022; Liao et al., 2021; Sansenya et al., 2022; Sharma et al., 2021; Yin et al., 2019). Out of these, bismuth oxychloride (BiOCl) stood out as a new emerging compelling option, BiOCl possessed a large band gap energy (3.2 ~3.6 eV) and a high electron mobility, which allows it to efficiently harness light energy and to carry out photodecomposition of organic pollutants (Chao et al., 2019; Yang et al., 2023; Zhang et al., 2021). Additionally, BiOCl is highly versatile and can be easily modified to enhance its photocatalytic activity. Moreover, it is inexpensive, environmentally friendly, high physiochemical stability and non-toxic, making it an attractive option for a wide range of environmental applications (Hou et al., 2021). However, it also has some limitations that hinder its widespread application. One of the major disadvantages of BiOCl is the difficulty in catalyst separation (Su et al., 2022). In fact, BiOCl is small in size and complicated to completely segregate them after the photocatalytic process. This will lead to loss of catalytic powder during the recovering process. Another disadvantage is the large band gap of BiOCl, which limits its light absorption in the visible light region, thus reducing its photocatalytic activity. Additionally, the fast recombination of electron-hole pairs in BiOCl also resulted in low quantum efficiency, limiting the overall efficiency of the photocatalytic process (Qi et al., 2021). Thus, attempts have been made to synthesize magnetic separable BiOCl photocatalytic with enhanced interfacial charge transfer and visible light absorption.

2.3.2 Z-scheme Heterojunction Photocatalyst

The Z-scheme heterojunction photocatalyst refers to a type of photocatalyst system that consists of two or more different semiconductor materials that are integrated together. This structure creates a sequential electron transfer pathway, known as the Z-scheme, between the two different materials. The Z-scheme heterojunction photocatalyst is designed to overcome the limitations of traditional single-component photocatalysts by improving the separation of photogenerated electrons and holes, reducing the recombination of these charges, and enhancing the overall photocatalytic performance (Cao et al., 2021; Fan et al., 2021a; Zhang et al., 2021). The unique architecture of the Z-scheme heterojunction photocatalyst allows for the combination of two different semiconductors with complementary properties, such as band gap energy, charge mobility, and electron affinity (Yang et al., 2022). This results in improved light utilization, increased electron-hole separation, and reduced recombination of charges, which leads to an overall improvement in photocatalytic efficiency (Fan et al., 2021b; Xu et al., 2022). The improved performance and versatility of Z-scheme heterojunction photocatalysts have made them a promising technology for a wide range of applications in the future (Kumar, Sharma, et al., 2021).

Jiang et al. (2019) investigated the use of CQD-SnNb₂O₆/BiOCl Z-scheme catalyst in treating the benzocaine over 90 mins, whereby 100% of benzocaine decomposition was achieved under 250W Xe light irradiation. Besides, the optimum catalyst loading and pH of benzocaine decomposition were found to be 0.5 g/L and a neutral pH, respectively. However, the

recyclability test of CQD-SnNb₂O₆/BiOCl over benzocaine decomposition revealed that a small degree of decline after 4th cycle.

Zhang et al. (2020) examined the utilize of Ag/BiOCl/AgIO₃ catalyst in treating the RhB over 120 mins, whereby 93% of RhB degradation was achieved under simulated sunlight irradiation. Also, the catalyst loading in RhB decomposition was found to be 1.0 g/L. Nevertheless, the recyclability test of Ag/BiOCl/AgIO₃ over RhB revealed that the degradability of Ag/BiOCl/AgIO₃ reduced from 93% to 39% after 6th cycle. They claimed that there is chemical bond between AgI and BiOCl, which hinders the further deterioration of AgI/BiOCl. That is, the Ag/BiOCl/AgI heterojunction is formed between AgI and BiOCl.

Tang et al., (2020) reported the application of Z-scheme CdS/BiOCl catalyst in handling the RhB over 100 mins, whereby 90% of RhB decomposition was achieved under simulated sunlight irradiation. Likewise, the catalyst loading of RhB degradation were found to be 1.0 g/L. Nonetheless, the recyclability test of Z-scheme CdS/BiOCl over RhB decomposition reported that the degradability of Z-scheme CdS/BiOCl slightly reduced after 5th cycle.

Dang et al. (2022) introduced the application of Z-scheme Fe₃O₄/BiOCl/BiOI in treating the pre-treated tetracycline over 80 mins, whereby 89% of tetracycline degradation was achieved under sunlight irradiation. Besides, the catalyst loading and concentration of tetracycline solution were found to be 0.4 g/L and 40 ppm, respectively. However, the

recyclability test of Z-scheme $\text{Fe}_3\text{O}_4/\text{BiOCl}/\text{BiOI}$ over tetracycline decomposition revealed that the degradability of Z-scheme $\text{Fe}_3\text{O}_4/\text{BiOCl}/\text{BiOI}$ reduced from 89% to 80% after 5th cycle. Carbon deposited on the catalyst was found to be the reason that led to decrease in catalyst reactivity. They claimed that the magnetic properties of the Z-scheme $\text{Fe}_3\text{O}_4/\text{BiOCl}/\text{BiOI}$ aided in the recovery of catalyst that prevent losses.

Chachvalvutikul & Kaowphong (2020) evaluated direct Z-scheme $\text{FeVO}_4/\text{BiOCl}$ catalyst in treating the Cr(VI) over 360 mins, whereby 97% of Cr(VI) degradation was achieved under visible light irradiation. Likewise, the optimum catalyst loading and pH of Cr(VI) degradation were found to be 0.5 g/L and at a pH 3 solution, respectively. Nevertheless, the recyclability test of Z-scheme $\text{FeVO}_4/\text{BiOCl}$ over Cr(VI) degradation revealed that the degradability of Z-scheme $\text{FeVO}_4/\text{BiOCl}$ slightly reduced from 97.8% to 94.8% after 3rd cycle.

Zhang et al. (2022) revealed rGO-modified $\text{BiOCl}/\text{Co-doped SrFe}_{12}\text{O}_{19}$ catalyst in treating the RhB over 80 mins, whereby 94% of RhB degradation was achieved under simulated sunlight irradiation. Besides, the optimum catalyst loading and concentration of RhB degradation were found to be 1.0 g/L and 10 ppm, respectively. However, the recyclability test of rGO-modified $\text{BiOCl}/\text{Co-doped SrFe}_{12}\text{O}_{19}$ over RhB degradation revealed that the degradability of RhB reduced from 85% to 70% after 4th cycle.

Liu et al. (2022) investigated the use of $\text{CoFe}_2\text{O}_4/\text{BiOCl}$ in treating the NOR and Cr(VI) over 120 mins, whereby 75.5% and 78% degradation were achieved under visible light irradiation. Furthermore, the optimum catalyst loading and pH of solution for Cr(VI) degradation were found to be 1.0 g/L and at a pH of 2, respectively. However, the recyclability test of $\text{CoFe}_2\text{O}_4/\text{BiOCl}$ over RhB degradation revealed that the degradability of $\text{CoFe}_2\text{O}_4/\text{BiOCl}$ reduced from 65% to 55% after 3rd cycle.

Dong et al. (2020) reported the application of $\text{H-TiO}_2/\text{BiOCl}$ heterojunction in treating the tetracycline hydrochloride and MO over 120 mins, whereby 82% of tetracycline hydrochloride degradation was achieved under 250W visible light irradiation. In addition, the catalyst loading and concentration of tetracycline degradation were found to be 1.0 g/L and 10 ppm, respectively. However, the recyclability test of $\text{H-TiO}_2/\text{BiOCl}$ over tetracycline hydrochloride degradation revealed that the degradability of $\text{H-TiO}_2/\text{BiOCl}$ had no significant changes after 5th cycle.

2.3.3 Barium Spinel Ferrite, BaFe_2O_4

Spinel ferrite, scientifically is a material class of inorganic compounds represented by the chemical formula of MFe_2O_4 , where M represents one or more divalent metal cations such as Magnesium (Mg), Manganese (Mn), Nickel (Ni), Barium (Ba) or Zinc (Zn). These materials are characterized by a crystal structure that consists of a regular arrangement of oxygen and metal atoms, forming a three-dimensional network of tetrahedrons. The crystal structure and

the presence of iron(III) ions in a high oxidation state result in magnetic and electrical properties that make spinel ferrites suitable for various applications, such as in magnetic storage devices and electromagnetic shielding (Narang & Pubby, 2021). Additionally, recent studies have revealed their potential as photocatalysts due to their ability to absorb light and facilitate the transfer of electrons and holes, leading to the degradation of organic pollutants (Ismael & Wark, 2022).

Barium Ferrite, scientifically known as BaFe_2O_4 , is a type of iron oxide that belongs to the class of magnetic materials known as spinel ferrites. It is an inorganic compound composed of barium, iron, and oxygen, where barium ions are surrounded by an octahedral arrangement of oxygen ions and iron ions occupy both tetrahedral and octahedral sites within the lattice structure (Abdalazeez et al., 2022). BaFe_2O_4 has a crystal structure with a cubic close-packed arrangement and is recognized as one of the most common ferrite magnetic materials with a high magnetic permeability and high magnetic storage capacity (Nikolic, 2020). Additionally, BaFe_2O_4 has been shown to possess catalytic properties and has been explored as a potential photocatalyst in environmental remediation applications, demonstrating the versatility and potential of this material (Kenfoud et al., 2022a).

Singh and Mishra (2022) studied the use of $\text{BaFe}_2\text{O}_4/\text{rGO}$ heterojunction in treating the chlorhexidine digluconate via visible light and UV light over 40 mins, whereby the decomposition of chlorhexidine digluconate

was achieved 93%. Moreover, the optimum pH value of the solution was found to be alkaline condition.

Kenfoud et al. (2022a) investigated the use of BaFe₂O₄/ZnO heterojunction in treating the RhB over 180 mins, whereby 93% of RhB degradation was achieved under visible light irradiation. In addition, the catalyst loading and concentration of RhB were found to be 1.0 g/L and 15 ppm, respectively. Nevertheless, the recyclability test of BaFe₂O₄/ZnO over RhB degradation revealed that the degradability of BaFe₂O₄/ZnO had no significant changes after 4th cycle.

Kenfoud et al. (2022b) studied the use of BaFe₂O₄/SnO₂ in handling the Cr(VI) over 120 mins, whereby 75.5% degradation was achieved under visible light irradiation. Besides, the optimum pH of solution for Cr(VI) and initial pollutants concentration degradation were found to be at a pH of 3 and 30 ppm, respectively. However, the recyclability test of BaFe₂O₄/SnO₂ over Cr(VI) degradation revealed that the degradability of BaFe₂O₄/SnO₂ reduced from 100% to 92% after 5th cycle. They claimed that BaFe₂O₄/SnO₂ was effective after multiple cycles, and it can be easily recovered from the photocatalytic system due to its paramagnetic property.

Keerthana et al. (2022) studied the 2% La-BaFe₂O₄ in treating the MB over 120 mins, whereby 80% and 85% degradation were achieved under UV light and visible light irradiation respectively. However, the recyclability test of 2% La-BaFe₂O₄ over MB degradation revealed that the degradability of 2% La-

BaFe₂O₄ remained at 85% (80%) after 3rd cycle under visible light (UV light). They went further to explain the constant efficiency retained by the 2% La-BaFe₂O₄ sample indicated its stable structure.

By combining BaFe₂O₄ and BiOCl in a direct Z-scheme, it is possible to eliminate these drawbacks. The magnetic properties of BaFe₂O₄ can help in promoting the separation of the photocatalytic species, while the large band gap of BiOCl can improve the photocatalytic performance. This direct Z-scheme can result in enhanced photocatalytic activity and improved separation efficiency, making it a promising approach for environmental treatment and alternative energy applications. Based on our knowledge, BaFe₂O₄/BiOCl composite was not reported by any other researcher.

2.4 Photocatalytic Pre-Treated POME Treatment

Photocatalytic processes had been reported as a good technology for treatment of pre-treated POME. For example, Phang et al. (2021) investigated the use of CuO NPs in treating the POME over 180 mins, whereby 66% degradation was achieved under UV light irradiation. The photocatalytic decomposition was carried under 0.5 g/L of photocatalyst loading. In addition, Razali et al. (2022) investigated the use of WO₃/g-C₃N₄ and WO₃/PANI in treating the POME over 300 mins, whereby 35% and 30% decomposition were achieved under visible light irradiation respectively. Besides, their photocatalyst loading in POME decomposition was found to be 1.0 g/L. Moreover, Shariah

Ghazali et al. (2019) investigated the use of 3-LaCa in treating the POME over 300 mins, whereby 55% of POME degradation was achieved under UV light irradiation. Besides, the catalyst loading was found to be 3.0 g/L. Furthermore, Aqilah Mohd Razali et al. (2023) investigated the use of WO₃/g-C₃N₄/PANI in treating the POME over 120 mins, whereby 55% degradation was achieved under 100 W visible light irradiation. Besides, the pH of solution for POME was found to be at a pH of 9.

2.5 Operating Parameter Studies

The removal efficiency in a photocatalytic reaction can be influenced by various aspects such as temperature, type of light, light intensity, solution pH and initial pollutant concentration. The important process parameters that are analysed in this research inclusive of photocatalyst loading, solution pH and initial pollutant concentration.

2.5.1 Photocatalyst Loading

The efficiency of photocatalytic POME decomposition can be improved by increasing the amount of photocatalyst until an optimum level. This was due to the increase in the photocatalyst loading improved the overall active sites on the surface of photocatalyst (Feilizadeh et al., 2019a) Consequently, the enhanced amount of induced reactive oxygen species (ROS), accelerated the removal of the contaminants. However, when the photocatalyst loading exceeded the optimum amount, the turbidity of the solution increased and led to the cloudiness of the reaction solution. Hence, the effective light penetration became lesser and declined the photocatalytic performance (Arifin et al., 2019). In addition, the overdosed photocatalyst tended to aggregate and reduced the interaction of both radiation and pollutant with the active sites on the surface of photocatalyst (Adeli & Taghipour, 2020; Niu et al., 2020). Table 2.5 displays the impact of photocatalyst loading on the efficiency of photocatalytic decomposition of different organic pollutants.

Table 2.5: Impact of photocatalyst loading on the efficiency of photocatalytic decomposition of organic pollutants.

Pollutant	Photocatalyst	Light source	Photocatalyst loading (mg/L)	Optimum loading (mg/L)	Removal efficiency (%)	References
Methylene blue	BiOCl/MoS ₂	Visible light	1000-10000	4000	96	(Monga & Basu, 2021)
Acid Orange 7	BiOCl-p-Mn ₃ O ₄	Visible light	500-1250	1000	80	(Yosefi & Haghghi, 2019)
Bisphenol A	Co-BiOCl/biochar	Visible light	200-1000	400	93	(Cao et al., 2022)
Tetracycline hydrochloride	BiVO ₄ :Er ³⁺ , Yb ³⁺ /BiOCl	visible light	100-400	200	88.8	(Liu et al., 2022)
Sulfamethoxazole	BiOCl	visible light	250-1500	1500	90	(Petala et al., 2021)

Table 2.5: Photocatalytic decomposition efficiency of various pollutants based on different photocatalyst loadings. (continued)

Pollutant	Photocatalyst	Light source	Photocatalyst loading (mg/L)	Optimum loading (mg/L)	Removal efficiency (%)	References
Valsartan	MoS ₂ /BiOCl	Visible light	50-1000	600	100	(Grilla et al., 2021)
POME	ZnO	UV light	200-1500	1000	100	(Wong et al., 2019b)
POME	TiO ₂	UV light	200-2000	1000	52%	(Ng et al., 2019)
	ZnO	UV light			50%	
POME	WO ₃	UV light	200-3000	500	51%	(Cheng et al., 2017)

Yosefi & Haghghi (2019) displayed that the photocatalytic decomposition efficiency of Acid Orange 7 dye reached up to 80% with the optimum photocatalyst loading of 1.0 g/L under visible light irradiation. Cao et al., (2022) also monitored the effect of photocatalyst varied from 200-1000 mg/L on photocatalytic performance of bisphenol A under visible light irradiation. The 400 mg/L of Co-BiOCl/biochar photocatalyst loading achieved 93% which was the optimum photocatalyst loading in his research. This was attributed due to the aggregation of particles at higher photocatalyst loading, which turned down the photocatalytic decomposition performance. In addition, Grilla et al. (2021) reported that the complete valsartan photodegradation achieved using MoS₂/BiOCl with an optimum photocatalyst loading of 600 mg/L under visible light irradiation. They explained that the appropriate photocatalyst site available contributing the good rate of photodegradation. Monga and Basu (2021) revealed the photocatalytic degradation of methylene blue with BiOCl/MoS₂ under visible light irradiation. They varied the photocatalyst loading ranging from 1000 to 10000 mg/L, in which the optimum photocatalyst loading was found to be 4000 mg/L and achieved the highest 96% photodegradation of methylene blue among the other tested photocatalyst loading. Liu et al. (2022) applied BiVO₄:Er³⁺,Yb³⁺/BiOCl to photocatalytic degrade the tetracycline hydrochloride up to 88.8% with an optimum photocatalyst loading of 200 mg/L under visible light irradiation. This phenomenon was explained that higher or lower dosage of photocatalyst loading triggered a decline in photocatalytic activity that is attributed by the shielding impact as well as agglomeration of photocatalysts and shortage of reaction sites.

On the other hand, Wong et al (2019b) tested the photocatalytic decomposition performance of pre-treated POME under UV light irradiation within the photocatalyst of 200-1500 mg/L. The highest photocatalytic decomposition performance achieved as high as 100% at optimum loading of 1000 mg/L. Cheng et al. (2017) evaluated the effect of WO_3 loading from 200-3000mg/L under halogen light irradiation. The ideal WO_3 loading was 500 mg/L with a 51% degradation efficiency under UV light. The effect of redundant photocatalyst loading of photocatalysts in the pre-treated POME mixture, the mixture tends to less transparent and restrict the light to penetrate. In a nutshell, the photocatalytic decomposition performance is reduced.

2.5.2 Solution pH

The effect of solution pH on the photocatalysis system on decomposition efficiency have been reported extensively. Typically, the influence of solution pH on different kind of contaminants can be adjusted by referring to the photocatalyst's point of zero charge (pzc) to optimize the photocatalytic activity (Bouddouch et al., 2022; Lu et al., 2021). The solution pH can modify the surface charge properties of the photocatalyst and affected the electrostatic interaction within photocatalyst surface and the organic contaminants substrate, which can bring impact to the photocatalytic decomposition performance. Table 2.6 summarizes the photocatalytic decomposition performance of several pollutants at different solution pH values.

Table 2.6: Influence of solution pH on photocatalytic decomposition efficiency of various pollutant using different photocatalytic.

Pollutant	Photocatalyst	Light source	pH range	Optimum pH	Removal efficiency (%)	References
RhB	Ni-BiOCl	Visible light	3.0-11.0	3.0	98	(Attri et al., 2023)
Reactive blue (RB-220)	PANI/BiOCl	Visible light	3.0-11.0	3.0	99.2	(Mansor et al., 2021)
CIP	BiOCl-Bi ₁₂ O ₁₇ Cl ₂	Visible light	3.0-11.0	3.0	97	(Long et al., 2020)
Phenol	BiOCl-1%Fe-350	Visible light	2.8-8.5	2.8	98	(Wu et al., 2022)
Tetracycline	CuO-BiOCl	Visible light	2.0-9.0	4.0	90.3	(Yuan et al., 2022)
POMSE	ZnO-PEG	UV light	4.0-9.0	6.5	73	(Zainuri et al., 2018)
POME	TiO ₂	UV light	4.0-11.0	4.0	53.82	(Arutanti et al., 2020)
POME	ZnO	UV light	3.0-11.0	11.0	27	(Affam & bin Bistar, 2020)
POME	Boron doped-TiO ₂ - SiO ₂ cobalt ferrite	Visible light	3.0-11.0	3.0	100	(Zangeneh et al., 2018)

Attri et al. (2023) mentioned that 98% of photocatalytic decomposition performance of RhB was achieved by employing Ni-BiOCl under visible light irradiation at pH 3.0 as optimum value. This was described by a large amount of negatively charged RhB anionic dye can be attracted onto the positively charged photocatalyst surface at low pH, leading to better photocatalytic decomposition efficiency. Wu et al. (2022) tested the effect of solution pH (2.8-8.5) on the visible light irradiated phenol applying BiOCl-1%Fe-350 as photocatalyst. The optimum photocatalytic decomposition efficiency of 98% was achieved under solution pH of 2.8. They stated that, the leaching of iron occurred at pH 2.8 thus the leached iron cations could possibly involve in photocatalytic process and enhanced to the further phenol degradation. Yuan et al. (2022) studied the photocatalytic activity of CuO/BiOCl over tetracycline degradation under visible light irradiation, which achieved the optimum degradation efficiency 90.3% at pH 4.0 as compared to alkaline conditions. Referring to Long et al. (2020), 97% of photocatalytic decomposition of CIP was achieved using BiOCl-Bi₁₂O₁₇Cl₂ under visible light irradiation at optimum pH of 3.0 among the pH (3.0-11.0). In addition, Mansor et al. (2021) revealed that 99.2% of photocatalytic degradation efficiency of reactive blue (RB-220) was obtained by applying PANI/BiOCl under visible light irradiation at pH 3.0 as optimum pH value. They explained the pH affecting the adsorption and desorption of dye molecules as well as electron-hole pairs separation. Whereas in acidic condition, the electron density of the anionic dye has been declined by the interactions of H⁺ with azo bond of RB-220. On the other hand, while in the alkaline conditions, the adsorption of hydroxyl radical created a negatively charged surface that reduced the

interactions of anionic dye molecules led to decrease in photocatalytic performance.

Arutanti et al. (2020) studied the photocatalytic decomposition efficiency of POME by TiO₂ under UV light irradiation within the solution pH range from 4.0-11.0. The optimal solution pH was 4.0 with 54% of POME removal. They mentioned that the poor photocatalytic efficiency at alkaline conditions attributed to the less efficient pollutant-photocatalyst adsorption due to the incompatible surface charge respectively. In another research, Affam and Bistar (2020) revealed that the application of ZnO in POME photocatalytic degradation under UV light irradiation over a variety of pH range, which are ranging from 3.0 to 11.0. They claimed that ZnO worked less effective under alkaline condition due to the repulsion of both negatively charged photocatalyst and POME, which credited to the less effective absorption of POME into photocatalyst thus led to poor photocatalytic degradation.

2.5.3 Initial Contaminant Concentration

The initial contaminant concentration is one of the significant process factors in photocatalytic decomposition performance. The removal performance reduced with the increasing of initial contaminant concentration. The abundant initial contaminant concentration minimal the path length of photo travelling into the contaminant solution (Mahmoodi & Saffar-Dastgerdi, 2019). Additionally, redundant amount of contaminant molecules in high concentrations can adhere in more active sites, thus declining the generation of ROS and consequently minify the photocatalytic decomposition performance (Alam et al., 2018; Nahar et al., 2019).

Mohsen et al. (2021) studied the photocatalytic decomposition of Congo Red by CQDs/BiOCl under visible light irradiation within the range of initial dye pollutant concentration of 5 to 30 ppm. The optimal concentration was tested to be 10 ppm which achieved 97%. The increase of initial concentration reduced the rate of light penetration inside the solution, which caused to the reduced in ROS generation and poor photocatalytic decomposition efficiency. Referring to Rashid et al. (2020), 100% of removal efficiency of diclofenac sodium was attained using BiOCl-GO under UV light at an optimal initial pollutant concentration of 5 ppm among 5 ppm to 25 ppm. In addition, Huang et al. (2021) investigated the photocatalytic degradation of RhB over Pt-BiOCl/rGO under visible light irradiation, whereas the optimum initial dye concentration of 50 ppm among 40-60 ppm obtained the highest photocatalytic degradation up to

98%. Besides, Zhu et al. (2022) studied the photocatalytic degradation performance of CIP over $0.7\text{Bi}^0\text{-BiOCl/WO}$ under visible light. The optimum initial CIP concentration with 15 ppm stands up among 5-25 ppm achieved 95% of CIP photocatalytic degradation. In addition, Gupta and Kansal (2019) demonstrated the photodegradation of levofloxacin with $\text{Bi}_3\text{O}_4\text{Cl/BiOCl}$ under visible light irradiation with the optimum initial concentration of levofloxacin at 10 ppm among 10-30 ppm. The highest levofloxacin photodegradation efficiency achieved up to 87%. They claimed that the photodegradation reduced at concentration beyond optimum level was due to the light scattered by the obstacles.

Furthermore, Ng and Cheng, (2017) stated that 52% removal of POME attained by TiO_2 with an ideal initial POME concentration of 250 ppm under UV light irradiation. They claimed that the higher concentration of POME increased the colour intensity simultaneously that limiting the accessing of UV light. According to Zainuri et al (2018), the effect of initial concentration of POME from 100 to 280 ppm was studied by employing ZnO-PEG as photocatalyst under UV light irradiation. The results demonstrated that the photocatalytic POME treatment efficiency reduced at high concentrations, which was due to the insufficient ROS generation to degrade POME. Finally, Table 2.7 displays the critical influence of initial contaminant concentration on photocatalytic decomposition performance of assorted contaminants.

Table 2.7: Effect of initial contaminant concentration on the photocatalytic decomposition of various organic pollutant.

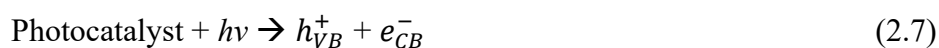
Pollutant	Photocatalyst	Light source	Initial concentration (ppm)	Optimum concentration (ppm)	Removal efficiency (%)	References
Congo Red	CQDs/BiOCl	Visible light	5-30	10	97	(Mohsen et al., 2021)
RhB	Pt-BiOCl/rGO	Visible light	40-60	50	98	(Huang et al., 2021)
Diclofenac sodium	BiOCl-GO	UV light	5-25	5	100	(Rashid et al., 2020)
CIP	0.7Bi ⁰ -BiOCl/WO	Visible light	5-25	15	95	(P. Zhu et al., 2022)
Levofloxacin	Bi ₃ O ₄ Cl/BiOCl	Visible light	10-30	10	87	(Gupta & Kansal, 2019)

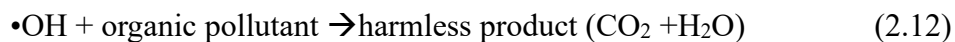
Table 2.7: Effect of pollutant initial concentration on the photocatalytic decomposition performance pollutant. (continued)

Pollutant	Photocatalyst	Light source	Initial concentration (ppm)	Optimum concentration (ppm)	Removal efficiency (%)	References
2,4,6-trichlorophenol	BiOClBr	Visible light	10-50	10	92.3	(Li et al., 2021)
Ammonium	BiOCl	UV light	10-50	10	100	(Z. Yan et al., 2021)
POME	TiO ₂	Visible light	100-400	240	52	(Ng & Cheng, 2017)
POME	ZnO-PEG	UV light	100-280	190	94	(Zainuri et al., 2018)
POME	ZnO	UV light	100-400	250	52	(Ng et al., 2016)

2.6 Influence of H₂O₂ Introduction

The ability of hydrogen peroxide to act as an electron scavenger makes it a powerful tool in a variety of chemical and biological processes. When H₂O₂ is present in the photocatalytic system, the photogenerated electrons in the conduction band of the photocatalyst can reduce H₂O₂ to form hydroperoxyl radicals ($\bullet\text{OOH}$) or hydroxyl radicals ($\bullet\text{OH}$), depending on the pH of the solution. The hydroperoxyl radicals and hydroxyl radicals can then react with organic pollutants in the solution and degrade them through oxidation. At the same time, H₂O₂ can act as an electron scavenger by accepting electrons from the conduction band of the photocatalyst, which can reduce the rate of electron-hole recombination and enhance the efficiency of the photocatalytic process. The photogenerated holes in the valence band of the photocatalyst can oxidize H₂O₂ to form hydroxyl radicals ($\bullet\text{OH}$), while the photogenerated electrons in the conduction band can reduce H₂O₂ to form water (H₂O). In biological systems, hydrogen peroxide plays a key role in the photocatalytic system by helping to kill invading bacteria and other pathogens through a process called oxidative burst, in which it acts as an electron scavenger to produce reactive oxygen species that are toxic to the pathogen. The overall reaction can be represented as follows:





There are several studies regarding the effect of H₂O₂ dosage on the photocatalytic decomposition performance of pollutant. For instances, Pham et al. (2019) reported that 100% removal of MB attained by BiVO₄ with an ideal H₂O₂ dosage of 0.001 mmol/L under visible light irradiation. However, the decrease in H₂O₂ dosage to 10⁻⁶ mmol/L ineffective as of the insufficient of •OH. In addition, Feilizadeh et al. (2019) stated that the 2-nitrophenol obtained an optimum 80% of 2-nitrophenol photodegradation over Ag-S/PEG/TiO₂ with the optimum H₂O₂ dosage of 325 mmol/L under solar irradiation. Nevertheless, the 2-nitrophenol photodegradation declined with the increase of H₂O₂ concentration. This was due to the excessive H₂O₂ molecules involved as •OH scavengers to form hydroperoxyl radicals such as •OOH that possessed fewer oxidizing power and can also act as scavengers of other •OH and •OOH. Besides, Jiao et al. (2019) demonstrated a complete photodegradation of RhB with AgNPs-IN-CNTs alongside with the presence of H₂O₂ under visible light irradiation. The optimum H₂O₂ concentration was 30 mmol/L, they stated the H₂O₂ was acted as an electron acceptor to produce •OH radicals for accelerating the degradation. Moreover, Cao et al. (2021) showed a 98% photodegradation of methylene blue via 0.15 ZnFe₂O₄/BiVO₄ with the presence of 50 x 10⁻⁶ L of

H₂O₂ under visible light irradiation. They claimed that the synergistic degradation of methylene blue by the heterojunction photocatalysts and H₂O₂ as it served as e^- receiver thus produced •OH radicals which can degrade organic pollutant. Additionally, Lee et al. (2019) investigated 2,4,5-trichlorophenoxyacetic acid and achieved 82.4% of photodegradation efficiency over Eu-BiWO₆ with the presence of H₂O₂ under visible light irradiation. They also found that the optimum H₂O₂ concentration was 0.2%. However, the concentration of H₂O₂ above 0.2% declined the photodegradation of 2,4,5-trichlorophenoxyacetic acid as the excessive amount of H₂O₂ acting as •OH radical scavenger, and to form •OOH radicals that have less oxidizing power as compared to •OH radical.

On the other hand, Nawaz et al. (2022) studied the effect of H₂O₂ concentration on phenol degradation. They claimed that the optimal H₂O₂ concentration at 90 mmol/L, if the H₂O₂ concentration beyond 90 mmol/L, it caused scavenging effect and reduced the removal rate of organic compounds. Rahman, et al. (2021) demonstrated a 82% of POME photocatalytic degradation over CNB-TiO₂ under UV light irradiation with the presence of optimal 2.0 mmol/L H₂O₂ concentration. They concluded that the H₂O₂ minimized the recombination of charge carriers by intercepting the e^- in the CB of CNB-TiO₂, and amplified the •OH radicals generation in CNB-TiO₂ for photodegradation. At last, Table 2.8 demonstrates the impact of H₂O₂ dosage on photocatalytic decomposition of different pollutants.

Table 2.8: Effect of hydrogen peroxide dosage on the photocatalytic decomposition of various organic pollutant.

Pollutant	Photocatalyst	Light source	H₂O₂ dosage range (mmol/L)	H₂O₂ dosage (mmol/L)	Removal efficiency (%)	References
Methylene Blue	BiVO ₄	Visible light	0 ~ 1	0.001	100	(Pham et al., 2019)
Methylene Blue	ZnFe ₂ O ₄ /BiVO ₄	Visible light	-	50 x 10 ⁻⁶	100%	(Cao et al., 2021)
2-nitrophenol	Ag-S/PEG/TiO ₂	Sunlight	0 ~ 500	325	80	(Feilizadeh et al., 2019)
RhB	AgNPs-in-CNTs	Visible light	5 ~ 30	30	100%	(Jiao et al., 2019)
2,4,5-trichlorophenoxyacetic acid	Eu-doped Bi ₂ WO ₆	Visible light	0 – 0.33%	0.2%	80%	(Lee et al., 2019)
POME	ZnO	UV light	Molar ratio (0.5 – 50)	Molar ratio of 5	~ 60%	(Affam & bin Bistar, 2020)

Table 2.8: Effect of hydrogen peroxide dosage on the photocatalytic decomposition of various organic pollutant. (continued)

Pollutant	Photocatalyst	Light source	H₂O₂ dosage range (mmol/L)	H₂O₂ dosage (mmol/L)	Removal efficiency (%)	References
Phenol	Core-shell structured black TiO ₂	Visible light	30~150	90	~ 93%	(Nawaz et al., 2022b)
POME	FeSO ₄	UV light	100-3000 mg/L	400 mg/L	~90%	(Arutanti et al., 2020)
POME	CNB-TiO ₂	UV light	1.0-10.0	2.0	~84%	(Rahman, et al., 2021)

2.7 Photocatalytic Inactivation on Microorganism

E. coli is gram negative and rod-shaped bacterium (Foster-Nyarko & Pallen, 2022). *B. cereus* is a Gram-positive, rod-shaped, and spore-forming facultative. (Bağcıoğlu et al., 2019) The existence of *E. coli* in real wastewater including POME, urban and municipal wastewater has been justified and published in literatures (Misrol et al., 2021). *E. coli* could impose a potential threat to human health and food safety even at low concentration (Ungureanu et al., 2020). The *E. coli* can be spread through raw water supply, raw meat and undercooked meat, food, vegetables, and the usage of common effortlessly, thus leading it highly spreadable and given greater chances of sparking an epidemic (Lagerstrom & Hadly, 2021). It can lead to various of intestinal illnesses for instances cholecystitis, peritonitis and diarrhoea (Okocha et al., 2018). Nevertheless, is reliant on the person immunologic state or the strain virulence, long term or fatal illness could happen (Martinson & Walk, 2020). Thus, it important to eliminate *E. coli* in wastewater prior dispose to the ecosystem.

Thus, it is a crucial step to eliminate pathogen from water reservoir. Photocatalytic bacterial inactivation was carried out to suppress the *E. coli* under the presence of light and photocatalysts. As Bi-based photocatalyst exhibited stable antibacterial effect on antibacterial activities against a wide range of non-pathogenic and pathogenic microorganisms for instances Huang et al. (2021) developed a visible-light-driven 3D Bi₅O₇I/BiOCl microsphere heterojunctions with great antibacterium performance against *E. coli*, which generated the strong •OH radicals under sunlight irradiation. The induced •OH radicals able to ruin

the cell membrane of bacteria and further limited the growth of bacteria. Besides, Padervand et al. (2019) reported that a novel quaternary BiOCl/AgCl-BiOI/AgI nanocomposite that able to inhibit the growth of *E. coli* and *S. aureus*. The growth of bacteria became unnoticeable after 5 hr of visible light irradiation. Recently, Liu et al. (2021) demonstrated BiOCl microspheres as photocatalysts for efficient removal of multidrug-resistant bacteria. To investigate the antibacterial capability of the microspheres, they employed *P. aeruginosa* multidrug-resistant strain NKP2-NKP5 and standard strain PAO1, the *S. aureus* multidrug-resistant strain NKS1-NKS2 as well as *E. coli* multidrug-resistant strain NKE2 and NKE3. At the end of the experiments, it displayed a strong inactivation of every employed bacteria species especially the multidrug-resistant strain. In addition, there are some examples of 3D flower like Bi₃O₄Cl/BiOCl, BiOCl/Bi₂Ti₂O₇, Ag/BiOCl/diatomite, Pt-loaded BiFeO₃ were applied to deactivate *E. coli*, *S. aureus*, and *K. pneumonia* (Chen et al., 2021; Gupta & Kansal, 2019a; Jaffari et al., 2019; Niu et al., 2020).

During photocatalytic bacterial inactivation, photocatalyst can produce abundance ROS, which are highly reactive and interacted with bacteria organelles. The reaction began with the adsorption of photocatalysts onto the cell membrane of bacteria followed by the release of ROS that aggressive and penetrate the bacteria finally killed the bacteria. The production of ROS by different photocatalysts has been revealed to be significant in photocatalytic inactivation to cause lethal destruction of bacteria organelles. The ROS species were known to cause oxidative stress by damaging DNA, cell membranes and cellular proteins (Gowda et al., 2022). The lysis of bacteria cell wall can be

attributed to the surface activity of photocatalyst which rooted the rupture of the cell membrane, consequently the exposure of cell organelles and eventually killed the bacteria (Patial et al., 2022). In contrary, the release of radical ions such as $\bullet\text{OH}$, $\text{O}_2\bullet^-$, H_2O_2 and e^- ions from photocatalyst would be feasible explanation for the photocatalytic inactivation (Baaloudj et al., 2021). The radical ions can be adhered on the bacteria cell membrane surface. Afterwards, the collision between bacterial cell membrane and metal ions allowed the metal ions penetrating bacteria effortlessly and reacted with the functional groups on bioactive proteases inclusive of sulfhydryl, amino and amino groups to modify the structure and performance of proteases, which root for unstable metabolism that eliminate the bacteria (Liu et al., 2021) .

There were several Bi-based photocatalysts have been employed for photocatalytic antibacterial investigations. For instances, Vignesh et al., 2018 reported that antibacterial efficiency (ZOI) was 17 mm for *E.coli* and 18 mm for *S. aureus* under visible light irradiation for 140 min over g-C₃N₄/BiFeO₃/CuO. Besides that, Shanmugan et al., 2020 reported that g-C₃N₄/Bi₂MoO₆/Ag testified antibacterial efficiency (ZOI) with 20 mm and 18 mm for *E. coli* and *S. aureus*, respectively under visible light irradiation. On the other hand, Qureshi et al., 2020 reported that CdS/Bi₂S₃ gained the ZOI of 16 mm and 18 mm under UV light irradiation for *E. coli* and *S. aureus* respectively. Finally, Table 2.9 displays a brief comparison of organic pollutants and microorganism inactivation over different Bi-based photocatalysts.

Table 2.9: Brief comparison of organic pollutants and microorganism inactivation over different Bi-based photocatalysts.

Photocatalyst	[Pollutant]	Catalyst loading	Light source	Time (min)	Degradation (%)	Bacteria species	Antibacterial efficiency (ZOI)	References
g-C ₃ N ₄ /BiFeO ₃ /CuO	5 mg/L Rhodamine B	0.5 g/L	500 W visible light	140 min	98.5%	<i>E. coli</i> <i>S. aureus</i>	17 mm 18 mm	Vignesh et al., 2018
Bi ₂ O ₃	50 mg/L Tartrazine	3 g/L	10 W UV light	140 min	85 %	<i>E. coli</i>	13 mm	El-Batal et al., 2017
g-C ₃ N ₄ /Bi ₂ MoO ₆ /Ag	30 mg/L Methylene blue	0.5 g/L	500 W visible light	80 min	99.6%	<i>E. coli</i> <i>S. aureus</i>	20 mm 18 mm	Shanmugam et al., 2020
g-C ₃ N ₄ -MoS ₂ /Bi ₂ O ₃	20 mg/L Methylene blue	50 mg	500 W visible light	90 min	98.4%	<i>E. coli</i> <i>S. aureus</i>	11 mm 12 mm	Shanmugam et al., 2020
CdS/Bi ₂ S ₃	10 mg/L Methyl orange	1 g/L	300 W UV-visible light	120min	~65%	<i>E. coli</i> <i>S. aureus</i>	16 mm 18 mm	Qureshi et al., 2020

2.8 Summary of Literature Review

Scientific investigations have been performed on photocatalytic treatment of pre-treated POME using different photocatalytic materials, however, no investigation has been carried out on the decorating BaFe₂O₄ on BiOCl as Z-scheme photocatalysts in POME treatment. Especially, the analytical assessment on the ROS generation for photocatalysts and suitable band positions of both semiconductors for a Z-scheme photocatalytic mechanism were inspected in detail. Moreover, the effects of operating parameters including photocatalyst loading, solution pH and initial POME concentration have been investigated in this study. BiOCl-based photocatalysts have also been recognised as effective photocatalysts to inactivate bacteria in water. The antibacterial performance of BaFe₂O₄/BiOCl towards *E.coli* and *B. cereus* have been investigated for the first time in this study. These are the challenges in the BaFe₂O₄/BiOCl photocatalysis and all stated above will be evaluated in order to subdue the constraints noticed in this review.

CHAPTER 3

METHODOLOGY

3.1 Flowchart

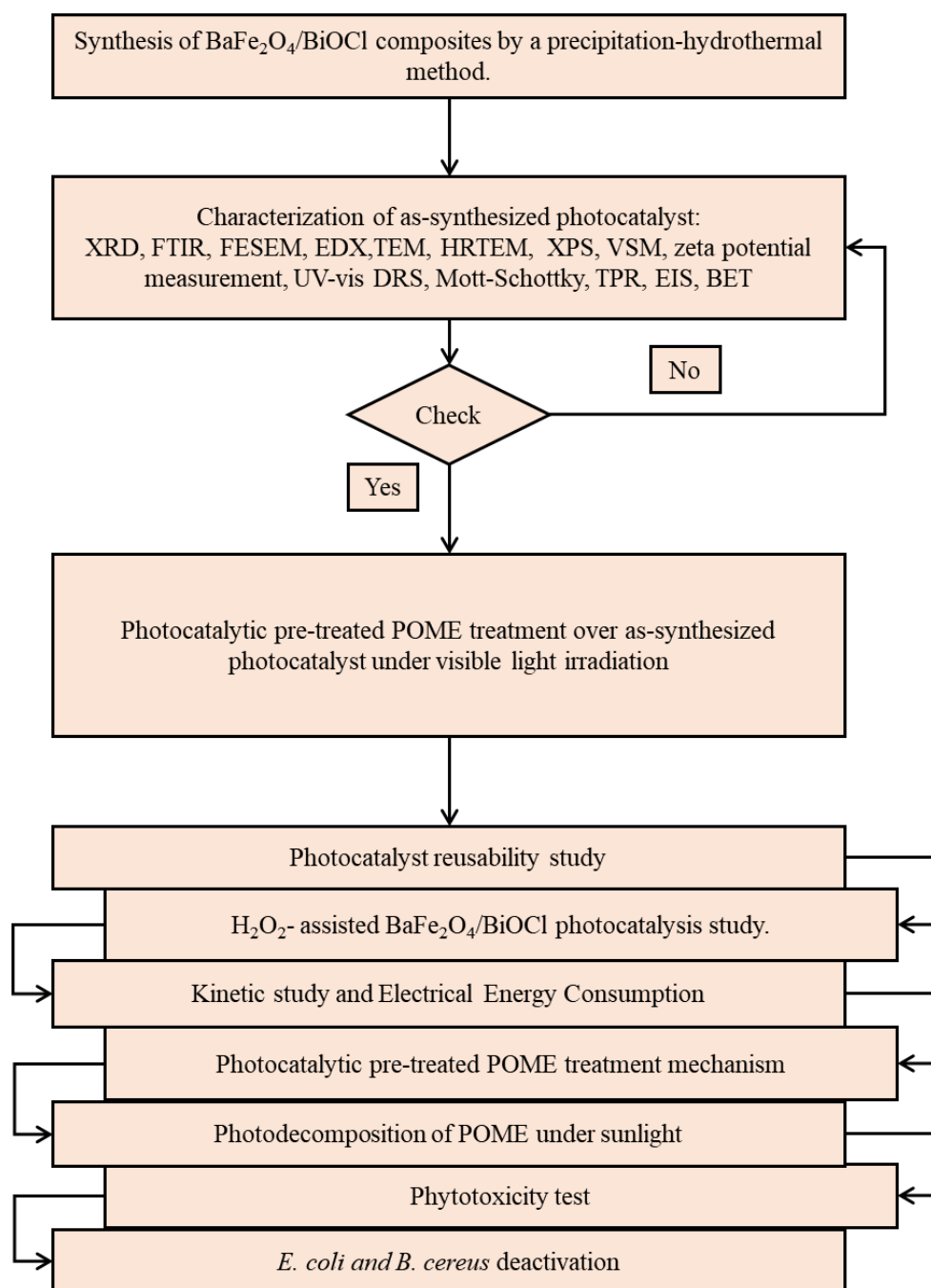


Figure 3.1: Flowchart of involved research methods in this study.

3.2 Materials and Chemical Listing

Table 3.1 lists the chemicals and materials employed in the current study. The chemicals employed are of analytical grade and were utilized as received without undergoing additional purification processes.

Table 3.1: List of Chemicals Utilized

Chemicals/ Reagents	Purity (%)	Supplier	Purpose
Bismuth nitrate pentahydrate ($\text{Bi}(\text{NO}_3)_3 \cdot 6\text{H}_2\text{O}$)	≥ 98.0	Synerlab	Photocatalyst preparation
Potassium chloride (KCl)	$\geq 99.5\%$	Qrec	Photocatalyst preparation
Barium nitrate ($\text{Ba}(\text{NO}_3)_2$)	$\geq 99.0\%$	System	Photocatalyst preparation
Iron nitrate nonahydrate	$\geq 99.0\%$	R & M Chemical	Photocatalyst preparation
Polyvinylpyrrolidone	$\geq 99.0\%$	Qrec	Photocatalyst preparation
Ethylene glycol	$\geq 99.5\%$	R & M Chemical	Photocatalyst preparation
Ethanol	$\geq 96.6\%$	Lab serv	Photocatalyst preparation

Table 3.1: List of Chemicals Utilized (continue)

Chemicals/ Reagents	Purity	Supplier	Purpose
Sodium hydroxide (NaOH)	≥98.0	Acros Organic	pH adjustment
Sodium Sulfate Anhydrous	≥98.0	Friendeman n Schmidt	Electrolyte solution in photochemical analysis
Isopropanol (IPA)	≥99.8%	ChemSola	Reactive oxygen species scavenger analysis
p-benzoquinone (BQ)	≥98.0%	Acros Organic	Reactive oxygen species scavenger analysis
Ethylenediaminetetraacetic acid sodium salt (EDTA-2Na)	≥99.0%	System	Reactive oxygen species scavenger analysis
Sodium chloride (NaCl)	≥95.0%	System	Antibacterial bacterial analysis
Nutrient broth	-	Himedia	Antibacterial bacterial analysis
Nutrient agar	-	Himedia	Antibacterial bacterial analysis

3.3 Photocatalysis Experiment Setup

The batch reaction system used in the experiment is schematically illustrated in Figure 3.2. The photocatalytic experiments were performed in a quartz tube photoreactor. The photoreactor was made of quartz with dimensions of 45 mm x 12.5 mm x 12.5 mm. A 150W LED lamp supplied by Jay Lighting, China was employed as a light source with 5 cm aside of the reaction mixture. The intensity of light reached the surface of the reaction mixture was approximately 45,000 lx., as assessed by a digital luxmeter (LX-101, EOSUN). The quartz tube and lamp were setup inside an acrylic black box to prevent ambient light entering the reaction mixture. An air pump with 1.0 L/min aeration was used to supply air into the photoreaction throughout the experiment as well as to ensure the homogeneous mixing of photocatalyst. Furthermore, cooling fans were installed and applied in the system as to maintain at room temperature and avoid any thermal catalytic effect.

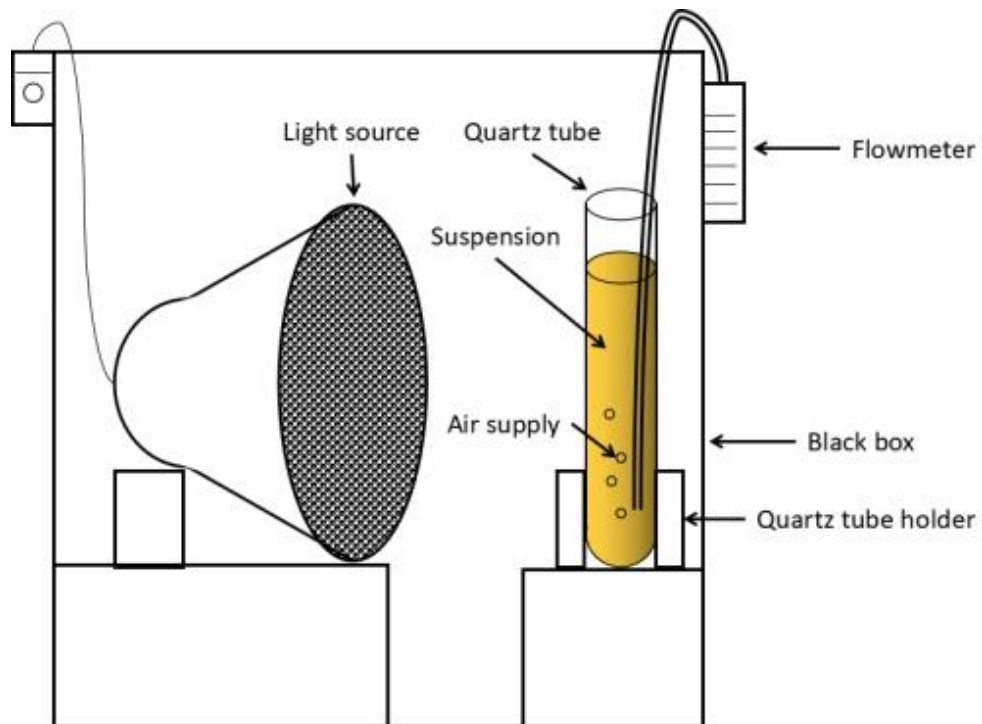


Figure 3.2: Schematic diagram of photocatalytic system under visible light irradiation

On the other hand, the photocatalytic experiments under sunlight were conducted on sunny days between 10:00 am to 15:00 pm in March of 2022. The assessed sunlight intensity was about 90,000 lx. The photocatalytic experiments were conducted in a 100 mL quartz tube as illustrated in Figure 3.3. The intensity of UVA and UVC from sunlight was also taken using series 9811 radiometer from Cole-Parmer. The UVA and UVC were defined allocated at 365nm and 254nm, which intensities were 2.0 mW/cm^2 and 1.4 mW/cm^2 respectively.

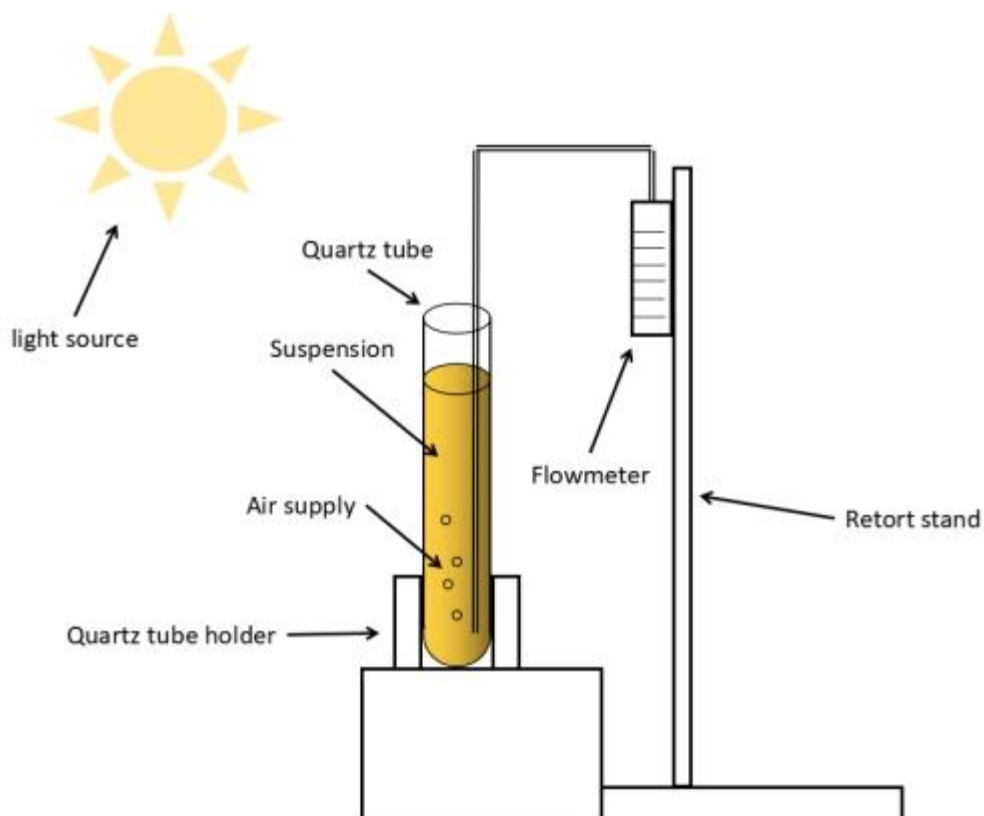


Figure 3.3: Schematic diagram of photocatalytic system under sunlight irradiation

3.4 PREPARATION OF PHOTOCATALYSTS

3.4.1 Preparation of BaFe₂O₄

The aggregated BaFe₂O₄ photocatalyst was synthesized via a chemical precipitation method. Typically, 4.04 g of Fe(NO₃)₃•9H₂O was dissolved into 100 mL distilled water under vigorous stirring for 30 min, which labelled as solution A. At the same time, 1.31 g of Ba(NO₃)₂ was dissolved into 100 mL distilled water under stirring and then labelled as solution B after constant stirring for 30 min. Subsequently, the solution B was added dropwise into solution A and stirred for 30 min. The mixture was heated to 90°C and followed

by the pH adjustment to 12.0 with appropriate amount of 0.01 M NaOH solution. After being stirred for 2 h, the obtained precipitate was filtered, washed several times with ethanol as well as water and finally dried overnight at 60°C.

3.4.2 Preparation of BaFe₂O₄/BiOCl and BiOCl.

The BaFe₂O₄/BiOCl composites were synthesized via a hydrothermal method. Initially, 4.85 g of Bi(NO₃)₃·5H₂O and 0.75 g of KCl were added into 180 mL ethylene glycol solution and stirred continuously for 30 min to obtain homogenized solution. Then, a desired amount of as-fabricated BaFe₂O₄ was added into the above mixture, which was vigorously stirred again for 90 min. The mixture was then shifted into a 200 mL Teflon-lined stainless-steel autoclave to undergo hydrothermal treatment at 150°C for 8 h. The resulted precipitates were filtered, washed several times with ethanol as well as water and finally dried overnight at 60°C. The obtained BaFe₂O₄/BiOCl composites with different BaFe₂O₄ weight ratios of 1, 5 and 10 wt% were denoted as 1 wt% BaFe₂O₄/BiOCl, 5 wt% BaFe₂O₄/BiOCl and 10 wt% BaFe₂O₄/BiOCl. Using the same hydrothermal method, the pure nanosheet BiOCl was prepared without the addition of aggregated BaFe₂O₄. A schematic illustration of the synthetic steps of BaFe₂O₄/BiOCl composites is shown in Figure 3.4.

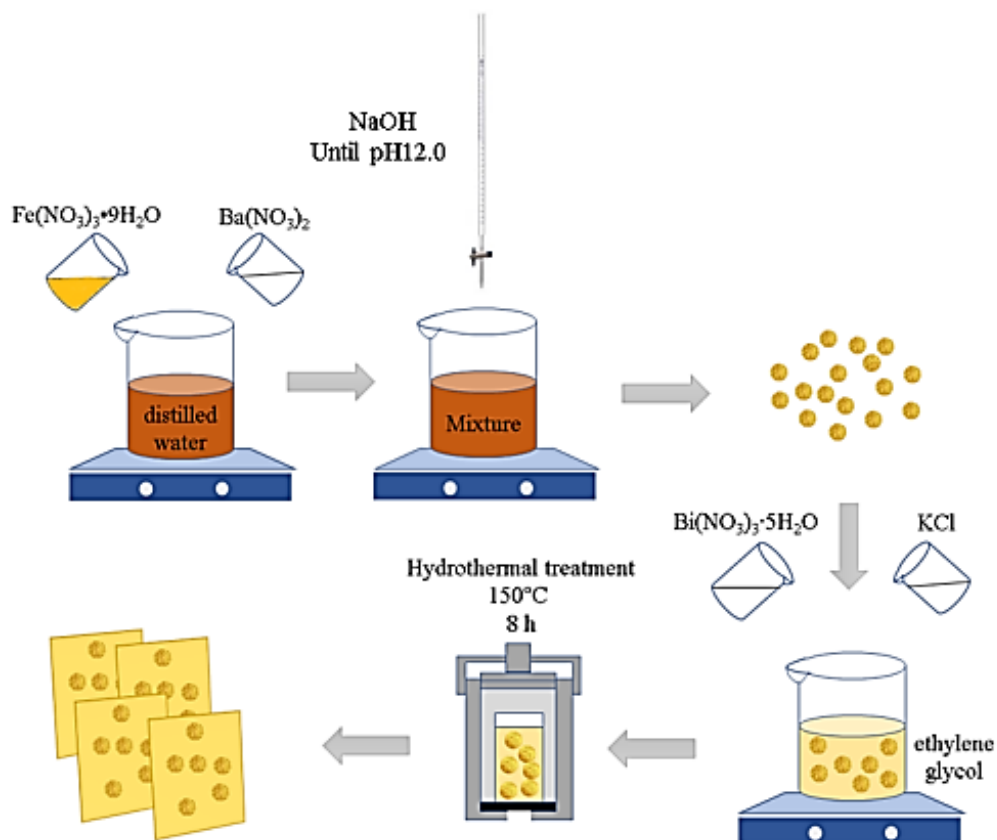


Figure 3.4: Schematic illustration of the synthesis path for BaFe₂O₄/BiOCl composite preparation.

3.5 Characterization of as-prepared photocatalysts

3.5.1 X-ray Diffraction (XRD)

X-Ray Diffraction (XRD) is a non-destructive analytical technique used to determine the crystal structure, chemical composition, and crystalline purity of a material. XRD operates by measuring the diffraction of X-rays by a sample to provide information about the arrangement of atoms within the sample. The XRD pattern was obtained using Philip PW1820 diffractometer from 20° to 60° scanning range, irradiated by Cu K α at 2° min⁻¹ scanning rate ($\lambda = 0.15406$ nm).

XRD analysis was conducted in Faculty of Science (FSc), University Tunku Abdul Rahman (UTAR).

3.5.2 Fourier Transform Infrared Spectroscopy (FTIR)

FTIR (Fourier Transform Infrared Spectroscopy) is a commonly used analytical technique that measures the absorption and transmission of infrared radiation by a sample. It is used to identify and quantify the functional groups and chemical bonds present in a material by analyzing its infrared spectrum. The FTIR analysis was recorded from 400 cm^{-1} to 4000 cm^{-1} wavelengths at 2 cm^{-1} spectral resolution in FSc, UTAR.

3.5.3 Field Emission Scanning Electron Microscopy (FESEM) and Energy Dispersive X-ray (EDX)

FESEM, or Field-Emission Scanning Electron Microscopy, is a type of electron microscopy that uses a field-emission electron source to produce high-resolution imaging of specimens. The operating principle of FESEM is based on the interaction between an electron beam and the surface of the specimen, leading to the generation of secondary electrons. These secondary electrons are then collected and used to form images of the specimen's surface features. The as-synthesized samples were analysed using a *JEOL 6701-F FESEM* at an accelerating voltage of 120 kV. The samples were placed on an adhesive carbon

tape on top of an aluminium stub before coated using a *Jeol JFC-1600 Auto Fine Coater*. This analysis was done in Faculty of Science (FSc), UTAR.

EDX, also known as Energy Dispersive X-ray Spectroscopy, is an analytical technique used in materials science and other related fields for elemental analysis. The method works by bombarding a sample with high energy electrons, which then excites the atoms and causes them to emit X-rays. The X-rays are then analyzed to determine the energy spectrum of the elements present in the sample. A *Jeol JSM 7601-F* equipment coupled with *Oxford Instruments X-Max* Energy Dispersive X-ray Diffractometer was used to perform EDX analysis. This analysis was used to determine elemental composition of products (Fadli et al., 2021) The samples were undergone with identical preparation steps as FESEM analysis. The EDX spectra and elemental images was done in FSc, UTAR.

3.5.4 Transmission Electron Microscopy (TEM)

TEM applied to investigate the morphology of solid photocatalyst at higher resolution. The TEM image was snapped with a Tecnai 20 microscope operated at 200 kV. The samples were firstly prepared by suspending a small quantity of sample powder in ethanol and vigorously shaking it for a few seconds before analysis. The suspensions were left to settle and allow the coarser particles for sedimentation. After that, a small amount of the prepared sample was collected and applied onto a copper grid coated with a carbon film.

The sample powders were dried aside then the grid was mounted on the specimen holder of the electron microscope for assessment. The TEM analysis was done at MIMOS Nano Semiconductor Technology Centre, MIMOS Berhad.

3.5.5 X-ray Photoelectron Spectroscopy (XPS)

X-ray Photoelectron Spectroscopy (XPS) is a surface-sensitive analytical technique used to determine the chemical composition and electronic structure of materials. It works by bombarding the sample with high-energy X-rays, causing electrons to be ejected from the inner shells of the atoms in the sample. These photoelectrons are then analyzed according to their kinetic energy, which provides information about the binding energy of the electrons, and the elemental and chemical state of the material. Surface chemical state of as-prepared composite were examined using XPS (Akika et al., 2020). The surface of the fine sample was excited with monochromatized aluminum radiation ($Al-K\alpha$) of 1487 eV in low vacuum pressure condition of 10^{-8} Pa. The XPS analysis was conducted using a *PHI Quantera II* Scanning XPS Microprobe in MIMOS Nano Semiconductor Technology Centre, MIMOS Berhad.

3.5.6 Vibrating Sample Magnetometer (VSM)

Vibrating Sample Magnetometer (VSM) is an analytical instrument used to measure the magnetic properties of a material, particularly the magnetic susceptibility and magnetic moment of ferromagnetic, paramagnetic, and diamagnetic materials (Nasrollahzadeh et al., 2019). The operating principle of VSM is based on the interaction between the magnetic moment of a sample and the magnetic field produced by a permanent magnet or electromagnet. The sample preparation for magnetic property measurements involved preparing the sample in a thin, flat shape and placing it in the sample holder. The instrument was then turned on and the magnetic field was set to the desired value. During the measurement, the sample was subjected to a magnetic field, and the change in magnetic field caused by the magnetic moment of the sample was measured and recorded as a function of frequency. Finally, the collected data was analyzed and processed to determine the magnetic properties of the sample, such as magnetic susceptibility and magnetic moment (H. Singh et al., 2020). The VSM analysis was conducted using a Quantum Design MPMS-5S VSM at SIRIM Berhad.

3.5.7 Zeta Potential Measurement

The photocatalyst's point of zero charge was determined by measuring the zeta potential at the point where it was zero (Hiremath et al., 2021). The zeta potential analysis was performed via a Molvern Zetastar Nano Z. 0.02 g of

sample powders was added in deionized water and adjusted to pH 2, 3, 4, 5, 6, and 7, which then inserted into a fold capillary all for testing. This assessment was conducted in School of Chemical Engineering, Universiti Sains Malaysia.

3.5.8 Ultraviolet-Visible Diffuse Reflectance Spectroscopy (UV-vis DRS)

UV-vis DRS refers to an analysis of the investigating the interaction of a sample and ultraviolet and visible light. During measurement, the sample is placed in the sample compartment and the range of UV-vis light was scanned to measure the optical properties. The UV-vis DRS analysis was carried out using a *Jacso V730* (J. Jiang et al., 2019). The products were dispersed in 10mL distilled water and ultrasonicated for 15 min. The spectra were recorded in the range of 350–700 nm timely using BaSO₄ as a reference standard. The band gap energies of products were calculated according to Equation 3.5. The analysis was done in Faculty of Engineering and Green Technology (FEGT), UTAR.

3.5.9 Photoelectrochemical experiments

The photoelectrochemical assessment were carried out using a Gamry Interfere 1000 electrochemical workstation equipped with a standard three-electrode system. The counter electrode was made of platinum foil, the reference electrode was Ag/AgCl, and the working electrode was fluorine-doped tin oxide (FTO) glass coated with the synthesized photocatalysts. All

electrodes were immersed in a 0.5 M Na₂SO₄ electrolyte solution and illuminated with a 150 W LED lamp. The transient photocurrent response spectra were recorded during multiple 30-second on-off cycles at a bias potential of 0.4 V vs Ag/AgCl. Additionally, the electrochemical impedance spectroscopy (EIS) spectra of the samples were obtained in the 0.1 Hz frequency range. This analysis was conducted at the Faculty of Science (FSc), UTAR..

3.5.10 Specific Surface Area (SSA)

The SSA analysis was performed to justify the photocatalytic surface active site on samples (Ajala et al., 2018). SSA was measured at 77K employing a *Micromeritics ASAP 2020* N₂ adsorption equipment. The examined samples were weighed and filled into a sample holder with a seal frit. The sample holder was degassed at 300°C under vacuum condition before start. The SSA analysis was performed in Quantum Skynet Resources Sdn. Bhd..

3.5.11 Mott-Schottky

Mott-Schottky analysis is a technique used to measure the conduction band potential (E_{CB}). The sample for Mott-Schottky analysis was thoroughly cleaned and polished to ensure a flat surface free of contaminants. The analysis required two electrodes, one being a metal serving as the counter electrode and the other being a thin film of the sample material. The capacitance of the sample

was measured by applying a small AC voltage and measuring the resulting current. The capacitance data was plotted as a function of the applied voltage to create the Mott-Schottky plot, with the slope being the E_{CB} of the semiconductor. Particularly, the valence band (VB) potential was determined by adding the value of the band gap (E_g) and (E_{CB}) and E_{CB} as shown in Equation 3.1.

$$E_{VB} = E_{CB} + E_g \quad (3.1)$$

This analysis was done via a Gamry Interfere 1000 electrochemical workstation in Faculty of Science (FSc), UTAR.

3.6 Photocatalytic Pre-Treat POME Treatment Under Visible Light Irradiation and Sunlight

The photocatalytic activities of as-synthesized photocatalysts were conducted in batch reaction system under visible and sunlight irradiation, which demonstrated in Figure 3.2 and 3.3 separately. To start an experimental run, a 80 mL substrate solution and weighted photocatalyst were loaded into a quartz tube. Air was supplied into the solution at a constant flow rate of 1 L/min during all experiments. Due to the tall design of the quartz tube, the solution was continuously agitated with the aided of upflowing bubbles. Prior to photocatalytic activity, the mixture solution was blended in dark for 30 min, and then exposed to light irradiation. After a specific time interval, sample solution was taken from the reactor, centrifuged, and filtered using 0.45 μm PTFE

syringe filters before being subjected to analysis. The photocatalytic decomposition performances were estimated using the following formula:

$$\text{Pre-treated POME decomposition (\%)} = \frac{C_0 - C_t}{C_0} \times 100\% \quad (3.2)$$

where C_0 is the equilibrium concentration of POME and C_t is the concentration of pre-treated POME at reaction time, t (min). To weigh against the performance of the enhanced photocatalysts, photocatalytic evaluation was also conducted on pure BaFe_2O_4 and pure BiOCl by employing the same experimental conditions. The POME was obtained from Tian Siang Palm Oil Mill, Air Kuning, Perak.

3.6.1 Effect of BaFe_2O_4 Loading

In order to gain the optimum BaFe_2O_4 loading on the photocatalyst preparation, The photocatalytic performance of different BaFe_2O_4 loadings on BiOCl , namely x wt% $\text{BaFe}_2\text{O}_4/\text{BiOCl}$ ($x = 1, 5, \text{ and } 10$) were studied on the photocatalytic decomposition of pre-treated POME under LED light irradiation. All experiments were conducted with: photocatalyst loading = 0.5 g/L, [pre-treated POME] = 50 ppm and solution pH = 7.0.

3.6.2 Effect of Photocatalyst Loading

The impact of photocatalyst loading was evaluated in the range of 0.25 – 1.0 g/L on the degradation of pre-treated POME (Charles et al., 2019). All experiments were conducted with: [pre-treated POME] = 50 ppm and solution pH = 7.0.

3.6.3 Effect of Solution pH

The impact of solution pH on the photocatalytic pre-treated POME treatment was evaluated, in the range of 2.0 to 9.0 (Alkaykh et al., 2020a), the pH adjustments were made by incorporating 2.0 M HNO₃ or 2.0 M NaOH. All experiments were conducted with: photocatalyst loading = 0.5 g/L and [pre-treated POME] = 50 ppm.

3.6.4 Effect of Initial POME Concentration

The impact of initial POME concentration on the pre-treated POME treatment was explored in the range of 50 ppm to 125 ppm (Wang et al., 2022). All experiments were conducted with: photocatalyst loading = 0.5 g/L, and solution pH = 7.0.

3.6.5 Photocatalyst Reusability

The photocatalytic performance of the recycled photocatalysts was evaluated by employing the identical method described in Section 3.5 for the pre-treated POME decomposition. Four consecutive cycles were carried out, with each cycle lasting 210 minutes. After each cycle, the photocatalysts were magnetically removed, cleaned with deionized water and dried out at 60°C for 12 h. The recycled trials were carried out on the freshly created pre-treated POME solution with the photocatalyst loading of 0.5 g/L, concentration of 50 ppm and solution pH of 2.0.

3.6.6 Effect of H₂O₂ Addition

The impact of the incorporation of hydrogen peroxide (H₂O₂) into the BaFe₂O₄/BiOCl photocatalytic system was studied by varying the concentration of H₂O₂ in the range of 0, 2, 3 and 4 mmol/L. All experiments were conducted with: photocatalyst loading = 0.5 g/L, and solution pH = 7.0.

3.6.7 Screening of Reactive Oxygen Species (ROS)

The screening of ROS such O₂•⁻, •OH radicals and photogenerated positive charged hole (h⁺) involved in the photocatalytic reaction were justified by radical scavenging tests in this research. Detection of ROS involved in the experiment was conducted by blending 2 mM of each distinct scavengers with

identical steps of the photocatalytic experiment (Jaffari et al., 2019). The presence of $O_2^{\bullet-}$, h^+ and $\bullet OH$ were detected with introduction of p-benzoquinone (BQ), ethylenediaminetetraacetic acid disodium salt (EDTA-2Na) and isopropanol (IPA) respectively (Dursun et al., 2020; Phuruangrat et al., 2021; Qin et al., 2019).

3.7 Phytotoxicity

Phytotoxicity of pre-treated POME, photocatalytically treated POME and distilled water were justified using *Vigna radiata* (Mung bean seeds). Mung bean seeds were sterilized and rinsed in 0.5 % sodium hypochlorite for 30 min. Simultaneously, cotton wools were placed at the bottom of petri dish. After that, 9 mung bean seeds placed on the cotton wools. Each of 12 h, the cotton wools in different petri dishes were irrigated by 3 mL of pre-treated POME, photocatalytically treated POME and distilled water (3 mL), respectively. After a week, the radicle length of the mung bean seeds was measured and the phototoxicity was calculated using the following equation: (Chin et al., 2022).

$$\text{Phytotoxicity (\%)} = ((R_C - R_S) / R_C) \times 100\% \quad (3.3)$$

Where R_C is the radicle length of control (cm) and R_S is the radicle length of samples.

3.8 Photocatalytic Antibacterial Experiment

All required apparatus and materials were sterilized at 121°C for 20 min with *Hirayama HV-110* sterilizer autoclave within the antibacterial assays. The test was performed in BIOBASE *BSC-3FA2-HA* biosafety cabinet under a sterile environment. The antibacterial activities of as-fabricated samples were studied by suppressing two bacterial species namely *B. cereus* and *E. coli*. The bacteria were cultured in 100 mL broth solution at 37 °C with consistent shaking for 24 h in orbital shaker and a *BD 53* microbiological incubator at 37°C. The culture was then centrifuged at 4000 rpm to remove the supernatant. The bacterial cells were rinsed few times with sterile phosphate-buffered saline solution and diluted to 10⁷ CFU/mL using saline water. Consequently, the bacterial solution was dispersed evenly on nutrientagar plates. An antimicrobial susceptibility test disc coated with photocatalyst positioned at the middle of nutrient agar plate. The diameter of the zone of inhibition (ZOI) was finally measured in millimetres after the agar plate was incubated in *BD 53* microbiological incubator at 37 °C for 24 hr.

CHAPTER 4

RESULT AND DISCUSSION

In this chapter, experimental data and results in this research will be explained. It starts off with the characteristic investigation of pure BaFe₂O₄, pure BiOCl and BaFe₂O₄/BiOCl composites that produced via a precipitation-hydrothermal method. Followed by the photocatalytic decomposition of pre-treated POME employing the optimized BaFe₂O₄/BiOCl under visible light and sunlight irradiation. Next, several key operational parameters for instances photocatalyst loading, solution pH and initial pre-treated POME concentration were researched for evaluation of photocatalytic decomposition efficiency of developed photocatalysts. In this section, the reusability study of best photocatalyst at optimum conditions was also carried out. Besides, the assessment of H₂O₂ addition in the photocatalytic decomposition system was performed. The kinetic study was conducted on the photocatalytic reaction based on Langmuir-Hinshelwood (L-H) kinetic model to justify the rate of photocatalytic reaction. In the next section, the electrical energy consumption in the photocatalytic pre-treated POME treatment was measured using the developed 5 wt% BaFe₂O₄/BiOCl composite. The phytotoxicity of the photocatalytically treated pre-treated POME was examined by investigating its effect on germination of *Vigna radiata*. The antibacterial efficiencies of pure BaFe₂O₄, pure BiOCl and BaFe₂O₄/BiOCl towards *E. coli* and *B. cereus* were investigated via zone of inhibition.

4.1. Characterization Studies of Developed Photocatalysis

4.1.1. XRD Characterization

The crystal phase of pure BiOCl, BaFe₂O₄ and 5 wt% BaFe₂O₄/BiOCl were characterized by XRD analysis as shown in Figure 4.1. The diffraction peaks of pure BiOCl were well indexed to the tetragonal structure (JCPDS: 06-0249). The major diffraction peaks of BiOCl can be observed at the angle of $2\theta = 24.36^\circ, 26.07^\circ, 32.73^\circ, 33.68^\circ, 35.00^\circ, 36.78^\circ, 38.36^\circ, 40.96^\circ, 46.59^\circ, 48.72^\circ, 49.65^\circ, 54.32^\circ, 55.33^\circ$ and 58.83° which corresponded to (002), (101), (110), (102), (003), (112), (200), (113), (211) and (212) respectively (Ahuja et al., 2022). It can be investigated that the major diffraction peaks of the pure BaFeO₄ at the angle of $2\theta = 23.98^\circ, 24.38^\circ, 34.20^\circ, 34.60^\circ, 36.48^\circ, 45.00^\circ, 46.92^\circ, 58.84^\circ$ which corresponded to (111), (402), (130), (220), (221), (422), and (141) respectively. For pure BaFe₂O₄, its diffraction peaks assigned to orthorhombic structure (JCPDS: 46-0113) (Mandizadeh et al., 2017b). The characteristic peaks of both BiOCl and BaFe₂O₄ were existed in the composite, illustrating that the two-phase BaFe₂O₄/BiOCl was successfully fabricated. The strong and sharp diffraction peaks in the XRD analysis demonstrated that the as-synthesized catalysts were high crystallinity. This characteristic could improve the charge carrier separation and hence enhancing the photocatalytic performance (Hui et al., 2022; Xu et al., 2019). Additionally, less, or no other diffraction peaks representing on other impurities were found, designating high purity of as-fabricated catalysts. These data and results acquired in this research

were justified by other research works (Abdulrahman et al., 2020; Z. Zhu et al., 2021).

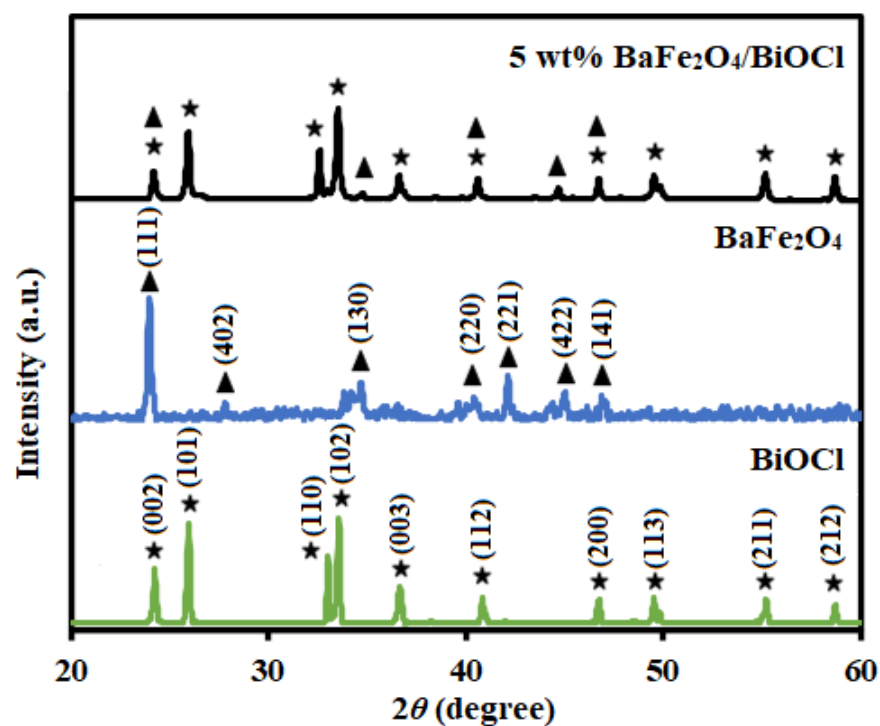


Figure 4.1: XRD patterns of BiOCl, BaFe₂O₄ and 5 wt% BiOCl/BaFe₂O₄ composite.

4.1.2. FTIR Examination

The construction of BaFe₂O₄/BiOCl composite was further justified by FTIR analysis, as displayed in Figure 4.2. The absorption bands at 1649 cm⁻¹ and 3414 cm⁻¹ were designated to the bending and stretching vibrations of O-H group, respectively (Jia et al., 2020). In addition, the characteristic peak appearing at 530 cm⁻¹ was assigned as Bi-O stretching vibration (Sin et al., 2020). The absorption bands in the range of 1300-1500 cm⁻¹ were corresponded to the Ba-O-Ba and Fe-O-Fe vibrations, whereas the peaks at 692 cm⁻¹ and 847cm⁻¹ were vibrations of metal–oxygen bonds in BaFe₂O₄ (Kenfoud,

Nasrallah, Baaloudj, Belabed, et al., 2022c; Zia & Riaz, 2020). The absorption band intensity of 5 wt% BaFe₂O₄/BiOCl was stronger than that of BaFe₂O₄, which can indicate the creation of a composite between BaFe₂O₄ and BiOCl (Yan & Yang, 2011). Furthermore, the peaks ascribed to the functional groups of BiOCl and BaFe₂O₄ were evidently observed in the FTIR spectrum of 5 wt% BaFe₂O₄/BiOCl, thereby further confirming the effective decoration of BaFe₂O₄ on BiOCl. Additionally, less, or no other diffraction peaks demonstrating on other impurities were observed, designating high purity of as-synthesized catalysts.

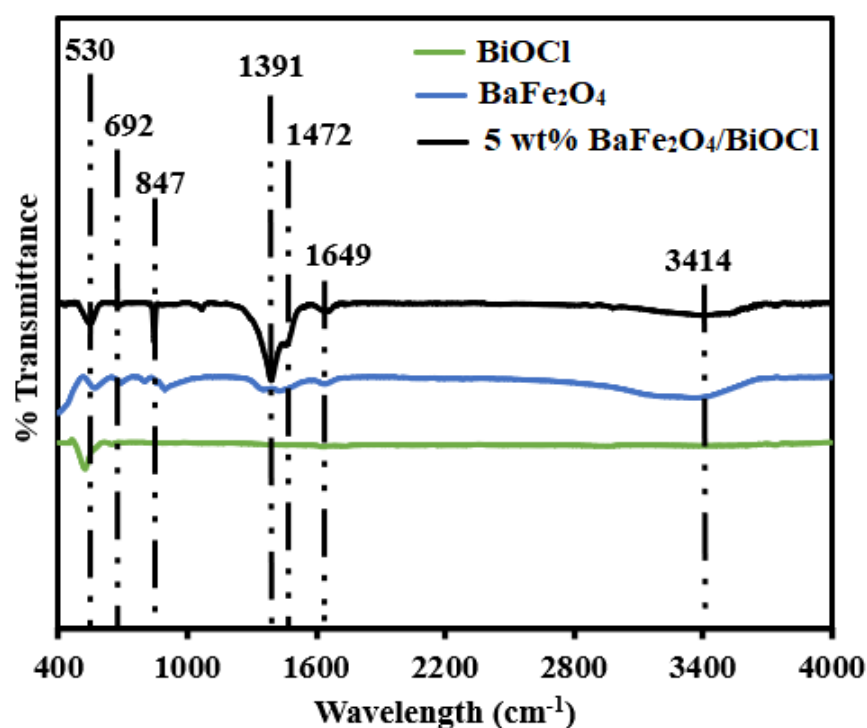


Figure 4.2: FTIR spectra of BiOCl, BaFe₂O₄ and 5 wt% BiOCl/BaFe₂O₄ composite.

4.1.3. FESEM, TEM and EDX Analyses

As depicted in Figure 4.3(a-c), the morphology of as-fabricated photocatalyst was studied by FESEM analysis. BaFe_2O_4 was a typical aggregated-structure particle, and BiOCl was a typical sheet structure. In the case of 5 wt% $\text{BaFe}_2\text{O}_4/\text{BiOCl}$, we can observe that the aggregated BaFe_2O_4 particles were vastly covered the surface of BiOCl , constructing a firmly contacted heterostructure. The TEM observation of 5 wt% $\text{BaFe}_2\text{O}_4/\text{BiOCl}$ was further carried out to evaluate the morphology and microstructure of the composite. Figure 4.3(d) displays that the surface of BiOCl nanosheets was embellished with aggregated BaFe_2O_4 particles, which was in good agreement with the FESEM study. Specifically, from the high-resolution TEM image in Figure 4.3(e), intimate interaction between the BiOCl and BaFe_2O_4 was established during the hydrothermal reaction. The lattice fringe with a spacing of 0.275 nm was ascribed to the (110) plane of BiOCl , whereas the lattice fringe with a spacing of 0.334 nm was classified as (221) plane of BaFe_2O_4 (F. Dong et al., 2014; J. Zhang et al., 2020). Moreover, the elemental mapping of 5 wt% $\text{BaFe}_2\text{O}_4/\text{BiOCl}$ composite was investigated by EDX test. As noticed in Figure 4.3(f), the composite was composed of Ba, Fe, O, Bi and Cl elements. The corresponding elemental mapping images also indicated that the detected elements homogeneously disseminated throughout the composite. Thus, these outcomes further provided legitimate validation of the coexistence of BaFe_2O_4 and BiOCl in the composite.

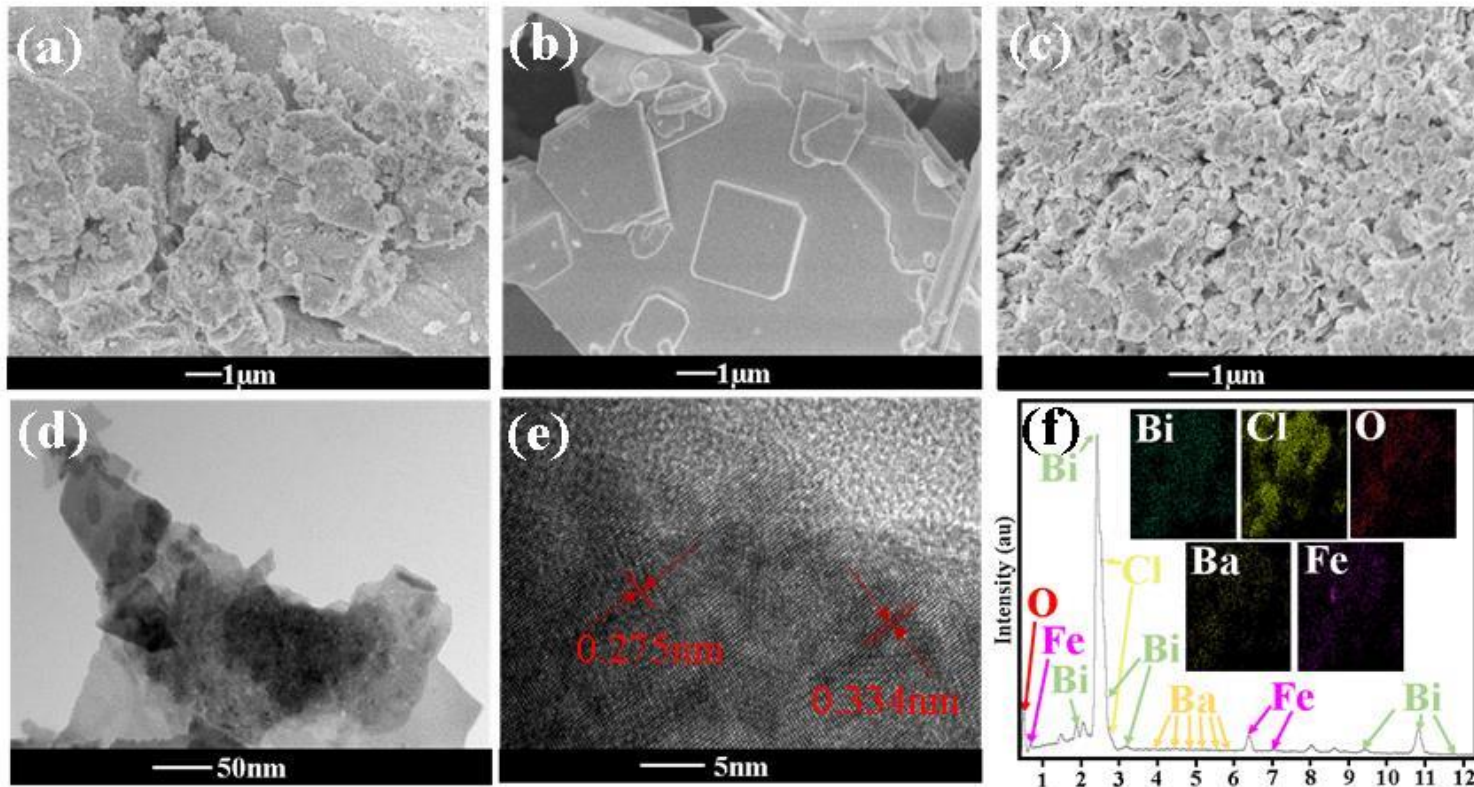


Figure 4.3: FESEM images of (a) BaFe₂O₄, (b) BiOCl and (c) 5 wt% BiOCl/BaFe₂O₄ composite. (d) TEM image, (e) HRTEM image and (f) EDX spectrum of 5 wt% BiOCl/BaFe₂O₄ composite. Inset of (f) is the EDX mapping images of 5 wt% BiOCl/BaFe₂O₄ composite

4.1.4. XPS Investigation

The surface of 5 wt% BaFe₂O₄/BiOCl was characterized by XPS method in order to detect the element chemical states within the composite. As demonstrated in Figure 4.4(a), the main peaks at 158.0 eV and 164.1 eV were correlated to Bi 4f_{7/2} and Bi 4f_{5/2}, respectively, which implied that the Bi existed as Bi³⁺ (Chin et al., 2022). Figure 4.4(b) reveals the Cl 2p spectrum of the composite, in which the binding energies at 197.4 eV and 199.2 eV were contributed by Cl 2p_{3/2} and Cl 2p_{1/2} of Cl⁻ respectively (Yan et al., 2020). In Figure 4.4(c), the peak positioned at 530.2 eV was assigned to O²⁻ in BiOCl (Gu et al., 2019). Ba 3d spectrum of as-fabricated composite is displayed in Figure 4.4(d), and the two peaks at 779.8 eV and 795.3 eV designated to Ba 3d_{5/2} and Ba 3d_{3/2}, respectively, exposing the coexistence of Ba²⁺ in composite (Liang et al., 2021). Figure 4.4(e) demonstrates two distinct peaks at 711.1 eV and 722.3 eV, which were corresponded to Fe 2p_{3/2} and Fe 2p_{1/2}, respectively, suggesting that Fe was presented in the form of Fe³⁺ (Kumar, Chandel, et al., 2021). Therefore, the XPS results further justified the co-occurrence of BiOCl and BaFe₂O₄ in the composite, agreeing well with the XRD, FTIR and EDX findings.

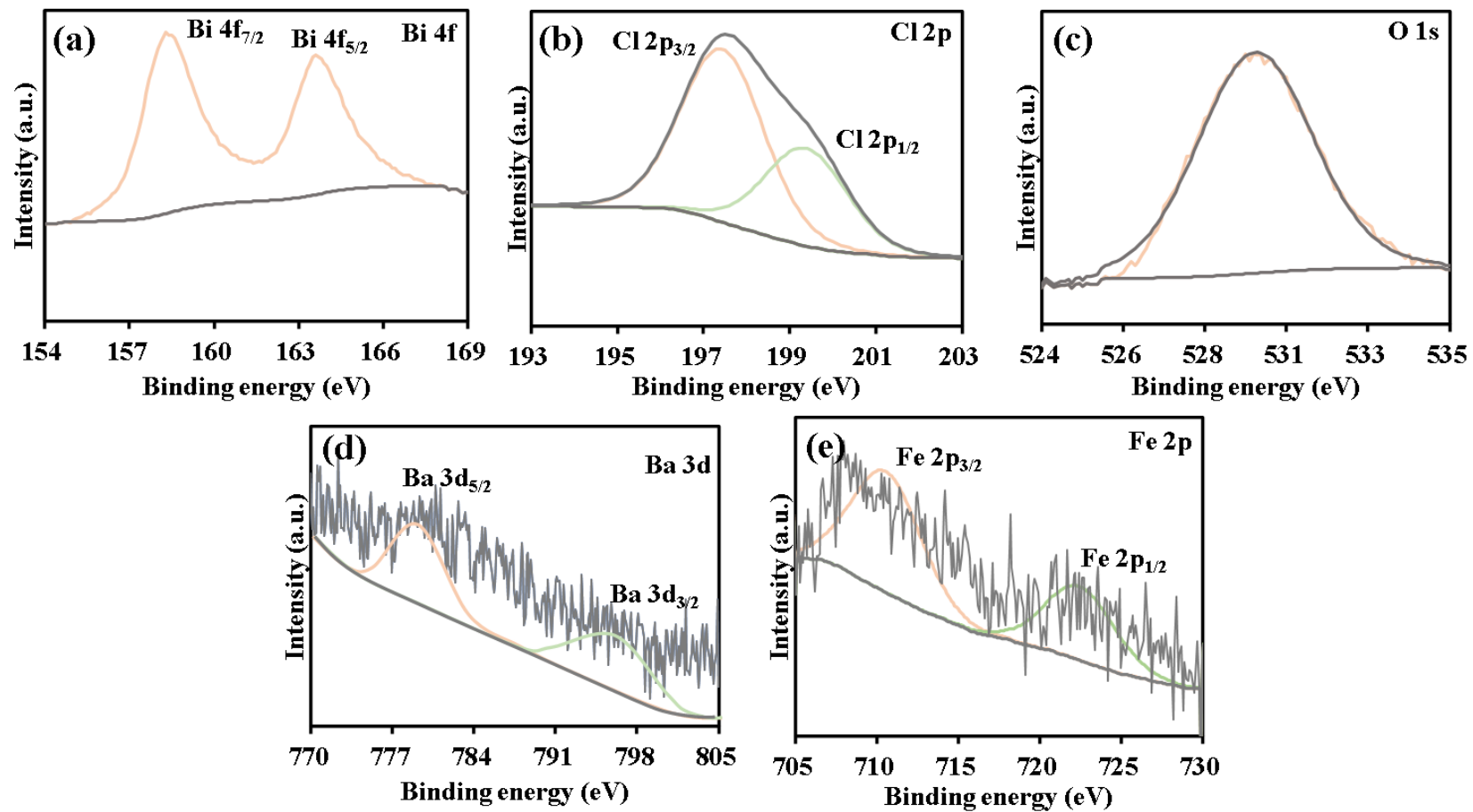


Figure 4.4: XPS spectra of (a) Bi 4f, (b) Cl 2p, (c) O 1s, (d) Ba 3d and (e) Fe 2p in 5 wt% BaFe₂O₄/BiOCl.

4.1.5. VSM ANALYSIS

The magnetic hysteresis loop of 5 wt% BaFe₂O₄/BiOCl is shown in Figure 4.5. The composite demonstrated a symmetrical S-shaped of magnetization curve, revealing the ferromagnetic behavior of the sample. The adequate saturated magnetization of 5 wt% BaFe₂O₄/BiOCl was beneficial to its easy separation from solution using an external magnet, which can be reused again in photodegradation process.

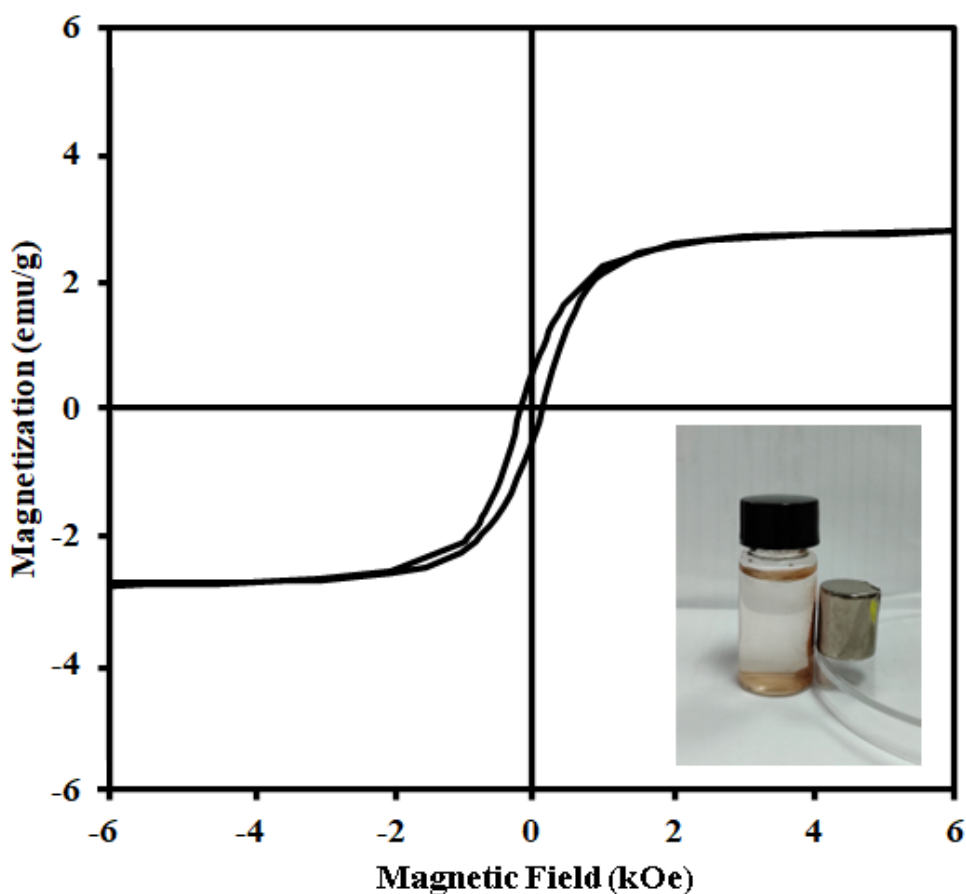


Figure 4.5: Magnetization curves of 5 wt% BaFe₂O₄/BiOCl composite. Inset is the image for the separation of the composite using a magnet.

By referring to Dilip and Jayaprakash, (2021), they demonstrated the magnetic property of BaFe₂O₄ nanorods which examined by vibrating sample magnetometer at room temperature. The hysteresis loop of BaFe₂O₄ powder displayed a ferromagnetic behaviour with a magnetization of 30.15 emu/g. Lin et al. (2021) evaluated the magnetic property of BiOCl and CoFe₂O₄/BiOCl, as expected BiOCl displayed no magnetic responsiveness while the CoFe₂O₄/BiOCl exhibited 2.5 emu/g of magnetization. Zia and Riaz (2020) displayed the magnetic property of BaFe₂O₄/PCz-PPy-60/40 (8.77 emu/g), which are having weaker magnetization as compared to pure BaFe₂O₄ (15.23 emu/g). They claimed that BaFe₂O₄ were responsible for the magnetic properties of BaFe₂O₄/PCz-PPy-60/40.

4.2. Photocatalytic Pre-Treated POME Treatment

4.2.1. Screening of As-Synthesized Photocatalysts Over Pre-Treated POME Decomposition.

The photocatalytic activities of BaFe₂O₄, BiOCl and x wt% BaFe₂O₄/BiOCl (x = 1, 5, and 10) were evaluated by pre-treated POME treatment under visible light irradiation. All experiments were conducted under similar conditions: photocatalyst loading = 0.5 g/L, [pre-treated POME] = 50 ppm, and solution pH = 7.0.

As shown in Figure 4.6, the blank test revealed that pre-treated POME was barely photolyzed under visible light irradiation. Furthermore, minor decline in the POME concentration was observed over 5 wt% BaFe₂O₄/BiOCl in the dark. Nevertheless, the concentration of pre-treated POME gradually decreased with elevating the irradiation time for all the investigated photocatalysts. This result can be correlated to the charge carrier generation and existence of redox reactions due to the sensitization of photocatalyst (Aditya et al., 2022; J. Zhang et al., 2018). The photocatalytic data demonstrated that the 5 wt% BaFe₂O₄/BiOCl possessed a greater degradation efficiency as compared to those of pure components (BiOCl and BaFe₂O₄) and other composites. It can be inferred that a suitable ratio of BaFe₂O₄/BiOCl was required for improving the photoactivity of the composite. This was because loading less BaFe₂O₄ amount resulted to less heterojunctions, while overloaded BaFe₂O₄ adversely worked as charge recombination center (Chen et al., 2021; Cui et al., 2020; Khan et al., 2020), which depressing the photodegradation efficiency. To further assess the photoactivity of 5 wt% BaFe₂O₄/BiOCl composite, additional experiment was performed over the physical mixture of BiOCl and 5 wt% BaFe₂O₄ (namely BiOCl + 5 wt% BaFe₂O₄). It was seemingly found that the photocatalytic performance of BiOCl + 5 wt% BaFe₂O₄ mixture was noticeably weaker compared to 5 wt% BaFe₂O₄/BiOCl, which only degraded 19% pre-treated POME within 210 min. This shows that simple BiOCl + 5wt% BaFe₂O₄ mixing not forming heterojunction with each other. By comparison, the degradation efficiency of 5 wt% BaFe₂O₄/BiOCl composite reached 61% at the same duration. This revealed the heterojunction created between BiOCl and

BaFe₂O₄ was an effective approach to improve the photodegradation performance.

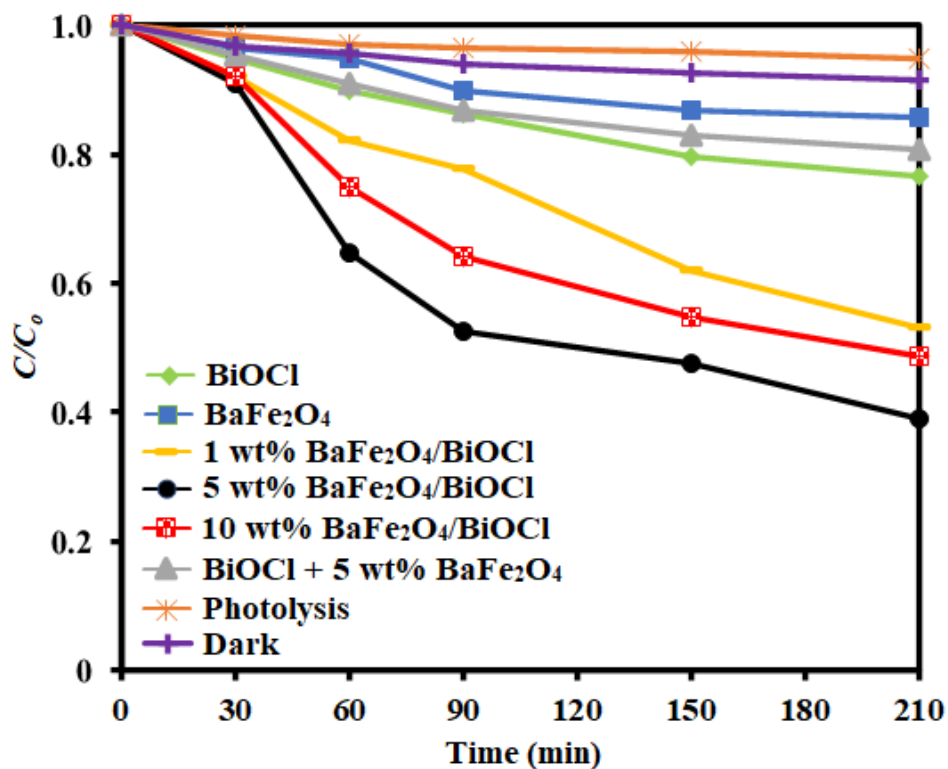


Figure 4.6: Photocatalytic pre-treated POME treatment over different photocatalysts ([pre-treated POME] = 50 mg/L; photocatalyst loading = 0.5 g/L; solution pH = 7).

4.2.2. Effect of Photocatalyst Loading

The impact of photocatalyst loading on photocatalytic decomposition of pre-treated POME was studied through experiments where different 5 wt% BaFe₂O₄/BiOCl loadings were applied, ranging from 0.25 g/L to 1.00 g/L, under visible light irradiation. All experiments were conducted with: [pre-treated POME] = 50 ppm and solution pH = 7.0.

Figure 4.7 presents the photocatalytic pre-treated POME treatment efficiency in the presence of varying loadings of 5 wt BaFe₂O₄/BiOCl composites. The results demonstrated an increase in photodecomposition efficiency from 40% at 0.25 g/L to 61% at 0.5 g/L, however, a decline was observed when the photocatalyst loading exceeded 0.5 g/L, resulting in decomposition efficiencies of 52% and 41% for 0.75g/L and 1.00 g/L, respectively.

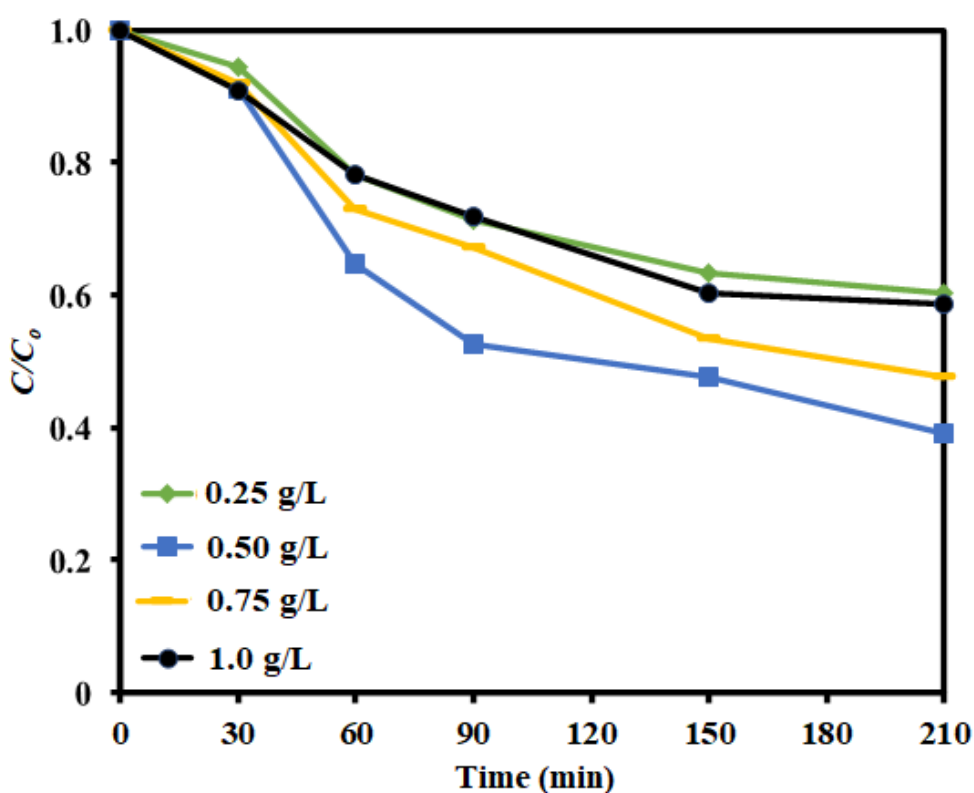


Figure 4.7: Effects of 5 wt% BiOCl/BaFe₂O₄ loading ([pre-treated POME] = 50 mg/L; solution pH = 7) on pre-treated POME treatment.

With the increase in the photocatalyst loading, the degradation efficiency of the composite demonstrated a trend of elevating initially from 0.25 to 0.5 g/L. The increase of photocatalyst loading was advantageous to deliver more charge carrier for oxidation-reduction reactions to proliferate the reactive

species (Prabhu et al., 2019; R. Xie et al., 2020). However, when the 5 wt% BaFe₂O₄/BiOCl loading further increased to 0.75 and 1.0 g/L, the pre-treated POME degradation depressed which can be due to the fact that overloading of photocatalyst can lead to poor light transmission and particle aggregation (Adhikari et al., 2019).

Li et al. (2019) fabricated Z-scheme BiOI/g-C₃N₄ heterojunction composite with improved photocatalytic performance and stability under visible light to reduce methyl orange (MO) dye. They varied the as-synthesized 15 wt% BiOI/g-C₃N₄ photocatalyst loading from 0.25 g/L to 1.5 g/L. Noticeably, 1.25 g/L was an optimum photocatalyst loading in MO degradation. They claimed that the slight reduction in photodegradation effect of MO was due to the increment of the loading of suspended photocatalyst which can increase the turbidity of the MO solution. This resulted in the worst absorption of visible light by the catalyst at the bottom of the solution thus suppressed the photodegradation efficiency of the MO.

Sin et al. (2020) reported the fabrication of the visible light-driven Nd-doped BiOBr nanosheets for photocatalytic POME treatment. In their experiment, the optimum loading of photocatalyst was 1.5 g/L with a 99.5% of photodegradation efficiency. They claimed that higher amount of photocatalyst will provide extra accessible active sites for photocatalytic activity. Nevertheless, the photodegradation efficiency generally worsen in excessive loading of photocatalyst loading which due to the agglomeration of the photocatalyst and optical opacity.

Kundu et al. (2021) published an article describing a facile synthesis of g-C₃N₄@BiOCl in adsorption-photocatalytic degradation of MB. They discovered that the increasing g-C₃N₄@BiOCl loading from 0.1-0.4 g/L improved the MB degradation efficiency. They mentioned that there were more active sites for adsorption and photocatalysis at higher loading content of the catalyst. The improvement effect was limited as the amount of photocatalyst further increased up to 0.4 g/L. It was influenced by the scattering of light and some saturation occurred due to a rise in the opacity of the solution.

4.2.3. Effect of solution pH

The effect of solution pH on photocatalytic decomposition of pre-treated POME was studied through experiments where different pre-treated POME pH were applied, ranging from pH 2-9, under visible light irradiation. All experiments were conducted with: photocatalyst loading = 0.5 g/L and [pre-treated POME] = 50 ppm. Figure 4.8(a) demonstrates the photocatalytic decomposition of pre-treated POME treatment efficiency under different pH of pre-treated POME. It was noticeable that the photodecomposition of pre-treated POME efficiency achieved 85% at optimum pH of 2. However, a decrease was observed when solution pH at 4, 7 and 9, resulting in decomposition efficiencies of 63%, 61% and 50% respectively.

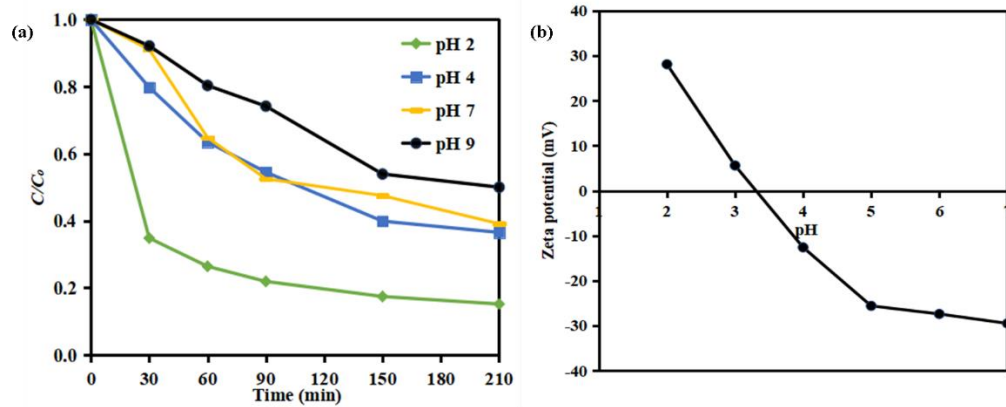


Figure 4.8: (a) Effects of solution pH with 5 wt% BiOCl/BaFe₂O₄ ([pre-treated POME] = 50 mg/L; photocatalyst loading = 0.5 g/L) on the pre-treated POME treatment; (b) Zeta potential measurement plot for 5 wt% BaFe₂O₄/BiOCl.

Based on the finding from Abdulsalam et al. (2020) they claimed that the pre-treated POME was negatively charge at low pH value. While as displayed in Figure 4.8(b), the pzc of 5 wt% BaFe₂O₄/BiOCl was determined as 3.3. The pzc value of photocatalyst below 3.3 indicates photocatalyst will be positively charged at <pH 3.3 and negatively charged at >pH 3.3. Therefore, under pH 2 both photocatalyst and pre-treated POME components interacted well led to better photodecomposition of pre-treated POME. In addition, across all range of pH regulated by the NaOH, higher pH intensified the competitive adsorption of ions from NaOH with pre-treated POME for the active site of photocatalyst thus reduced the photodecomposition performance. With the pzc of photocatalyst 3.3, the 5 wt% BaFe₂O₄/BiOCl was negatively charged it should be notified that there was an attraction force between photocatalyst and Na⁺ ions, the Na⁺ ion was poisonous to the active sites of the photocatalyst which led to the declined of photocatalytic decomposition of pre-treated POME (Li et al., 2021).

Aghdam et al. (2017) reported that the BiOI-BiOCl/C₃N₄ achieved the highest acid orange 7 degradation efficiency at pH = 3 and gradually reduced with the increase of solution pH. The plausible reason led to this difference was that acid orange 7 adsorption performance was relied on the catalyst surface charge. The measured pzc of BiOI-BiOCl/C₃N₄ was 6.0. They claimed that a strong adsorption of the dye on BiOI-BiOCl/C₃N₄ was due to the strong electrostatic attraction of the positively charged BiOI-BiOCl/C₃N₄ with anionic dye at pH =3. Besides, the positively charged BiOI-BiOCl/C₃N₄ surface in acidic solution aided in both adsorption of anionic dye and movement of photo-induced electrons to the surface of the photocatalyst.

Sin et al. (2020) demonstrated that the degradation of 2,4-D over BiOBr/MnFe₂O₄-10 nanocomposite and achieved 96.5% at optimum pH 4.7 after 80 min by adjusting pH from 2 to 9. However, at elevated pH levels, both negatively charged 2,4-D and nanocomposite experienced electrostatic repulsion that caused the decreases in photocatalytic performance. The pH level of 2,4-D was adjusted using NaOH to obtain pH 7 and 9. This alteration might have caused competition between the ions from NaOH and 2,4-D for the active-sites on the nanocomposite, leading to decelerate the photocatalytic activity.

4.2.4. Effect of Initial Pre-treated POME Concentration

Another operating parameter that can influence the photocatalytic activity was pollutant concentration thus effect of initial pre-treated POME

concentration was investigated. Different initial pre-treated POME concentrations of 50-125 ppm were employed in the photocatalytic treatment under visible light irradiation. All experiments were conducted under similar conditions: 5 wt% BaFe₂O₄/BiOCl loading = 0.5 g/L and solution pH = 2. Figure 4.9 shows the findings of the photocatalytic pre-treated POME treatment under different initial pre-treated POME concentrations. The decomposition efficiency of pre-treated POME with 50 ppm as initial concentration reached 85% when the pre-treated POME concentration raised to 75 ppm, the decomposition efficiency reduced to 78%. As the initial pre-treated POME concentration further raised to 100 ppm and 125 ppm, the photocatalytic activities of 5 wt% BaFe₂O₄/BiOCl were 75% and 72% respectively.

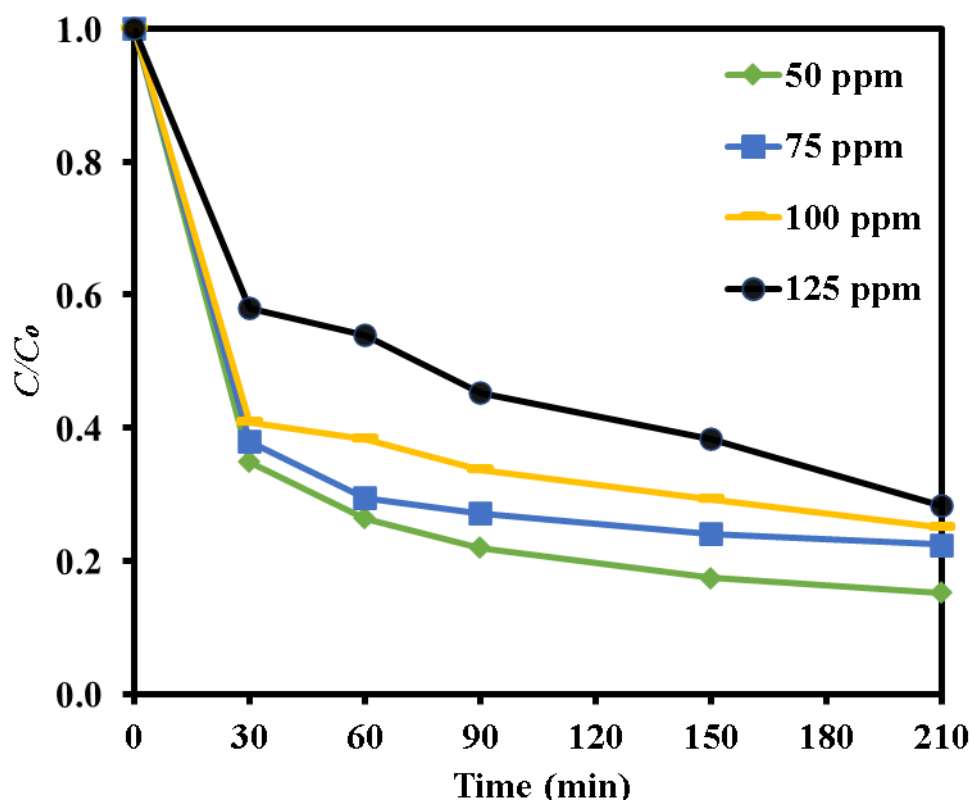


Figure 4.9: Photocatalytic decomposition performance of different initial pre-treated POME concentration (ppm) under (photocatalyst loading = 0.5 g/L; solution pH = 2) on the pre-treated POME treatment.

These results can be attributed to the higher chances of collision between organics and photocatalyst at low concentrations, whereas at higher pre-treated POME content, excessive amounts of pollutants can be adsorbed on the photocatalyst surface, reducing the number of effective active sites for decomposition. Additionally, high levels of pre-treated POME, which is a heavily coloured effluent, can contribute to the turbidity of the solution and hindered light penetration, affecting the activation of photocatalysts.

Maleki et al. (2020) demonstrated the photoactivity of 2% WO₃ doped ZnO in degradation of diazinon. They revealed that the increasing diazinon concentration from 10 to 200 ppm declined the diazinon efficiency from 88.6% to 44.4%. They explained that higher concentrations of diazinon led to more active sites to be covered thus decreased the generation of active species and reduced the rate of decomposition.

Zangeneh et al. (2019) reported the initial concentration pre-treated POME was adjusted from 300 ppm to 700 ppm which declined from 93% to 72% of photocatalytic decomposition. They claimed that at high concentration of POME, the active sites of the photocatalyst were saturated and poisoning occurred by the excess organic molecules and intermediates thereby causing an inhibitive effect on light penetration, •OH and O₂•⁻ formation for photodegradation reaction. The conceivable effect of longer irradiation time on the photodegradation process was observed which favors more effective contacts between the •OH radicals and the organic compounds, causing higher degradation efficiency.

4.3. Photocatalyst Recyclability And Phytotoxicity Studies

The longevity and repeatability of the photocatalyst played a vital role in retaining its practical value for large-scale wastewater applications. To evaluate the stability of the photocatalyst, the 5 wt% BaFe₂O₄/BiOCl material was repeatedly utilized over four cycles while undergoing the photodegradation of pre-treated POME treatment under constant operating conditions: a photocatalyst loading = 0.5 g/L, an initial pre-treated POME concentration = 50 ppm, and solution pH = 2. After each cycle, the photocatalyst was filtered, cleaned with distilled water, and dried before being reuse for the next round of photodecomposition.

As presented in Figure 4.10(a), the photoactivity only slightly reduced (from 85% to 78%), and the minimal decline can be attributed to the inescapable loss of composite during the recovery process. Farhan Hanafi and Sapawe (2019) also claimed that photocatalyst recycling was a pivoted issue for the long run utilization. Their results showed that the degradation efficiency reduced with only 6% from 96% to 90%. Therefore, its convenient magnetic separation and good stability during recycling runs, which are of great importance for practical applications.

To assess the phytotoxicity of treated pre-treated POME, *vigna radiata* germination was carried out (Figure 4.10 (b) and Figure A1) and the findings demonstrated that after 5 wt% BaFe₂O₄/BiOCl photocatalysis, the phytotoxicity levels of pre-treated POME solution significantly diminished, which revealed

the effectiveness of reducing the toxicity of treated effluent over the prepared composite. Similar findings also reported by Phang et al., 2021, they performed the phytotoxicity test of the photocatalytically treated POME over CuO NPs and stated that the radicle length in green mung bean (*vigna radiata*) as the indication of reduction in phytotoxicity. Through their findings, the *vigna radiata* irrigated with photocatalytically treated POME and deionized water having the average radicle length of 16 cm and 16.5 cm respectively., while the *vigna radiata* irrigated with untreated POME having a shorter radicle length of 9.0 cm. In addition, the phytotoxicity profile of *vigna radiata* seeds germination applying before and after photocatalytic degradation of carbamazepine-contaminated solution was also reported (Mohan et al., 2021). Based on their findings, the radical length of *vigna radiata* irrigated with water, carbamazepine contaminated solution and treated carbamazepine solution were found to be 6.2, 2.5 and 3.6 cm respectively. They claimed that the shorter radicle length from the treated carbamazepine solution was due to the existing of trace amount of intermediates that was not completely decompose during photocatalysis.

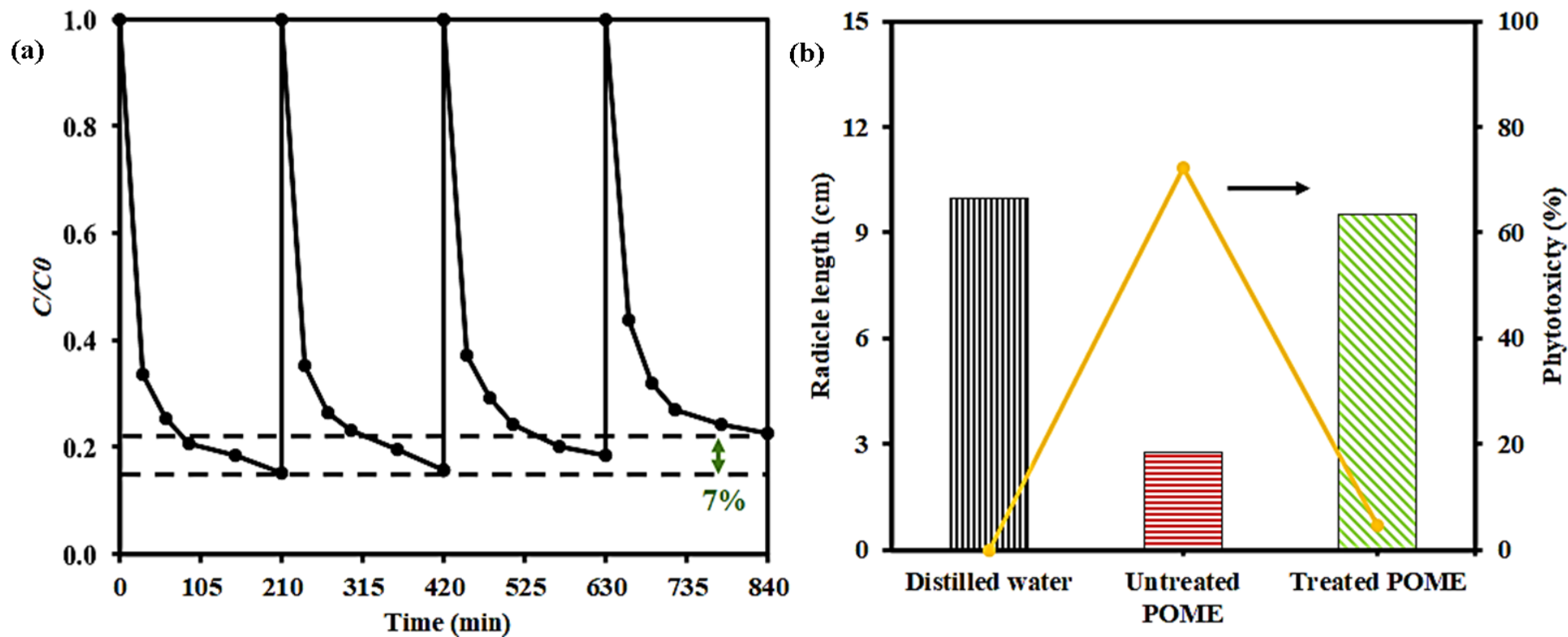


Figure 4.10: (a) Cyclic use of 5 wt% BaFe₂O₄/BiOCl for four successive runs under (photocatalyst loading = 0.5 g/L; solution pH = 2; [pre-treat POME] = 50 ppm) on the pre-treated POME treatment; (b) Phytotoxicity of pre-treated POME before and after the 5 wt% BaFe₂O₄/BiOCl photocatalysis.

4.4 The Role of H₂O₂ As Electron Acceptor in Photocatalytic POME Treatment.

To study the influence of H₂O₂ on the photocatalytic removal performance of pre-treated POME, the experiments were conducted by 5wt% BaFe₂O₄/BiOCl (0.5 g/L) under acidic pH conditions (pH 2.0) and pre-treated POME concentration (50 ppm) with varied concentration of H₂O₂ (0-4 mmol/L).

As displayed in Figure 4.11, the decomposition efficiency of pre-treated POME increased with the introduction of 2 mmol/L of H₂O₂ concentration and reached 91%, when the H₂O₂ concentration raised to 3 mmol/L, the decomposition efficiency increased to 99%. As H₂O₂ concentration further raised to 4 mmol/L, the photocatalytic activities of 5 wt% BaFe₂O₄/BiOCl reduced to 87%.

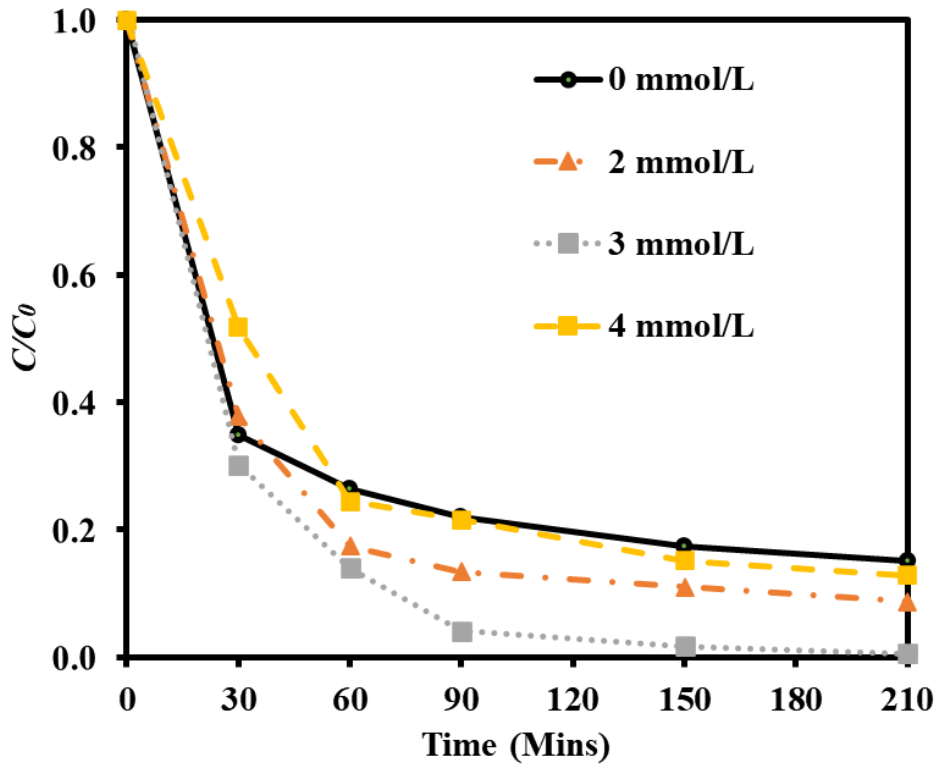


Figure 4.11: Photocatalytic decomposition of pre-treated POME at optimal conditions with different concentration of H₂O₂.

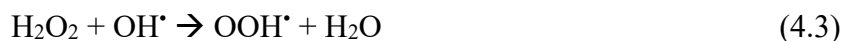
Asadzadeh-Khaneghah et al. (2019) and Cai et al. (2019) also reported the presence of the optimum concentration of H₂O₂ in their photocatalytic studies. In this study, the optimum H₂O₂ concentration was found to be 3 mmol/L, the reduction of decomposition efficiency at 4 mmol/L would be due to the overdose of H₂O₂ as •OH scavenger and produced a weaker, •OOH and H₂O as demonstrated by Equation 4.3. Besides, the •OOH potentially to scavenge •OH to form H₂O and O₂ that presented in Equation 4.4.



Additional •OH can be generated from the reaction of H₂O₂ with O₂•⁻ :



However, at high concentrations, H₂O₂ can act as a cleaver of •OH, according to the following reactions (Choi et al., 2022):



The findings were tallied with Arutanti et al. (2020) experimentally analysed the effect of H₂O₂ concentration on the lignin photodegradation. Their study demonstrated that the lignin decomposition enhanced from 19.4% to 47.7% as the concentration of H₂O₂ increased from 100 to 4000 mg/L. However, a further increase of concentration greater than 4000 mg/L led to a decline of photoactivity. Moreover, Khoiriah et al. (2020) and Mohammed et al. (2020) claimed that excess H₂O₂ can also scavenge valence band holes following either Equations (4.5 and 4.6). This mechanism led to the inhibition of the major pathway for the generation of •OH radicals.



Sayadi et al. (2021) reported the synthesis of Ag-CuFe₂O₄@WO₃ in photocatalytic degradation of Gemfibrozil (GEM) and Tamxifen (TAM). They noticed that the increasing H₂O₂ concentration enhanced the GEM and TAM efficiency from 0.1 to 0.5 mg/L. They claimed that the improved photodegradation performance can be recognized as the elevated oxygen content due to the decomposition of H₂O₂. However, H₂O₂ also acted as

scavenger of positive holes which led to the depreciation of photodegradation of GEM and TAM.

4.5 Kinetic Study

4.5.1 Determination of Kinetic Model

The photodecomposition rate can be affected by several factors including photocatalyst loading, solution pH, initial pre-treated POME concentration, and H₂O₂ concentration (Kamari et al., 2021). In this research, the effect of H₂O₂ assisted photocatalytic decomposition of pre-treated POME was investigated. The tests were conducted under 5wt% BaFe₂O₄/BiOCl (0.5 g/L) under acidic pH conditions (pH 2.0) and pre-treated POME concentration (50 ppm) and 3 mmol/L H₂O₂ concentration.

Kinetic study was performed to justify the reaction rate of photodecomposition of pre-treated POME using 5 wt% BaFe₂O₄/BiOCl. In heterogeneous photocatalytic reaction, rate law was employed to evaluate the rate of reaction which can be stated as displayed in Equation (4.7).

$$-r = \frac{dC_P}{dt} = k[\text{concentration of reactant}]^n \quad (4.7)$$

where k is the rate constant, C is the pollutant concentration and n is the order of reaction. The reaction order was relied on the data of n which was 0, 1, 2, or

3. Hence, determination on kinetic order of photodecomposition of pre-treated POME was conducted by replacing the acquired data into all ‘n’ order in the integrated equation in Figure 4.12. The orders of rate of reaction with respective rate law were displayed in Table 4.1.

Table 4.1: Reaction order with their relative rate law and integrated equation.

Order (n)	Reaction	Rate laws	Integrated Equations	Rate constant (K) units
0	Zero Order	$-r = KC_P^0$	$C_P = -C_P + kt$	mol/L•min
1	First Order	$-r = KC_P^1$	$\ln \frac{C_{P0}}{C_P} = kt$	L/min
2	Second Order	$-r = KC_P^2$	$\frac{1}{C_P} = \frac{1}{C_{P0}} + kt$	L/mol•min
3	Third Order	$-r = KC_P^3$	$\frac{1}{C_P^2} = \frac{1}{C_{P0}^2} + kt$	(L/mol) ² /min

Note: $-r$ = rate of reaction
 k = rate constant
 C_{po} = initial concentration of pre-treated POME (ppm)
 C_p = Concentration of pre-treated POME at reaction time t (ppm)
 t = reaction time (min)

The results of the test were used to generate graphs for Zero-order, First-order, Second-order, and Third-order integrated equations, which are presented in Figure 4.12 respectively.

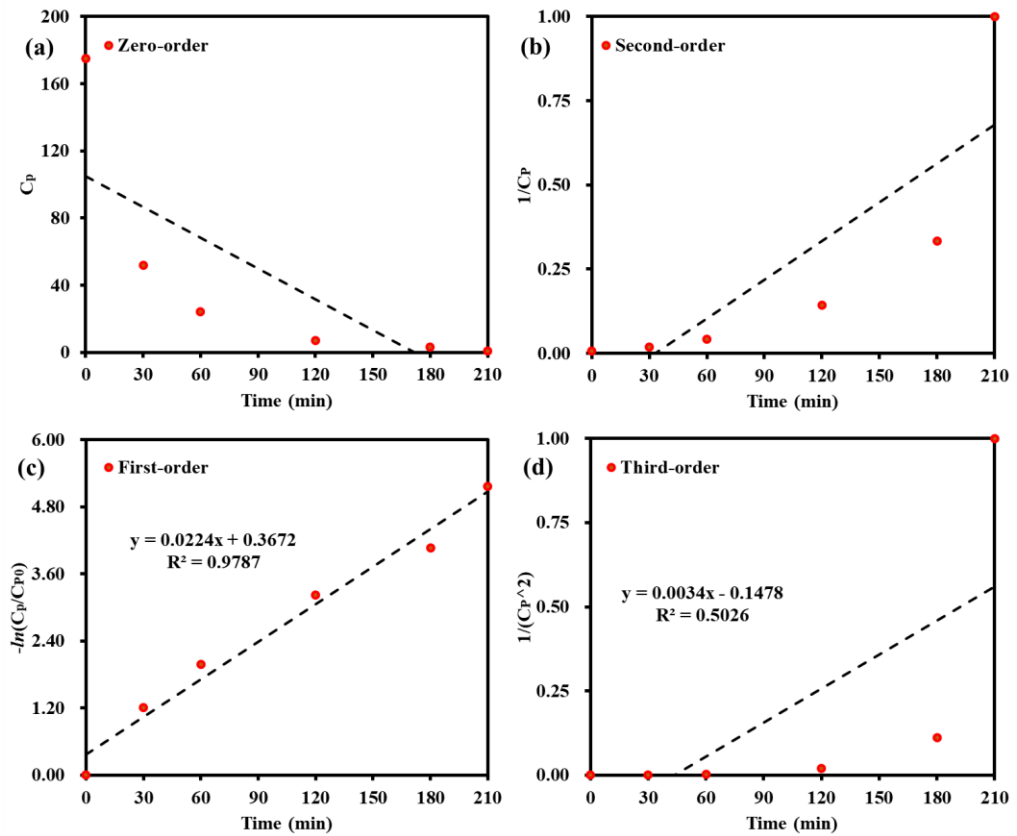


Figure 4.12: Plot of (a) zero order reaction, (b) first order reaction, (c) second order reaction, and (d) third order reaction. Conditions: BaFe₂O₄/BiOCl loading= 0.5 g/L; pre-treated POME concentration = 50 ppm, solution pH= 2.0 and H₂O₂ concentration= 3.0 mmol/L.

The slope of the best fitting line of corresponding graph represented the rate constant (k). Table 4.2 displays the rate constant (k) and their respective coefficient of determination (R^2) gained from the reaction order plotting graphs.

Table 4.2: The rate constant and their corresponding determination coefficient obtained from reaction order plotting graphs.

Order (n)	Reaction Order	R ²	Rate constant (k)
0	Zero Order	0.5857	-0.6105
1	First Order	0.9787	0.0224
2	Second Order	0.7084	0.0038
3	Third Order	0.5026	0.0034

The first order reaction displayed the largest value of rate constant (0.0224) and the highest determination coefficient (0.9787). Thus, the kinetics of the photocatalysis of pre-treated POME was concluded as first order reaction. Similar to this study, the kinetic for photodegradation of pre-treated POME has been developed and analysed using pseudo first order model (Kleiman et al., 2020; Salari & Zahiri, 2022; Subramanian et al., 2023).

4.5.2 Langmuir-Hinshelwood Model

The Langmuir-Hinshelwood (L-H) model was employed in this study to examine the kinetic for photodegradation of pre-treated POME using 5 wt% BaFe₂O₄/BiOCl. The L-H model assumes an irreversible reaction on a single active site, which affects the degradation rate and is dependent on catalyst loading. This model is widely adopted in the literature for photocatalysis studies and has a strong agreement with the data from this experiment. Furthermore,

many researchers have relied on the L-H model in investigating the kinetics of pre-treated POME photodegradation, making it a suitable choice for this study (Charles et al., 2019; Lim & Kay Lup, 2022). According to L-H model, the kinetic for photodegradation of pre-treated POME can be expressed as Equation 4.8.

$$\ln \frac{C_0}{C} = k_{app}t \quad (4.8)$$

where C is equal to C_0 when $t = 0$ (mg/L), and k_{app} is the apparent rate constant (L/mg)

In the photocatalytic system, when the pollutant concentration was considerably low ($K_{app} \ll 1$), the L-H expression could be streamlined to an apparent first-order equation as demonstrated in Equation (4.8) demonstrated in Section 4.5.1. In addition, the equation can be further described in terms of r as displayed in Equation (4.7) previously shown in section 4.5.1. (Neelgund & Oki, 2020; Tamaddon et al., 2020; Xiang et al., 2022). The experimental conditions were 0 to 4 mmol/L of H_2O_2 concentration, 0.5 g/L of photocatalyst loading, solution pH of 2 and 50 ppm of pre-treated POME concentration. Figure 4.13 displays the kinetic profile for photodecomposition of pre-treated POME with different H_2O_2 concentrations.

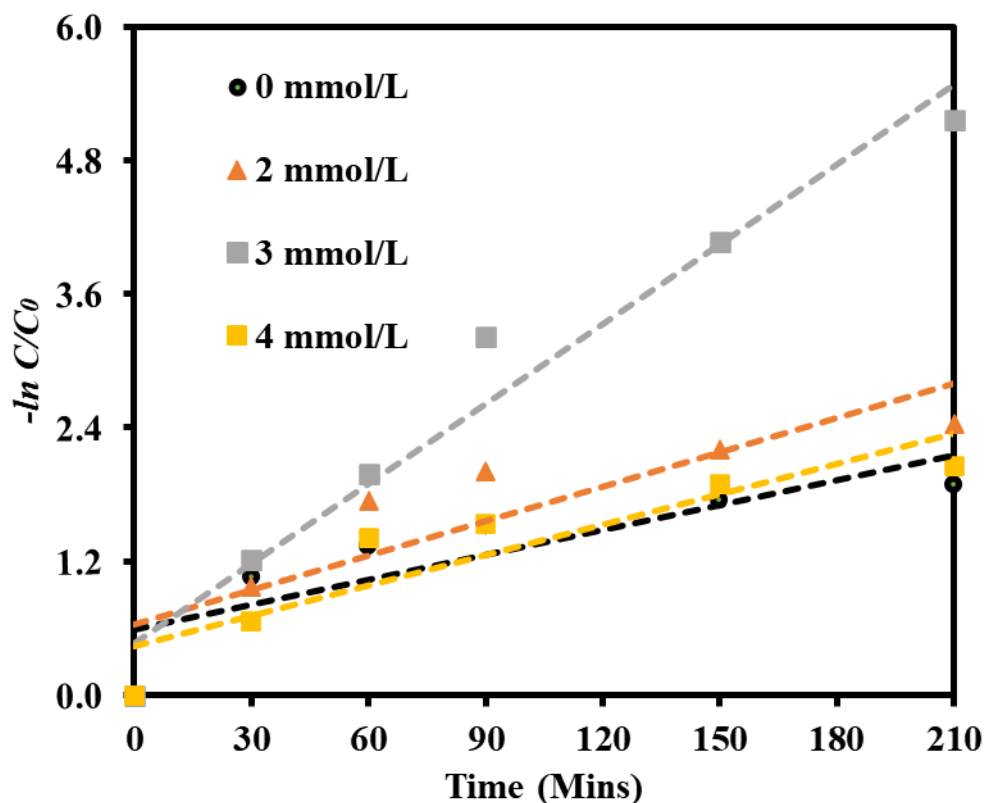


Figure 4.13: Kinetic profile for photodecomposition of pre-treated POME with different H₂O₂ concentration.

The slope of the plotting graph was the apparent first order constant (k_{app}). The obtained k_{app} with different H₂O₂ concentrations (0, 2, 3 and 4 mmol/L) were found to be 0.0074, 0.0091, 0.0222 and 0.0103 respectively. The obtained optimal k_{app} value was 0.0222 (3 mmol/L) was 3 folds, 2.43 folds and 2.15 folds correlated to 0, 2 and 4 mmol/L respectively. The value of apparent rate constant (k_{app}) increased when the H₂O₂ concentration increased from 0 to 3 mmol/L. However, the k_{app} declined when the H₂O₂ concentration beyond 3 mmol/L. This was due to high H₂O₂ concentration, excessive H₂O₂ will act as electron. Moreover, the order of k_{app} value was 3>4>2>0 mmol/L, which were tallied with the findings as discussed in the effect of H₂O₂ concentration.

4.6. Electrical Energy Consumption

The economic factor is one of the critical factors that assessing the viability of the photocatalytic process (Guaraldo et al., 2023; Vaiano et al., 2019). The electrical energy consumption and operational cost under the optimum conditions were evaluated based on the concept of electrical energy per order (E_{EO}) for the photodecomposition of pre-treated POME in this research study. The E_{EO} is precisely defined as the amount of electrical energy, measured in kilowatt-hours, required to reduce the organic waste in treating each cubic meter of organic waste (Mecha & Chollom, 2020; Mustafa & Oladipo, 2021). Under the optimum conditions, the E_{EO} (kW h/m³ order) of photocatalytic system using 5 wt% BaFe₂O₄/BiOCl and commercial BiOCl photocatalyst were calculated based on Equation (4.9) (Fattahi et al., 2021; H. Liu et al., 2022)

$$E_{EO} = \frac{38.4 \times P}{V \times k} \quad (4.9)$$

Where P is described, the power consumed by the LED lamp (kW), V is the volume of the solution in the reactor (L), k is pseudo first order rate constant for the POME photodecomposition (min⁻¹) respectively. Table 4.3 shows the E_{EO} (in kWh/m³) values for 5 wt% BaFe₂O₄/BiOCl and individual photocatalysts. It was investigated that the photocatalytic system using 5 wt% BaFe₂O₄/BiOCl was discovered to be about 17.08- and 27.75-times lower power consuming as compared to the that photocatalytic system using pure BiOCl and pure BaFe₂O₄, implying that the photocatalytic system using 5 wt% BaFe₂O₄/BiOCl was more

effective. The outcomes also furthered confirmed the pros of using 5 wt% BaFe₂O₄/BiOCl in photodecomposition of pre-treated POME. It was also to conduct E_{EO} measurement in the present research to the cost of electricity. Based on the Tenaga Nasional Berhad (2022), the cost of 1 kW h of electricity for the first 200 kW h (1~200 kWh) is RM 0.38 (Ringgit Malaysia). Then, for the next kWh (201 kWh onwards), the cost is RM 0.441. The estimated costs (RM/m³•order) were calculated based on Equation (4.10).

$$\text{Electrical cost} = E_{EO} \times S \quad (4.10)$$

Where S is the cost of electricity for 1 kWh (RM/kWh).

Table 4.3. Electrical energy consumption estimation using LED light as light source.

Photocatalyst	Rate constant (k)	E_{EO} (kWh/m ³ •order)	Cost (RM/m ³ •order)
5 wt% BaFe ₂ O ₄ /BiOCl	0.0222	54.054	23.83
BiOCl	0.0013	923.07	372.46
BaFe ₂ O ₄	0.0008	1500	609

Based on the outcomes, the cost required in photocatalytic system using 5 wt% BaFe₂O₄/BiOCl was lower than that of the photocatalytic system using individual photocatalysts. This indicated that the photocatalytic system employing 5 wt% BaFe₂O₄/BiOCl was economically viable, being able to attain higher decomposition of pre-treated POME with the cost of RM 23.83/m³•order. Generally, it can be simplified that the 5 wt% BaFe₂O₄/BiOCl photocatalytic system was a much energy and cost-efficient system for the decomposition of

pre-treated POME. Several results were published by other researchers in their findings. Nawaz et al., (2022) stated that W-TiO₂, CS B TiO₂, CS B-TiO₂+H₂O₂ obtained an electrical energy consumption 92.84, 48.31 and 36.86 (kWh/m³) respectively in order to treat phenol. Irfan et al., (2021) demonstrated that the optimized Mn-B-TiO₂(0.3%) achieved an electrical consumption per order with a value of 75.15 kWh/m³ in order to decompose phenol. In this research outcomes, the E_{EO} value for 5 wt% BaFe₂O₄/BiOCl displayed that the photocatalytic system was a practical electrical-cost-efficient method for the photodecomposition of pre-treated POME.

4.7 Photocatalytic Activity Under Sunlight Irradiation

To study the photocatalytic removal performance of pre-treated POME under sunlight irradiation, the experiments were conducted by 5wt% BaFe₂O₄/BiOCl (0.5 g/L) under acidic pH conditions (pH 2.0) and pre-treated POME concentration (50 ppm) with concentration of H₂O₂ (3 mmol/L).

Based on Figure 4.14, among the findings, the photolysis of POME with 3 mmol/L of H₂O₂ performed weakly with negligible POME decomposition. However, the POME decomposition with 5 wt% BaFe₂O₄/BiOCl and 3 mmol/L of H₂O₂ achieved the remarkable 100% of POME decomposition which was excelled as compared to pure BiOCl, pure BaFe₂O₄, 5 wt% BaFe₂O₄/BiOCl, H₂O₂ (3 mmol/L) and photolysis of pre-treated POME. Besides, the photolysis of pre-treated POME displayed insignificant decomposition performance under

sunlight irradiation. Interestingly, the performance of as-synthesized photocatalyst showed a boosted performance as compared to the findings under visible light irradiation. In addition, photocatalytic decomposition of pre-treated POME with 5 wt% BaFe₂O₄/BiOCl elevated to 95% without the addition of H₂O₂ concentration as compared to the 85% under visible light irradiation.

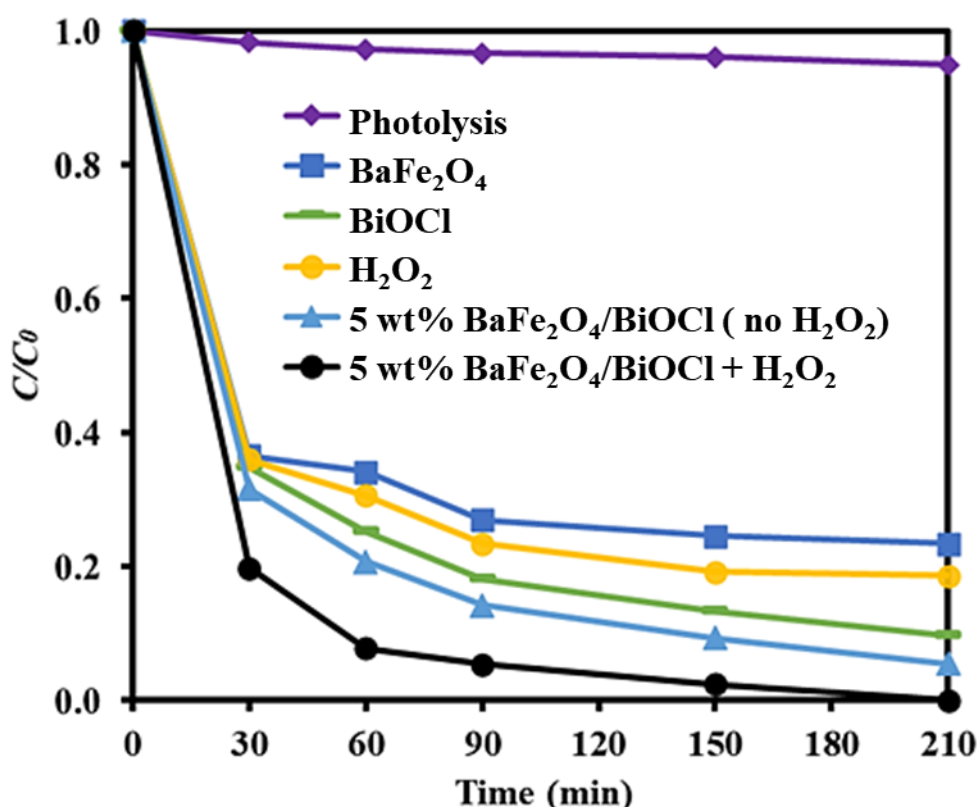


Figure 4.14: Photocatalytic decomposition of pre-treated POME under sunlight irradiation with conditions: (Photocatalyst loading = 0.5 g/L, solution pH = 2.0, pre-treated POME concentration = 50 ppm and H₂O₂ concentration = 3 mmol/L)

The overall improvement illustrated in decomposition of organic pollutant under sunlight irradiation was due to the intensity difference of light source (Alkaykh et al., 2020b). As mentioned in Section 3.2, the intensity of LED lamp emitted a 45,000 lx while the sunlight can easily have an average intensity of 90,000 lx throughout the experiment. Therefore, the light can

penetrate well in the solution to activate the photocatalyst which enhanced generation of ROS that responsible to POME decomposition.

Similar findings were reported by Rosu et al. (2017), they employed TiO₂-pt/GO in amaranth, sunset yellow and tartrazine degradation under UV light and natural sunlight irradiation. They found that the sunlight photocatalytic system was more efficient in amaranth (85% → 99%), sunset yellow (60% → 88%) and tartrazine (63% → 95%) photodegradation. In addition, Chankhanittha et al. (2021) synthesized the 5Ag-ZnO photocatalyst and utilized in photodegradation of reactive red 141 dye as well as ofloxacin antibiotics. Based on their findings, the photodegradation of both pollutants achieved complete degradation as compared to red 141 dye (51%) and ofloxacin antibiotics (17%) under visible light irradiation. Besides, Eskizeybek et al. (2012) also illustrated the degradation of methylene blue and malachite green under UV light and sunlight irradiation via PANI/ZnO. The degradation of methylene blue (79% → 97%) and malachite green (89% → 99%) generally improved under sunlight irradiation as compared to artificial UV light irradiation. They claimed that the PANI/ZnO could be activated to photo-generate more charge carrier under natural sunlight irradiation to enhance photocatalytic activity.

4.8 Photocatalytic Mechanism

4.8.1 UV-vis DRS and Mott-Schottky Analyses

UV-vis DRS spectra were used to investigate the optical traits of BiOCl, BaFe₂O₄ and 5 wt% BaFe₂O₄/BiOCl as shown in Figure 4.15(a). It can be noticed that pure BiOCl mainly absorbed in the UV region, whereas the BaFe₂O₄ possessed strong absorption in visible light region. The optical absorption of 5 wt% BaFe₂O₄/BiOCl had a slight redshift compared to pure BiOCl, validating the interaction between BiOCl and BaFe₂O₄ in the composite. Similar investigation has also reported Ma et al. (2016), they fabricated BiOCl/ZnFe₂O₄ samples and redshift of the absorption edge was observed for the heterojunction sample that was due to the interaction of both BiOCl and ZnFe₂O₄ at the interface. Besides, Bera et al. (2022) also demonstrated the decoration of CuFe₂O₄ on BiOCl, which able to boost the light absorption on UV and visible light region which was attributed by intimate connection between BiOCl and CuFe₂O₄. The band gap (E_g) can also be determined from Tauc plot of $(\alpha h\nu)^2$ versus photon energy ($h\nu$). By intercepting the tangent to x-axis as demonstrated in Figure 4.15(b-c), the E_g of BiOCl and BaFe₂O₄ were recorded as 3.59 eV and 2.27 eV, respectively. Moreover, Mott-Schottky curves were employed to investigate the band alignment of these semiconductors (Mao et al., 2021). From Figure 4.15(d), the conduction band positions (E_{CB}) of BiOCl and BaFe₂O₄ were revealed as -0.24 eV and -0.85 eV, respectively. In contrast, their valence band positions (E_{VB}) can be determined by $E_{VB} = E_{CB} + E_g$ (Chen

et al., 2022; Kafian & Sadeghzadeh-Attar, 2022). Hence, the E_{VB} of BiOCl and BaFe₂O₄ were 3.35 eV and 1.42 eV, respectively. Above outcomes indicated that the staggered band alignment in BaFe₂O₄/BiOCl fulfilled the necessity in developing the Z-scheme heterojunction, which improved the charge carrier separation and concurrently retained great redox capabilities.

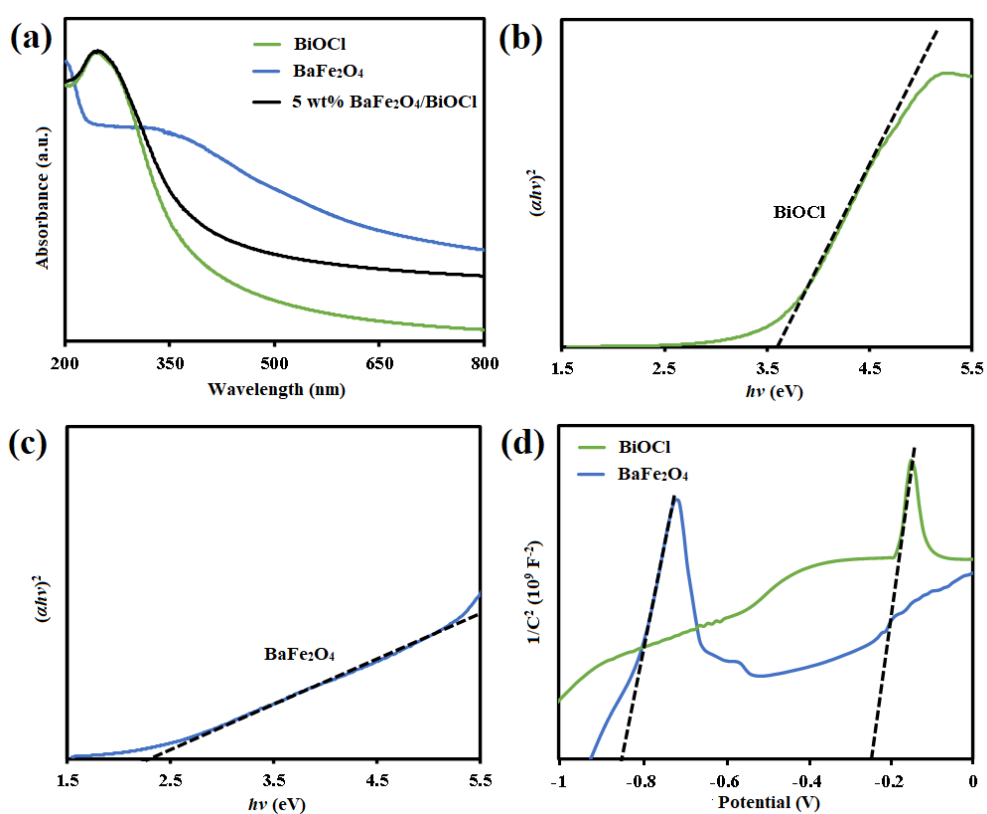


Figure 4.15: (a) UV-vis DRS spectra of BiOCl, BaFe₂O₄ and 5 wt% BiOCl/BaFe₂O₄ composite. Tauc plots of (b) BiOCl and (c) BaFe₂O₄. (d) Mott-Schottky analysis of BiOCl and BaFe₂O₄.

4.8.2. Photoelectrochemical Analyses

Transient photocurrent response (TPR) was applied to detect the separation efficiency of photogenerated electrons and holes in the photocatalysts. TPR was performed by several repetitive on/off irradiation cycles. When subjected to light, the increase of photoinduced electron-hole pairs were elevated (Zhang et al., 2023). As depicted in Figure 4.16(a), the photocurrent densities of all the BaFe₂O₄/BiOCl composites were higher than those of pure BiOCl and BaFe₂O₄. This demonstrated that the synthesis of heterojunction photocatalysts can efficiently promote the interfacial charge separation. Specifically, the 5 wt% BaFe₂O₄/BiOCl composite with the highest photocurrent density displayed its effectiveness in curtailing the recombination of charge carriers. Electrochemical Impedance Spectroscopy (EIS) was used to detect the separation and transfer of photogenerated charge carriers. A smaller arc radius of the EIS Nyquist plot displays a faster electron transfer rate and better charge carrier separation (Hasanvandian et al., 2022). The charge transfer efficiency of as-fabricated samples was also evaluated by EIS as exhibited in Figure 4.16(b). It was obvious that the arc radius of 5 wt% BaFe₂O₄/BiOCl was the smallest among other samples. This recommended that the former has a higher charge separation efficiency than the latter, which was also consistent with the transient photocurrent response result. Therefore, it can be concluded from the above findings that the development of BaFe₂O₄/BiOCl heterojunction enhanced the separation and transfer of charge carriers, thereby causing an improvement in the photoactivity.

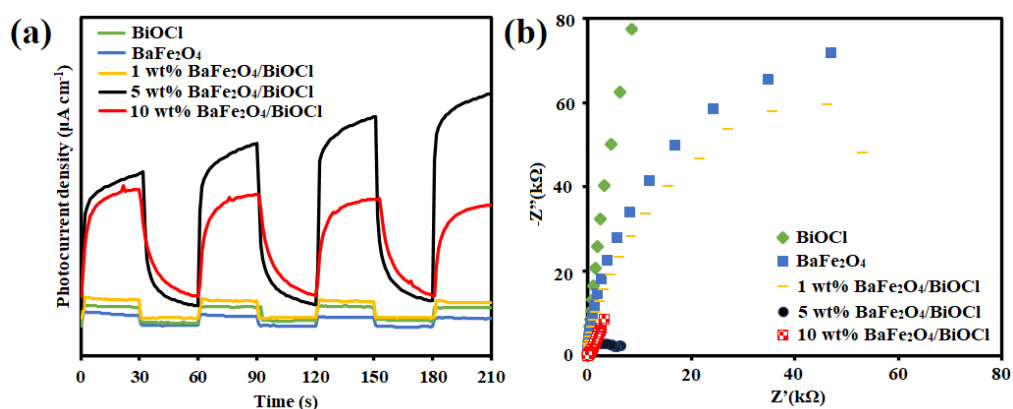


Figure 4.16: (a) Transient photocurrent response curves and (b) EIS spectra of as-synthesized samples.

4.8.3 SSA Analysis

N₂ adsorption–desorption method was adopted to investigate the SSA of as-synthesized samples. In Figure 4.17, the isotherms were of type IV, revealing the mesoporous structure of the fabricated photocatalysts. The SSA of pristine BiOCl, BaFe₂O₄ and 5 wt% BaFe₂O₄/BiOCl were measured to be 2.7, 15.8 and 5.1 m²/g, respectively. The decoration of BaFe₂O₄ on BiOCl improved the surface area of BiOCl, indicating more active sites for photocatalytic reactions. However, no formality between the photoactivity trend of samples and SSA was investigated. This reflected that the SSA of catalyst was not the decisive factor in improving the photoactivity. Thus, the photocatalytic improvement of 5 wt% BaFe₂O₄/BiOCl can be primarily credited to the effective charge separation and migration in the heterojunction structure.

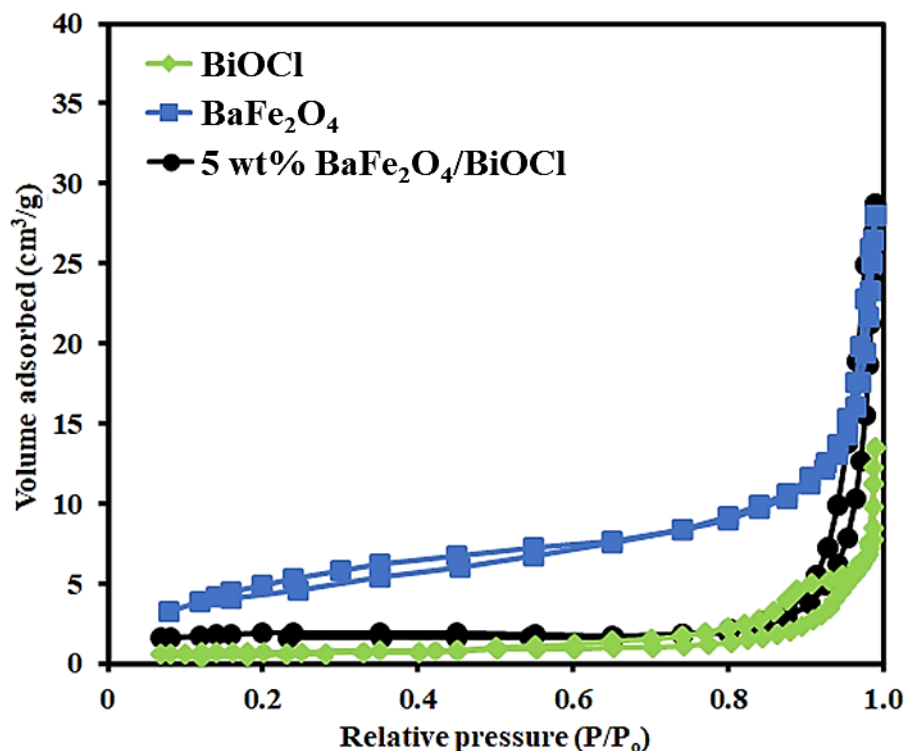


Figure 4.17: Nitrogen adsorption-desorption isotherms of pristine BiOCl, BaFe₂O₄ and 5 wt% BaFe₂O₄/BiOCl composite.

Cao et al. (2020) reported that modifying of BiOCl can increase the specific surface area of photocatalysts. In their SSA analysis, the surface area of BiOCl was 11.12 m²/g, while that of Mn-BiOCl was 13.28 m²/g. In addition, Li et al. (2022) displayed that the SSA of BiOCl, NaNbO₃, and BiOCl/NaNbO₃ were 0.24, 2.00 and 1.32 m²/g. They claimed that the findings of SSA were not decisive factor as the BiOCl/NaNbO₃ achieved better photocatalytic activity. Singh and Mishra (2021) found that the SSA of GO and BaFe₂O₄/rGO were 93.66 m²/g and 91.50 m²/g, respectively. They also mentioned that the BaFe₂O₄/rGO attained low surface area as compared to pristine GO but displayed better photocatalytic activity.

4.8.4 Active Species Detection

Active species (ROS) were induced during photocatalytic decomposition of pre-treated POME using 5 wt% BaFe₂O₄/BiOCl composites. The active species such as ROS including •O₂⁻, •OH, e⁻ and h⁺ acted as vital role during photocatalytic activity process. To detect the major radicals that will influence the photocatalytic activity process, active species trapping tests were performed under visible light irradiation through introducing corresponding scavengers (Juntrapirom et al., 2020; Zhu and Zhou, 2021). The experimental conditions for active species trapping test were: 5wt% BaFe₂O₄/BiOCl (0.5 g/L) under acidic pH conditions (pH 2.0) and pre-treated POME concentration (50 ppm) and 3 mmol/L H₂O₂ concentration and 2.0 mM of scavenger dosage. In Figure 4.18, the photocatalytic activity declined after employed the scavengers. When the EDTA, IPA and catalase was added individually, the degree of decomposition slightly reduced to 80%, 72% and 74%, this demonstrated that h⁺, •OH and e⁻ contributed minor effect in photocatalysis of pre-treated POME respectively. The photodecomposition efficiency declined from 85% to 33% when BQ introduced in photocatalytic decomposition of pre-treated POME, which implying that •O₂⁻ contributed major effect in this photocatalytic decomposition process.

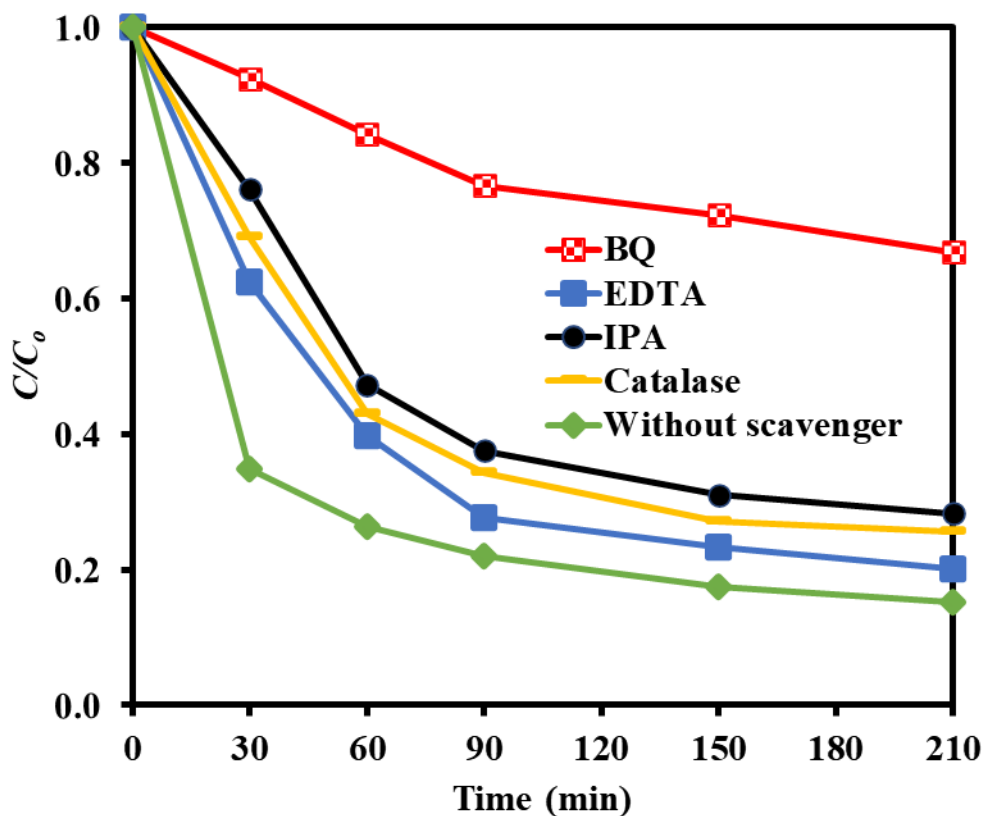


Figure 4.18: Photocatalytic pre-treated POME treatment over 5 wt% BaFe₂O₄/BiOCl in the presence of different scavengers.

Based on the other researchers, Wang et al. (2022) testified BiOCl with vitamin C as scavenger to detect $\bullet\text{O}_2^-$ as the major active species radicals, The findings revealed a significant declined in degradation efficiencies of ciprofloxacin, norfloxacin and tetracycline with vitamin C as scavenger. Du et al. (2022) revealed that the $\bullet\text{O}_2^-$ and h^+ were the dominating active species in the CIP degradation over BiOCl/Cu-doped Bi₂S₃ via BQ and KI as scavengers. They observed that the ciprofloxacin reduced to 28% and 24% with the addition of BQ and KI respectively. By employing BQ and EDTA-2Na as scavengers, Lin et al. (2021) reported that the $\bullet\text{O}_2^-$ and h^+ were the major active species in the photodegradation of tetracycline hydrochloride over CoFe₂O₄/BiOCl.

4.8.5 Photocatalytic Enhancement Mechanism of BaFe₂O₄/BiOCl Composite

A plausible photocatalytic mechanism for photocatalysis of 5 wt% BaFe₂O₄/BiOCl composite was recommended accordance to our research outcomes and literature reviews. The bands position of BiOCl and BaFe₂O₄ were critical matter when designing the efficient composites. The band position of the composites was found to be correlated with the formation of active species. Figure 4.18 shows the plausible photocatalytic improvement mechanism of 5 wt% BaFe₂O₄/BiOCl composites on decomposition of pre-treated POME. Upon visible light irradiation, both BaFe₂O₄ and BiOCl received photon energy, and the electrons (e^-) photoexcited to their CB and left h^+ in the VB. The e^- of BaFe₂O₄ would transfer to the BiOCl owing to the higher CB position of BaFe₂O₄, meanwhile the h^+ of BiOCl would roam in reverse route as the VB of BiOCl was positioned lower than that of BaFe₂O₄. Nevertheless, the amassed e^- and h^+ in the respective semiconductor cannot interact with both O₂ and H₂O, forming O₂ \cdot^- and \cdot OH, respectively ($E_0(\text{O}_2/\text{O}_2\cdot^-) = -0.33 \text{ eV vs NHE}$; $E_0(\text{H}_2\text{O}/\cdot\text{OH}) = 2.72 \text{ eV vs NHE}$) (Dong et al., 2017; He et al., 2021; Miao et al., 2021). This disagreed with the findings of active species trapping test that O₂ \cdot^- and \cdot OH were participated in the photocatalytic process. Therefore, the Z-scheme heterojunction was better to be applied in explicating the photocatalytic mechanism of BaFe₂O₄/BiOCl composite. As depicted in Figure 4.19, the e^- in CB of BiOCl transferred to VB of BaFe₂O₄ and recombined with h^+ . The e^- in BaFe₂O₄ can reduce the O₂ to O₂ \cdot^- as well as H₂O₂ due to its more

negative CB position against the standard redox potentials of $E_0(\text{O}_2/\text{O}_2^{\bullet-})$ and $E_0(\text{O}_2/\text{H}_2\text{O}_2)$. At the same time, the h^+ in VB of BiOCl can oxidize the H_2O to $\bullet\text{OH}$ due to its stronger oxidation ability. Hence, this Z-scheme photogenerated charge transfer mechanism permitted BaFe₂O₄/BiOCl composites not only effectively fostered the e^- - h^+ pairs separation, but also preserved high redox capability and improved their photocatalytic performance.

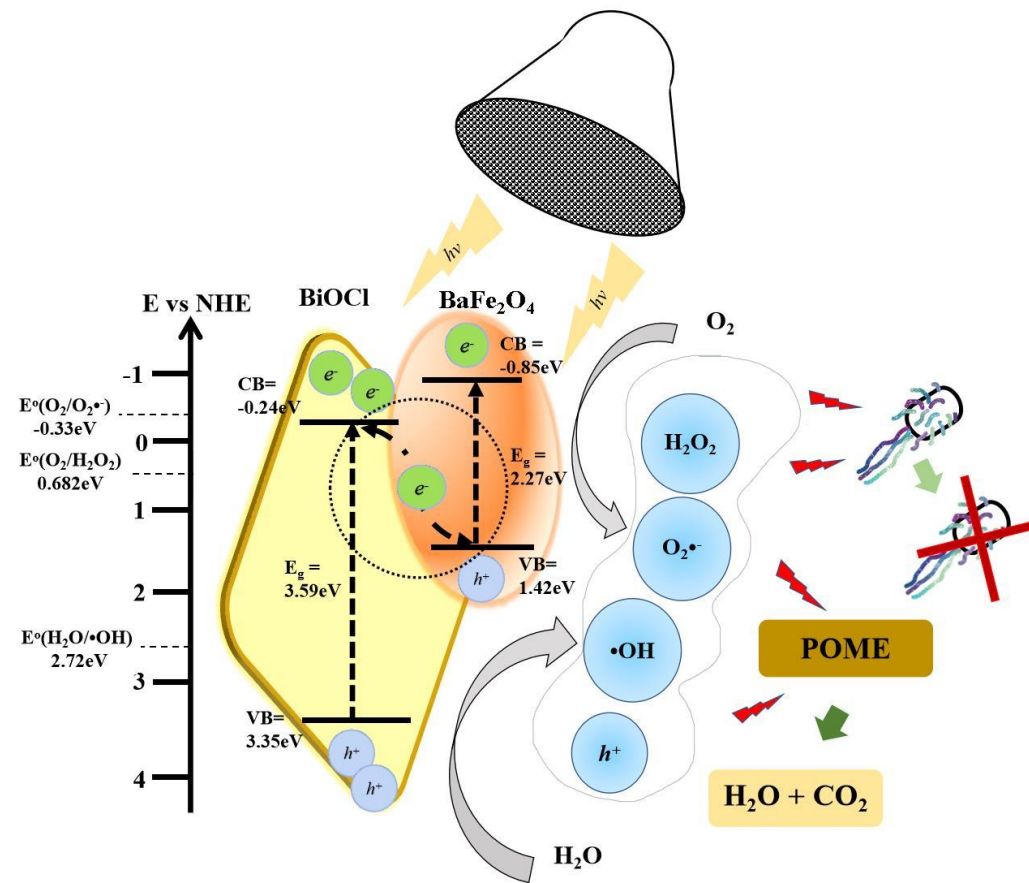


Figure 4.19: Plausible photocatalytic mechanism of BiOCl/BaFe₂O₄ composite.

4.9 Antibacterial Activity

The photocatalytic antibacterial effects of the as-fabricated samples were testified based on the inactivation of *E.coli* and *B. cereus*. Figure 4.20 demonstrates the findings of the photocatalytic antibacterial activities toward *E.coli* and *B.cereus* using BaFe₂O₄, BiOCl and 5 wt% BaFe₂O₄/BiOCl composite. Antibacterial effects of BaFe₂O₄, BiOCl and 5 wt% BaFe₂O₄/BiOCl composite were justified by measuring the diameter of clear zone of inhibition (ZOI) on agar surface surrounding the disks. No obvious bacteria inactivation was monitored under photolysis, indicating that both *E. coli* and *B. cereus* can survive under visible light irradiation. In contrast, the fabricated samples only displayed a little inhibition of bacteria growth in darkness. Nevertheless, in the presence of light irradiation, the 5 wt% BaFe₂O₄/BiOCl was more effective against *E. coli* and *B. cereus* among the samples investigated. The maximum ZOI for the synthesized composite was found to be 17 mm for *E. coli*, whereas for *B. cereus* the value achieved 12 mm. In the case of pristine photocatalysts, the resulting ZOI were only documented as 7-11 mm for both bacteria. Hence, these implied that the decoration of BaFe₂O₄ was efficiently to improve the photocatalytic antibacterial performance of BiOCl.

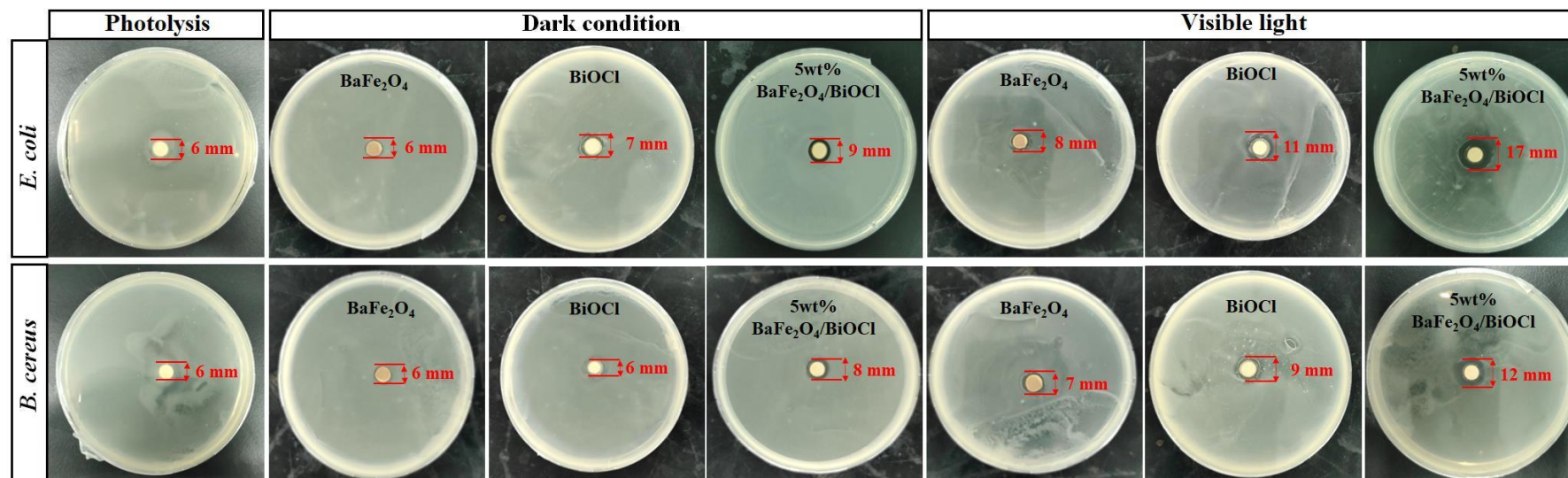


Figure 4.20: Inhibition zones of BiOCl, BaFe₂O₄ and 5 wt% BaFe₂O₄/BiOCl composite towards *E. coli* and *B. cereus* on the agar plates.

The antibacterial properties of BaFe₂O₄/BiOCl composite were associated to the efficient charge carrier separation and led to generation of numerous active species. Under light irradiation, the synthesized composite exhibited its potential to produce different active species such as •O₂⁻, H₂O₂ and •OH, causing the intracellular biomolecule contents seepage. The generated active species can effortlessly infiltrate the cell wall and induced the seepage of protein as well as DNA, which consequently led to cell death (Gnanasekaran et al., 2021; Kong et al., 2021; Munawar et al., 2020) The cell wall of *E. coli* comprised of a thin layer of peptidoglycan, which allowed it more permeable to antibacterial agents that can lead to cell damage and death. Similar results were also reported by other researchers (El-Batal et al., 2017). Shanmugam, Muppudathi, et al. (2020) also reported higher antibacterial effect of g-C₃N₄/Bi₂MoO₆/Ag composites as compared to pristine photocatalyst. In their study, they found that the heterojunction showed the largest ZOI toward *E. coli* and *S. aureus* with diameters of 20 mm and 18 mm respectively. Qureshi et al. (2020) also revealed the application of CdS/Bi₂S₃ able to create ZOI of *E. coli* and *S. aureus* with diameter of 16 mm and 18 mm respectively. This was due to the generation of ROS that can attack the bacterial cell membrane, which lead to severe leakage of organelles and prohibit the growth of bacterial. Vignesh et al. (2018) reported that the antibacterial performance of g-C₃N₄/BiFeO₃/CuO was relied on the induced ROS radicals on the g-C₃N₄/BiFeO₃/CuO composites surfaces as the outer membrane wall of bacteria which can be broken down by ROS radicals, which led to the ZOI of *E. coli* and *S. aureus* with diameter of 17 mm and 18 mm respectively.

CHAPTER 5

CONCLUSION AND RECOMMENDATION

5.1 Conclusion

Direct Z-scheme BaFe₂O₄/BiOCl have been successfully synthesized via a two-step precipitation-hydrothermal route. The as-synthesized samples were analysed by XRD, FTIR, FESEM, TEM, EDX, XPS, VSM, UV-vis DRS, Mott-Schottky, TPR, EIS and specific surface area analyses in order to assess the physical, chemical, optical and electronic properties of the as-synthesized photocatalyst. The characterization results revealed that the two-phase tetragonal BiOCl and orthorhombic BaFe₂O₄ were existed in the 5 wt% BaFe₂O₄/BiOCl composite. In addition, aggregated BaFe₂O₄ particles were vastly covered the surface of BiOCl sheets, constructing a firmly contacted heterostructure. The successfully decoration of BaFe₂O₄ on BiOCl has been confirmed via the XRD, FTIR, FESEM, TEM, EDX and XPS analyses.

The photocatalytic performances of BaFe₂O₄/BiOCl composites were evaluated by POME decomposition under visible light and sunlight irradiation. The BaFe₂O₄/BiOCl composites displayed obvious improvement in photocatalytic decomposition compared to pure BiOCl and BaFe₂O₄. It was credited to the decoration of BaFe₂O₄ on the surface of BiOCl broaden the

light absorption of BiOCl and enhanced the charge carrier separation. Among the composite photocatalysts, 5 wt% BaFe₂O₄/BiOCl composite demonstrated the best photocatalytic activity and was applied in subsequent photocatalytic experiments.

Furthermore, several operating parameters included photocatalyst loading, solution pH, initial POME concentration and H₂O₂ concentration were configured in studying their effects toward the photocatalytic decomposition of POME. The highest photocatalytic efficiency of POME was achieved at conditions: 0.5 g/L 5 wt% BaFe₂O₄/BiOCl, solution pH of 2.0, 50 ppm POME and 3 mmol/L H₂O₂. To study the photocatalytic mechanism of the fabricated composites, TPR and EIS analyses were carried out. Both analyses verified that the development of BaFe₂O₄/BiOCl heterojunction enhanced the separation and transfer of charge carriers, thereby causing an improvement in the photoactivity. The active species scavenging experiments indicated that •O₂⁻, H₂O₂, photogenerated h^+ and •OH were all involved in the POME degradation, among which O₂⁻ was principally responsible for the photoactivity of 5 wt% BaFe₂O₄/BiOCl nanocomposite. Moreover, the 5 wt% BaFe₂O₄/BiOCl composite can be magnetically separated and demonstrated good stability up to four recycling runs. To assess the electrical energy consumption, the 5 wt% BaFe₂O₄/BiOCl displayed to be more economical in decomposing the POME. The 5 wt% BaFe₂O₄/BiOCl nanocomposite also demonstrated good antibacterial efficiencies towards *E. coli* and *B. cereus*. All these features of BaFe₂O₄/BiOCl nanocomposites made them effective visible light-driven photocatalysts for wastewater treatment.

5.2 RECOMMENDATIONS

Upon this research study completion, several suggestions were recommended to be emphasis upon in future photocatalytic works.

1. The photocatalyst can be further developed into ternary composite to investigate its photocatalytic enhancement in different applications such as photocatalytic wastewater treatment, bacteria inactivation and heavy metal reduction.
2. Water splitting capability of as-synthesized photocatalyst could be further evaluated via solar light irradiation which allowed the practicality of photocatalytic treatment in Malaysia by utilizing clean energy to produce green energy.
3. The as-produced photocatalyst should be tested using real pharmaceutical wastewater to investigate its wide applications in wastewater treatment under different operating parameters to an extent.
4. Future commercialization of the produced photocatalyst in different photocatalytic markets at a pilot scale may be explored for potential photocatalytic applications.

REFERENCES

- Abdalazeez, A., Tianle, L., Cao, Y., Wang, W., Abuelgasim, S., & Liu, C. (2022). Syngas production from chemical looping gasification of rice husk-derived biochar using BaFe₂O₄ as an oxygen carrier. *Journal of the Energy Institute*, *105*, 376–387. <https://doi.org/10.1016/j.joei.2022.10.009>
- Abdulrahman, A. F., Ahmed, S. M., Ahmed, N. M., & Almessiere, M. A. (2020). Enhancement of ZnO Nanorods Properties Using Modified Chemical Bath Deposition Method: Effect of Precursor Concentration. *Crystals*, *10*(5), 386. <https://doi.org/10.3390/cryst10050386>
- Abdulsalam, M., Che Man, H., Goh, P. S., Yunos, K. F., Zainal Abidin, Z., Isma M.I., A., & Ismail, A. F. (2020). Permeability and Antifouling Augmentation of a Hybrid PVDF-PEG Membrane Using Nano-Magnesium Oxide as a Powerful Mediator for POME Decolorization. *Polymers*, *12*(3), 549. <https://doi.org/10.3390/polym12030549>
- Adeli, B., & Taghipour, F. (2020). Atomic-scale synthesis of nanoporous gallium–zinc oxynitride-reduced graphene oxide photocatalyst with tailored carrier transport mechanism. *RSC Advances*, *10*(25), 14906–14914. <https://doi.org/10.1039/D0RA01725F>
- Adhikari, S., Mandal, S., & Kim, D.-H. (2019). Z-scheme 2D/1D MoS₂ nanosheet-decorated Ag₂Mo₂O₇ microrods for efficient catalytic oxidation of levofloxacin. *Chemical Engineering Journal*, *373*, 31–43. <https://doi.org/10.1016/j.cej.2019.05.017>
- Aditya, M. N., Chellapandi, T., Prasad, G. K., Venkatesh, M. J. P., Khan, M. M. R., Madhumitha, G., & Roopan, S. M. (2022). Biosynthesis of rod shaped Gd₂O₃ on g-C₃N₄ as nanocomposite for visible light mediated photocatalytic degradation of pollutants and RSM optimization. *Diamond and Related Materials*, *121*, 108790. <https://doi.org/10.1016/j.diamond.2021.108790>
- Affam, A. C., & bin Bistar, A. R. (2020). Oxidation of Palm Oil Mill Effluent Using Hydrogen Peroxide and Catalysed by UV Light/Zinc Oxide. *IOP Conference Series: Materials Science and Engineering*, *736*(4). <https://doi.org/10.1088/1757-899X/736/4/042025>
- Aghdam, S. M., Haghighi, M., Allahyari, S., & Yosefi, L. (2017). Precipitation dispersion of various ratios of BiOI/BiOCl nanocomposite over g-C₃N₄ for promoted visible light nanophotocatalyst used in removal of acid orange 7 from water. *Journal of Photochemistry and Photobiology A: Chemistry*, *338*, 201–212. <https://doi.org/10.1016/j.jphotochem.2017.02.013>

- Ahmad, A., & Ghufuran, R. (2022). Microbial granules on reactors performance during organic butyrate digestion: clean production. *Critical Reviews in Biotechnology*, 1–21. <https://doi.org/10.1080/07388551.2022.2103641>
- Ahmad, I., Ibrahim, N. N. B., Abdullah, N., Koji, I., Mohama, S. E., Khoo, K. S., Cheah, W. Y., Ling, T. C., & Show, P. L. (2022). Bioremediation strategies of palm oil mill effluent and landfill leachate using microalgae cultivation: An approach contributing towards environmental sustainability. *Chinese Chemical Letters*, 107854. <https://doi.org/10.1016/j.ccllet.2022.107854>
- Ahuja, V., Vengarathody, R., Singh, S., & Senguttuvan, P. (2022). Realization of high cycle life bismuth oxychloride Na-ion anode in glyme-based electrolyte. *Journal of Power Sources*, 529. <https://doi.org/10.1016/j.jpowsour.2022.231227>
- Ajala, F., Hamrouni, A., Houas, A., Lachheb, H., Megna, B., Palmisano, L., & Parrino, F. (2018). The influence of Al doping on the photocatalytic activity of nanostructured ZnO: The role of adsorbed water. *Applied Surface Science*, 445, 376–382. <https://doi.org/10.1016/j.apsusc.2018.03.141>
- Akika, F. Z., Benamira, M., Lahmar, H., Trari, M., Avramova, I., & Suzer, Ş. (2020). Structural and optical properties of Cu-doped ZnAl₂O₄ and its application as photocatalyst for Cr(VI) reduction under sunlight. *Surfaces and Interfaces*, 18, 100406. <https://doi.org/10.1016/j.surfin.2019.100406>
- Alam, U., Khan, A., Ali, D., Bahnemann, D., & Muneer, M. (2018). Comparative photocatalytic activity of sol-gel derived rare earth metal (La, Nd, Sm and Dy)-doped ZnO photocatalysts for degradation of dyes. *RSC Advances*, 8(31), 17582–17594. <https://doi.org/10.1039/c8ra01638k>
- Alkaykh, S., Mbarek, A., & Ali-Shattle, E. E. (2020). Photocatalytic degradation of methylene blue dye in aqueous solution by MnTiO₃ nanoparticles under sunlight irradiation. *Heliyon*, 6(4), e03663. <https://doi.org/10.1016/j.heliyon.2020.e03663>
- Aqilah Mohd Razali, N., Norharyati Wan Salleh, W., Hafiza Ismail, N., Zu Nurain Ahmad, S., Awang, A., & Fauzi Ismail, A. (2023). Preparation of visible light-WO₃/g-C₃N₄/PANI photocatalyst onto glass and their photocatalytic properties. *Materials Today: Proceedings*. <https://doi.org/10.1016/j.matpr.2023.01.328>
- Aravind Kumar, J., Sathish, S., Krithiga, T., Praveenkumar, T. R., Lokesh, S., Prabu, D., Annam Renita, A., Prakash, P., & Rajasimman, M. (2022). A comprehensive review on bio-hydrogen production from brewery industrial wastewater and its treatment methodologies. *Fuel*, 319, 123594. <https://doi.org/10.1016/j.fuel.2022.123594>
- Arifin, M. N., Rezaul Karim, K. M., Abdullah, H., & Khan, M. R. (2019). Synthesis of titania doped copper ferrite photocatalyst and its photoactivity towards methylene blue degradation under visible light irradiation. *Bulletin of Chemical Reaction Engineering & Catalysis*, 14(1), 219–227. <https://doi.org/10.9767/bcrec.14.1.3616.219-227>

- Aris, A., Jusoh, M. N. H., & Wahab, N. S. A. A. (2019). *Applications of Advanced Oxidation Processes in Palm Oil Mill Effluent Treatment* (pp. 123–149). <https://doi.org/10.4018/978-1-5225-5766-1.ch006>
- Arutanti, O., Sari, A. A., Berkah, A., Nurdin, M., Fitriady, M. A., Parmawati, Y., Rinaldi, N., Yuniarto, A., & Hadibarata, T. (2020). Advanced Degradation of Lignin from Palm Oil Mill Effluent (POME) by a Combination of Photocatalytic-Fenton Treatment and TiO₂ Nanoparticle as the Catalyst. *Water, Air, and Soil Pollution*, 231(6). <https://doi.org/10.1007/s11270-020-04617-8>
- Asadzadeh-Khaneghah, S., Habibi-Yangjeh, A., & Nakata, K. (2019). Decoration of carbon dots over hydrogen peroxide treated graphitic carbon nitride: Exceptional photocatalytic performance in removal of different contaminants under visible light. *Journal of Photochemistry and Photobiology A: Chemistry*, 374, 161–172. <https://doi.org/10.1016/j.jphotochem.2019.02.002>
- Attri, P., Garg, P., Chauhan, M., Singh, R., Sharma, R. K., Kumar, S., Lim, D.-K., & Chaudhary, G. R. (2023). Metal doped BiOCl Nano-architectures (M-BiOCl, M = Ni, Mo, Cd, Co) for efficient visible light photocatalytic and antibacterial behaviour. *Journal of Environmental Chemical Engineering*, 109498. <https://doi.org/10.1016/j.jece.2023.109498>
- Aziz, F. F. A., Jalil, A. A., Hassan, N. S., Fauzi, A. A., & Azami, M. S. (2021). Simultaneous photocatalytic reduction of hexavalent chromium and oxidation of p-cresol over AgO decorated on fibrous silica zirconia. *Environmental Pollution*, 285, 117490. <https://doi.org/10.1016/j.envpol.2021.117490>
- Baaloudj, O., Assadi, I., Nasrallah, N., El Jery, A., Khezami, L., & Assadi, A. A. (2021). Simultaneous removal of antibiotics and inactivation of antibiotic-resistant bacteria by photocatalysis: A review. In *Journal of Water Process Engineering* (Vol. 42). Elsevier Ltd. <https://doi.org/10.1016/j.jwpe.2021.102089>
- Bağcıoğlu, M., Fricker, M., Jöhler, S., & Ehling-Schulz, M. (2019). Detection and identification of bacillus cereus, bacillus cytotoxicus, bacillus thuringiensis, bacillus mycoides and bacillus weihenstephanensis via machine learning based FTIR spectroscopy. *Frontiers in Microbiology*, 10(APR). <https://doi.org/10.3389/fmicb.2019.00902>
- Bera, S., Ghosh, S., Maiyalagan, T., & Basu, R. N. (2022). Band Edge Engineering of BiOX/CuFe₂O₄ Heterostructures for Efficient Water Splitting. *ACS Applied Energy Materials*, 5(3), 3821–3833. <https://doi.org/10.1021/acsaem.2c00296>
- Bouddouch, A., Akhsassi, B., Amaterz, E., Bakiz, B., Taoufyq, A., Villain, S., Guinneton, F., el Aamrani, A., Gavarrı, J. R., & Benlhachemi, A. (2022). Photodegradation under UV Light Irradiation of Various Types and Systems of Organic Pollutants in the Presence of a Performant BiPO₄ Photocatalyst. *Catalysts*, 12(7). <https://doi.org/10.3390/catal12070691>
- Cai, J., Huang, J., Wang, S., Iocozzia, J., Sun, Z., Sun, J., Yang, Y., Lai, Y., & Lin, Z. (2019). Crafting Mussel-Inspired Metal Nanoparticle-Decorated Ultrathin

- Graphitic Carbon Nitride for the Degradation of Chemical Pollutants and Production of Chemical Resources. *Advanced Materials*, 31(15), 1806314. <https://doi.org/10.1002/adma.201806314>
- Cao, J., Li, J., Chu, W., & Cen, W. (2020). Facile synthesis of Mn-doped BiOCl for metronidazole photodegradation: Optimization, degradation pathway, and mechanism. *Chemical Engineering Journal*, 400, 125813. <https://doi.org/10.1016/j.cej.2020.125813>
- Cao, T., Zhou, D., Wang, X., & Cui, C. (2022). Photocatalytic degradation of bisphenol A over Co-BiOCl/biochar hybrid catalysts: Properties, efficiency and mechanism. *Journal of Molecular Liquids*, 362, 119622. <https://doi.org/10.1016/j.molliq.2022.119622>
- Cao, W., Jiang, C., Chen, C., Zhou, H., & Wang, Y. (2021). A novel Z-scheme CdS/Bi₄O₅Br₂ heterostructure with mechanism analysis: Enhanced photocatalytic performance. *Journal of Alloys and Compounds*, 861, 158554. <https://doi.org/10.1016/j.jallcom.2020.158554>
- Cao, Y., Ren, Y., Zhang, J., Xie, T., & Lin, Y. (2021). Activation of H₂O₂ by photo-generated electrons for enhanced visible light driven methylene blue degradation with ZnFe₂O₄/BiVO₄ heterojunction. *Optical Materials*, 121. <https://doi.org/10.1016/j.optmat.2021.111637>
- Chachvalvutikul, A., & Kaowphong, S. (2020). Direct Z-scheme FeVO₄ /BiOCl heterojunction as a highly efficient visible-light-driven photocatalyst for photocatalytic dye degradation and Cr(VI) reduction. *Nanotechnology*, 31(14), 145704. <https://doi.org/10.1088/1361-6528/ab61d1>
- Chan, Y. J., Chong, R. J. W., Chong, M. F., Ng, D. K. S., & Lim, L. K. (2023). Performance and Stability of Pre-commercialized Integrated Anaerobic–Aerobic Bioreactor (IAAB) for the Treatment of Palm Oil Mill Effluent (POME). In *Sustainable Technologies for the Oil Palm Industry* (pp. 301–323). Springer Nature Singapore. https://doi.org/10.1007/978-981-19-4847-3_12
- Chankhanittha, T., Komchoo, N., Senasu, T., Piriyanon, J., Youngme, S., Hemavibool, K., & Nanan, S. (2021). Silver decorated ZnO photocatalyst for effective removal of reactive red azo dye and ofloxacin antibiotic under solar light irradiation. *Colloids and Surfaces A: Physicochemical and Engineering Aspects*, 626, 127034. <https://doi.org/10.1016/j.colsurfa.2021.127034>
- Charles, A., Khan, M. R., Ng, K. H., Wu, T. Y., Lim, J. W., Wongsakulphasatch, S., Witoon, T., & Cheng, C. K. (2019). Facile synthesis of CaFe₂O₄ for visible light driven treatment of polluting palm oil mill effluent: Photokinetic and scavenging study. *Science of The Total Environment*, 661, 522–530. <https://doi.org/10.1016/j.scitotenv.2019.01.195>
- Chen, F., Bian, K., Li, H., Tang, Y., Hao, C., & Shi, W. (2022). A novel CeO₂/MIL101 (Fe) heterojunction for enhanced photocatalytic degradation of tetracycline under visible-light irradiation. *Journal of Chemical Technology & Biotechnology*, 97(7), 1884–1892. <https://doi.org/10.1002/jctb.7061>

- Chen, J., Ren, Q., Ding, Y., Xiong, C., & Guo, W. (2021). Synthesis of bifunctional composites Ag/BiOCl/diatomite: Degradation of tetracycline and evaluation of antimicrobial activity. *Journal of Environmental Chemical Engineering*, 9(6). <https://doi.org/10.1016/j.jece.2021.106476>
- Chen, Y., Jiang, Z., Xu, L., Liu, C., Cheng, Y., Zou, Y., & Zhang, Q. (2021). Composite magnetic photocatalyst Bi₂₄O₃₁Br₁₀/NiFe₂O₄: Hydrothermal preparation, characterization and photocatalytic mechanism. *Materials Science in Semiconductor Processing*, 126, 105669. <https://doi.org/10.1016/j.mssp.2021.105669>
- Cheng, Y. W., Chang, Y. S., Ng, K. H., Wu, T. Y., & Cheng, C. K. (2017). Photocatalytic restoration of liquid effluent from oil palm agroindustry in Malaysia using tungsten oxides catalyst. *Journal of Cleaner Production*, 162, 205–219. <https://doi.org/10.1016/j.jclepro.2017.06.023>
- Cheng, Y. W., Chong, C. C., Lam, M. K., Ayoub, M., Cheng, C. K., Lim, J. W., Yusup, S., Tang, Y., & Bai, J. (2021). Holistic process evaluation of non-conventional palm oil mill effluent (POME) treatment technologies: A conceptual and comparative review. *Journal of Hazardous Materials*, 409, 124964. <https://doi.org/10.1016/j.jhazmat.2020.124964>
- Chin, Y.-H., Sin, J.-C., Lam, S.-M., Zeng, H., Lin, H., Li, H., Huang, L., & Mohamed, A. R. (2022). 3-D/3-D Z-Scheme Heterojunction Composite Formed by Marimo-like Bi₂WO₆ and Mammillaria-like ZnO for Expeditious Sunlight Photodegradation of Dimethyl Phthalate. *Catalysts*, 12(11), 1427. <https://doi.org/10.3390/catal12111427>
- Choi, J., Kim, H., Lee, K., Chen, N., Kim, M. S., Seo, J., Lee, D., Cho, H., Kim, H., Lee, J., Lee, H., & Lee, C. (2022). Bicarbonate-enhanced generation of hydroxyl radical by visible light-induced photocatalysis of H₂O₂ over WO₃: Alteration of electron transfer mechanism. *Chemical Engineering Journal*, 432, 134401. <https://doi.org/10.1016/j.cej.2021.134401>
- Cui, K., Wang, X., Tai, M., Gao, B., & Su, B. (2020). Facile synthesis of intercalated Z-scheme Bi₂O₄/g-C₃N₄ composite photocatalysts for effective removal of 2-Mercaptobenzothiazole: Degradation pathways and mechanism. *Journal of the Taiwan Institute of Chemical Engineers*, 111, 212–221. <https://doi.org/10.1016/j.jtice.2020.03.007>
- Dang, J., Guo, J., Wang, L., Guo, F., Shi, W., Li, Y., & Guan, W. (2022). Construction of Z-scheme Fe₃O₄/BiOCl/BiOI heterojunction with superior recyclability for improved photocatalytic activity towards tetracycline degradation. *Journal of Alloys and Compounds*, 893, 162251. <https://doi.org/10.1016/j.jallcom.2021.162251>
- Dashti, A. F., Aziz, H. A., Ibrahim, A. H., & Zahed, M. A. (2020). Suspended Solid Removal of Palm Oil Mill Effluent Using Horizontal Roughing Filter and Calcinated Limestone. *Water, Air, & Soil Pollution*, 231(8), 393. <https://doi.org/10.1007/s11270-020-04755-z>

- Dilip, R., & Jayaprakash, R. (2021). Supremacy of Magnetic Behaviour in n-Heptane Based M Doped Barium Ferrite (BaFe₂O₄) Nanoparticles (M: Co, Ni and Mn). *Journal of Inorganic and Organometallic Polymers and Materials* 2021 31:7, 31(7), 3154–3163. <https://doi.org/10.1007/S10904-021-01963-W>
- Dong, F., Chen, Y., Chen, D., & Shao, Z. (2014). Surprisingly High Activity for Oxygen Reduction Reaction of Selected Oxides Lacking Long Oxygen-Ion Diffusion Paths at Intermediate Temperatures: A Case Study of Cobalt-Free BaFeO_{3-δ}. *ACS Applied Materials & Interfaces*, 6(14), 11180–11189. <https://doi.org/10.1021/am502240m>
- Dong, H., Xiao, M., Li, J., Hu, W., Sun, X., Liu, Y., Zhang, P., Che, G., & Liu, C. (2020). Construction of H-TiO₂/BiOCl heterojunction with improved photocatalytic activity under the visible and near-infrared light. *Journal of Photochemistry and Photobiology A: Chemistry*, 392, 112369. <https://doi.org/10.1016/j.jphotochem.2020.112369>
- Dong, H., Zhang, X., Li, J., Zhou, P., Yu, S., Song, N., Liu, C., Che, G., & Li, C. (2020). Construction of morphology-controlled nonmetal 2D/3D homojunction towards enhancing photocatalytic activity and mechanism insight. *Applied Catalysis B: Environmental*, 263, 118270. <https://doi.org/10.1016/j.apcatb.2019.118270>
- Dong, P., Hou, G., Xi, X., Shao, R., & Dong, F. (2017). WO₃-based photocatalysts: morphology control, activity enhancement and multifunctional applications. *Environmental Science: Nano*, 4(3), 539–557. <https://doi.org/10.1039/C6EN00478D>
- Du, F., Lai, Z., Tang, H., Wang, H., & Zhao, C. (2022). Construction and application of BiOCl/Cu-doped Bi₂S₃ composites for highly efficient photocatalytic degradation of ciprofloxacin. *Chemosphere*, 287, 132391. <https://doi.org/10.1016/j.chemosphere.2021.132391>
- Duong, H. P., Mashiyama, T., Kobayashi, M., Iwase, A., Kudo, A., Asakura, Y., Yin, S., Kakihana, M., & Kato, H. (2019). Z-scheme water splitting by microspherical Rh-doped SrTiO₃ photocatalysts prepared by a spray drying method. *Applied Catalysis B: Environmental*, 252, 222–229. <https://doi.org/10.1016/j.apcatb.2019.04.009>
- Dursun, S., Kaya, İ. C., Kocabaş, M., Akyildiz, H., & Kalem, V. (2020). Visible light active heterostructured photocatalyst system based on CuO plate-like particles and SnO₂ nanofibers. *International Journal of Applied Ceramic Technology*, 17(3), 1479–1489. <https://doi.org/10.1111/ijac.13467>
- Mugunthan, E., Saidutta, M.B., & Jagadeeshbabu, P.E., (2019). Photocatalytic activity of ZnO-WO₃ for diclofenac degradation under visible light irradiation. *Journal of Photochemistry and Photobiology A: Chemistry*, 383, 111993. <https://doi.org/10.1016/j.jphotochem.2019.111993>
- El-Batal, A.I., El-Sayyad, G.S., El-Ghamry, A., Agaypi, K.M., Elsayed M.A., Gobara, M., (2017). Melanin-gamma rays assistants for bismuth oxide nanoparticles

- synthesis at room temperature for enhancing antimicrobial, and photocatalytic activities,. *J. Photochem. Photobiol. B: Biol*, 173, 120-139. <http://dx.doi.org/10.1016/j.jphotobiol.2017.05.030>.
- Efros, A. L., & Brus, L. E. (2021). Nanocrystal Quantum Dots: From Discovery to Modern Development. *ACS Nano*, 15(4), 6192–6210. <https://doi.org/10.1021/acsnano.1c01399>
- Eskizeybek, V., Sarı, F., Gülce, H., Gülce, A., & Avcı, A. (2012). Preparation of the new polyaniline/ZnO nanocomposite and its photocatalytic activity for degradation of methylene blue and malachite green dyes under UV and natural sun lights irradiations. *Applied Catalysis B: Environmental*, 119–120, 197–206. <https://doi.org/10.1016/j.apcatb.2012.02.034>
- Fadli, M. H., Ibadurrohman, M., & Slamet, S. (2021). Microplastic Pollutant Degradation in Water Using Modified TiO₂ Photocatalyst Under UV-Irradiation. *IOP Conference Series: Materials Science and Engineering*, 1011(1), 012055. <https://doi.org/10.1088/1757-899X/1011/1/012055>
- Fan, X., Sokorai, K. J. B., & Gurtler, J. B. (2020). Advanced oxidation process for the inactivation of Salmonella typhimurium on tomatoes by combination of gaseous ozone and aerosolized hydrogen peroxide. *International Journal of Food Microbiology*, 312, 108387. <https://doi.org/10.1016/j.ijfoodmicro.2019.108387>
- Fan, Z., Luan, J., Zhu, C., & Liu, F. (2021). Depositing Ag₂S quantum dots as electron mediators in SnS₂/g-C₃N₄ nanosheet composites for constructing Z-scheme heterojunction with enhanced photocatalytic performance. *Materials Research Bulletin*, 133, 111045. <https://doi.org/10.1016/j.materresbull.2020.111045>
- Farhan Hanafi, M., & Sapawe, N. (2019). Electrogenerated Zirconia (EGZrO₂) Nanoparticles as Recyclable Catalyst for Effective Photocatalytic Degradation of Phenol. *Materials Today: Proceedings*, 19, 1537–1540. <https://doi.org/10.1016/j.matpr.2019.11.180>
- Fattahi, A., Arlos, M. J., Bragg, L. M., Kowalczyk, S., Liang, R., Schneider, O. M., Zhou, N., & Servos, M. R. (2021). Photodecomposition of pharmaceuticals and personal care products using P25 modified with Ag nanoparticles in the presence of natural organic matter. *Science of The Total Environment*, 752, 142000. <https://doi.org/10.1016/j.scitotenv.2020.142000>
- Feilizadeh, M., Attar, F., & Mahinpey, N. (2019). Hydrogen peroxide-assisted photocatalysis under solar light irradiation: Interpretation of interaction effects between an active photocatalyst and H₂O₂. *The Canadian Journal of Chemical Engineering*, 97(7), 2009–2014. <https://doi.org/https://doi.org/10.1002/cjce.23455>
- Garrido-Cardenas, J. A., Esteban-García, B., Agüera, A., Sánchez-Pérez, J. A., & Manzano-Agugliaro, F. (2019). Wastewater Treatment by Advanced Oxidation Process and Their Worldwide Research Trends. *International Journal of*

Environmental Research and Public Health, 17(1), 170.
<https://doi.org/10.3390/ijerph17010170>

- Ghosh, S., Modak, A., Samanta, A., Kole, K., & Jana, S. (2021). Recent progress in materials development for CO₂ conversion: issues and challenges. *Materials Advances*, 2(10), 3161–3187. <https://doi.org/10.1039/D1MA00107H>
- Gowda, P., Reddy, P. H., & Kumar, S. (2022). Deregulated mitochondrial microRNAs in Alzheimer's disease: Focus on synapse and mitochondria. *Ageing Research Reviews*, 73, 101529. <https://doi.org/10.1016/j.arr.2021.101529>
- Grilla, E., Kagialari, M. N., Petala, A., Frontistis, Z., & Mantzavinos, D. (2021). Photocatalytic Degradation of Valsartan by MoS₂/BiOCl Heterojunctions. *Catalysts*, 11(6), 650. <https://doi.org/10.3390/catal11060650>
- Gu, X., Yan, Q., Wei, Y., Luo, Y., Sun, Y., Zhao, D., Ji, F., & Xu, X. (2019). Visible-light-responsive photocatalyst with a microsphere structure: preparation and photocatalytic performance of CQDs@BiOCl. *Journal of Materials Science: Materials in Electronics*, 30(17), 16321–16336. <https://doi.org/10.1007/s10854-019-02003-7>
- Guaraldo, T. T., Vakili, R., Wenk, J., & Mattia, D. (2023). Highly efficient ZnO photocatalytic foam reactors for micropollutant degradation. *Chemical Engineering Journal*, 455, 140784. <https://doi.org/10.1016/j.cej.2022.140784>
- Gupta, G., & Kansal, S. K. (2019). Novel 3-D flower like Bi₃O₄Cl/BiOCl p-n heterojunction nanocomposite for the degradation of levofloxacin drug in aqueous phase. *Process Safety and Environmental Protection*, 128, 342–352. <https://doi.org/10.1016/j.psep.2019.06.008>
- Hasanvandian, F., Zehtab Salmasi, M., Moradi, M., Farshineh Saei, S., Kakavandi, B., & Rahman Setayesh, S. (2022). Enhanced spatially coupling heterojunction assembled from CuCo₂S₄ yolk-shell hollow sphere capsulated by Bi-modified TiO₂ for highly efficient CO₂ photoreduction. *Chemical Engineering Journal*, 444, 136493. <https://doi.org/10.1016/j.cej.2022.136493>
- He, Z., Yang, H., Su, J., Xia, Y., Fu, X., Wang, L., & Kang, L. (2021). Construction of multifunctional dual Z-scheme composites with enhanced photocatalytic activities for degradation of ciprofloxacin. *Fuel*, 294, 120399. <https://doi.org/10.1016/j.fuel.2021.120399>
- Hiremath, P. G., S, R., Binnal, P., & Theodore, T. (2021). Fluoride Contamination in Underground Water and Its Treatment. In *Management of Contaminants of Emerging Concern (CEC) in Environment* (pp. 249–280). Elsevier. <https://doi.org/10.1016/B978-0-12-822263-8.00009-9>
- Hou, J., Zhang, T., Jiang, T., Wu, X., Zhang, Y., Tahir, M., Hussain, A., Luo, M., Zou, J., & Wang, X. (2021). Fast preparation of oxygen vacancy-rich 2D/2D bismuth oxyhalides-reduced graphene oxide composite with improved visible-light

- photocatalytic properties by solvent-free grinding. *Journal of Cleaner Production*, 328, 129651. <https://doi.org/10.1016/j.jclepro.2021.129651>
- Hu, H., Wang, T., Peng, L., Ling, X., He, Y., Sun, M., Yang, M., & Deng, C. (2022). Microwave-assisted synthesis of Z-scheme CdS/BiOBr heterojunction for improved visible-light photocatalytic degradation of organic dyes. *Applied Physics A*, 128(5), 452. <https://doi.org/10.1007/s00339-022-05595-w>
- Huang, Y., Zhang, X., & Zeng, J. (2021). Ternary heterojunctions catalyst of BiOCl nanosheets with the {001} facets compounded of Pt and reduced graphene oxide for enhancing photocatalytic activity. *Journal of Materials Science: Materials in Electronics*, 32(3), 2667–2684. <https://doi.org/10.1007/s10854-020-04758-w>
- Hui, K., Dai, F., Guo, L., Li, L., & Wang, X. (2022). Ferroelectric-assisted charge carrier separation over Bi₂MoO₆ nanosheets for photocatalytic dye degradation. *Nanoscale*, 14(39), 14661–14669. <https://doi.org/10.1039/D2NR02911A>
- Huzir, N. M., Aziz, M. M. A., Ismail, S. B., Mahmood, N. A. N., Umor, N. A., & Fua'ad Syed Muhammad, S. A. (2019). Optimization of coagulation-flocculation process for the palm oil mill effluent treatment by using rice husk ash. *Industrial Crops and Products*, 139, 111482. <https://doi.org/10.1016/j.indcrop.2019.111482>
- Irfan, M., Nawaz, R., Khan, J. A., Ullah, H., Haneef, T., Legutko, S., Rahman, S., Józwick, J., Alsaiani, M. A., Khan, M. K. A., Mursal, S. N. F., AlKahtani, F. S., Alshorman, O., & Ghanim, A. A. J. (2021). Synthesis and Characterization of Manganese-Modified Black TiO₂ Nanoparticles and Their Performance Evaluation for the Photodegradation of Phenolic Compounds from Wastewater. *Materials*, 14(23), 7422. <https://doi.org/10.3390/ma14237422>
- Ismael, M., & Wark, M. (2022). Photocatalytic activity of CoFe₂O₄/g-C₃N₄ nanocomposite toward degradation of different organic pollutants and their inactivity toward hydrogen production: The role of the conduction band position. *FlatChem*, 32, 100337. <https://doi.org/10.1016/j.flatc.2022.100337>
- Jaffari, Z. H., Lam, S. M., Sin, J. C., & Mohamed, A. R. (2019). Constructing magnetic Pt-loaded BiFeO₃ nanocomposite for boosted visible light photocatalytic and antibacterial activities. *Environmental Science and Pollution Research* 2019 26:10, 26(10), 10204–10218. <https://doi.org/10.1007/S11356-019-04503-9>
- Jia, Z., Li, T., Zheng, Z., Zhang, J., Liu, J., Li, R., Wang, Y., Zhang, X., Wang, Y., & Fan, C. (2020). The BiOCl/diatomite composites for rapid photocatalytic degradation of ciprofloxacin: Efficiency, toxicity evaluation, mechanisms and pathways. *Chemical Engineering Journal*, 380, 122422. <https://doi.org/10.1016/j.cej.2019.122422>
- Jiang, J., Mu, Z., Xing, H., Wu, Q., Yue, X., & Lin, Y. (2019). Insights into the synergetic effect for enhanced UV/visible-light activated photodegradation activity via Cu-ZnO photocatalyst. *Applied Surface Science*, 478, 1037–1045. <https://doi.org/10.1016/j.apsusc.2019.02.019>

- Jiang, R., Lu, G., Yan, Z., Wu, D., Zhou, R., & Bao, X. (2019). Insights into a CQD-SnNb₂O₆/BiOCl Z-scheme system for the degradation of benzocaine: Influence factors, intermediate toxicity and photocatalytic mechanism. *Chemical Engineering Journal*, 374, 79–90. <https://doi.org/10.1016/j.cej.2019.05.176>
- Jiao, J., Wan, J., Ma, Y., & Wang, Y. (2019). Enhanced photocatalytic activity of AgNPs-in-CNTs with hydrogen peroxide under visible light irradiation. *Environmental Science and Pollution Research*, 26(25), 26389–26396. <https://doi.org/10.1007/s11356-019-05877-6>
- Juntraprom, S., Anuchai, S., Thongsook, O., Pornsuwan, S., Meepowan, P., Thavornnyutikarn, P., Phanichphant, S., Tantraviwat, D., Inceesungvorn, B., (2020) “Photocatalytic activity enhancement of G-C₃N₄/BiOBr in selective transformation of primary amines to imines and its reaction mechanism,” *Chemical Engineering Journal*, 394, p. 124934. Available at: <https://doi.org/10.1016/j.cej.2020.124934>.
- Kafian, S., & Sadeghzadeh-Attar, A. (2022). Photocatalytic degradation of Basic Blue 41 dye under visible light over SrTiO₃/Ag₃PO₄ hetero-nanostructures. *International Journal of Applied Ceramic Technology*, 19(6), 3347–3357. <https://doi.org/10.1111/ijac.14148>
- Kamali, M., Alavi-Borazjani, S. A., Khodaparast, Z., Khalaj, M., Jahanshahi, A., Costa, E., & Capela, I. (2019). Additive and additive-free treatment technologies for pulp and paper mill effluents: Advances, challenges and opportunities. *Water Resources and Industry*, 21, 100109. <https://doi.org/10.1016/j.wri.2019.100109>
- Kamari, A., Jumadi, J., Abdul Rahim, N., Fatimah, I., & Sukkaew, A. (2021). A Brief Review of Physico-Chemical Treatment Techniques for Palm Oil Mill Effluent (POME). *Current Applied Science and Technology*, 22(5). <https://doi.org/10.55003/cast.2022.05.22.013>
- Karim, A., Islam, M. A., Yousuf, A., Khan, Md. M. R., & Faizal, C. K. M. (2019). Microbial Lipid Accumulation through Bioremediation of Palm Oil Mill Wastewater by *Bacillus cereus*. *ACS Sustainable Chemistry & Engineering*, 7(17), 14500–14508. <https://doi.org/10.1021/acssuschemeng.9b01960>
- Keerthana, SP., Yuvakkumar, R., Ravi, G., Al-Sehemi, A. G., & Velauthapillai, D. (2022). Synthesis of pure and lanthanum-doped barium ferrite nanoparticles for efficient removal of toxic pollutants. *Journal of Hazardous Materials*, 424, 127604. <https://doi.org/10.1016/j.jhazmat.2021.127604>
- Kenfoud, H., Nasrallah, N., Baaloudj, O., Belabed, C., Chaabane, T., & Trari, M. (2022). Opto-electrochemical characteristics of synthesized BaFe₂O₄ nanocomposites: Photocatalytic degradation and hydrogen generation investigation. *International Journal of Hydrogen Energy*, 47(24), 12039–12051. <https://doi.org/10.1016/j.ijhydene.2022.01.232>
- Kenfoud, H., Nasrallah, N., Baaloudj, O., Derridj, F., & Trari, M. (2022). Enhanced photocatalytic reduction of Cr(VI) by the novel hetero-system BaFe₂O₄/SnO₂.

Journal of Physics and Chemistry of Solids, 160, 110315.
<https://doi.org/10.1016/j.jpics.2021.110315>

- Khan, A., Danish, M., Alam, U., Zafar, S., & Muneer, M. (2020). Facile Synthesis of a Z-Scheme ZnIn₂S₄/MoO₃ Heterojunction with Enhanced Photocatalytic Activity under Visible Light Irradiation. *ACS Omega*, 5(14), 8188–8199. <https://doi.org/10.1021/acsomega.0c00446>
- Khoiriah, K., Safni, S., Syukri, S., & Gunlazuardi, J. (2020). THE OPERATIONAL PARAMETERS EFFECT ON PHOTOCATALYTIC DEGRADATION OF DIAZINON USING CARBON AND NITROGEN MODIFIED TiO₂. *Rasayan Journal of Chemistry*, 13(03), 1919–1925. <https://doi.org/10.31788/RJC.2020.1335743>
- Kleiman, A., Meichtry, J. M., Vega, D., Litter, M. I., & Márquez, A. (2020). Photocatalytic activity of TiO₂ films prepared by cathodic arc deposition: Dependence on thickness and reuse of the photocatalysts. *Surface and Coatings Technology*, 382, 125154. <https://doi.org/10.1016/j.surfcoat.2019.125154>
- Kumar, A., Chandel, M., Sharma, A., Thakur, M., Kumar, A., Pathania, D., & Singh, L. (2021). Robust visible light active PANI/LaFeO₃/CoFe₂O₄ ternary heterojunction for the photo-degradation and mineralization of pharmaceutical effluent: Clozapine. *Journal of Environmental Chemical Engineering*, 9(5), 106159. <https://doi.org/10.1016/j.jece.2021.106159>
- Kumar, A., Sharma, G., Kumari, A., Guo, C., Naushad, Mu., Vo, D.-V. N., Iqbal, J., & Stadler, F. J. (2021). Construction of dual Z-scheme g-C₃N₄/Bi₄Ti₃O₁₂/Bi₄O₅I₂ heterojunction for visible and solar powered coupled photocatalytic antibiotic degradation and hydrogen production: Boosting via I⁻/I₃⁻ and Bi³⁺/Bi⁵⁺ redox mediators. *Applied Catalysis B: Environmental*, 284, 119808. <https://doi.org/10.1016/j.apcatb.2020.119808>
- Kundu, A., Sharma, S., & Basu, S. (2021). Modulated BiOCl nanoplates with porous g-C₃N₄ nanosheets for photocatalytic degradation of color/colorless pollutants in natural sunlight. *Journal of Physics and Chemistry of Solids*, 154. <https://doi.org/10.1016/j.jpics.2021.110064>
- Kuok, K. K., Chiu, P. C., Rahman, Md. R., Bakri, M. K. bin, & Chin, M. Y. (2022). Effectiveness of Centralized Wastewater Treatment Plant in Removing Emerging Contaminants: A Case Study at Kuching, Malaysia. *Journal of Water Resource and Protection*, 14(09), 650–663. <https://doi.org/10.4236/jwarp.2022.149034>
- Lagerstrom, K. M., & Hadly, E. A. (2021). The under-investigated wild side of *Escherichia coli*: genetic diversity, pathogenicity and antimicrobial resistance in wild animals. *Proceedings of the Royal Society B: Biological Sciences*, 288(1948), rspb.2021.0399. <https://doi.org/10.1098/rspb.2021.0399>
- Lau, K. J., Lim, A., Chew, J. J., Ngu, L. H., & Sunarso, J. (2021). Treatment and decolourisation of treated palm oil mill effluent (POME) using oil palm trunk-derived activated carbon as adsorbent. *IOP Conference Series: Materials*

Science and Engineering, 1195(1), 012025. <https://doi.org/10.1088/1757-899X/1195/1/012025>

- Lee, M. D., Mohamad, N. F. A., Hassan, N. A., & Lee, P. S. (2021). Performance of Oil Palm Frond Fiber as Filtration Material in Palm Oil Mill Effluent Treatment. *IOP Conference Series: Earth and Environmental Science*, 690(1), 012039. <https://doi.org/10.1088/1755-1315/690/1/012039>
- Lee, S.-S., Huy, B. T., Phuong, N. T. K., Tung, D. K., & Lee, Y.-I. (2019). Enhanced performance in the photocatalytic degradation of 2,4,5-Trichlorophenoxyacetic acid over Eu-doped Bi₂WO₆ under visible light irradiation. *Korean Journal of Chemical Engineering*, 36(10), 1716–1723. <https://doi.org/10.1007/s11814-019-0371-2>
- Lee, Z. S., Chin, S. Y., Lim, J. W., Witoon, T., & Cheng, C. K. (2019). Treatment technologies of palm oil mill effluent (POME) and olive mill wastewater (OMW): A brief review. *Environmental Technology & Innovation*, 15, 100377. <https://doi.org/10.1016/j.eti.2019.100377>
- Li, L., Cao, W., Yao, J., Liu, W., Li, F., & Wang, C. (2022). Synergistic Piezo-Photocatalysis of BiOCl/NaNbO₃ Heterojunction Piezoelectric Composite for High-Efficient Organic Pollutant Degradation. *Nanomaterials*, 12(3), 353. <https://doi.org/10.3390/nano12030353>
- Li, L., Ma, Y., Chen, G., Wang, J., & Wang, C. (2022). Oxygen-vacancy-enhanced piezo-photocatalytic performance of AgNbO₃. *Scripta Materialia*, 206, 114234. <https://doi.org/10.1016/j.scriptamat.2021.114234>
- Li, Q., Wei, G., Yang, Y., Gao, L., Zhang, L., Li, Z., Huang, X., & Gan, J. (2021). Novel step-scheme red mud based Ag₃PO₄ heterojunction photocatalyst with enhanced photocatalytic performance and stability in photo-Fenton reaction. *Chemical Engineering Journal*, 424, 130537. <https://doi.org/10.1016/j.cej.2021.130537>
- Li, S., Liu, Z., Qu, Z., Piao, C., Liu, J., Xu, D., Li, X., Wang, J., & Song, Y. (2020). An all-solid-state Z-scheme NaNbO₃-Au-Sn₃O₄ photocatalyst for effective degradation of carbofuran under sunlight irradiation. *Journal of Photochemistry and Photobiology A: Chemistry*, 389, 112246. <https://doi.org/10.1016/j.jphotochem.2019.112246>
- Li, Y., Li, Z., & Gao, L. (2019). Construction of Z-scheme BiOI/g-C₃N₄ heterojunction with enhanced photocatalytic activity and stability under visible light. *Journal of Materials Science: Materials in Electronics* 2019 30:13, 30(13), 12769–12782. <https://doi.org/10.1007/S10854-019-01642-0>
- Li, Y., Zheng, X., Yang, J., Zhao, Z., & Cui, S. (2021). Enhanced photocatalytic degradation of 2,4,6-trichlorophenol and RhB with RhB-sensitized BiOClBr catalyst based on response surface methodology. *Journal of the Taiwan Institute of Chemical Engineers*, 119, 213–223. <https://doi.org/10.1016/j.jtice.2021.02.014>

- Liang, Q., Tong, Z., Guo, J., Wang, M., Yao, Q., & Zhou, H. (2021). Structural, magnetic and microwave properties of $Ba_{1-x}Nd_xFe_{12}O_{19}$. *Journal of Magnetism and Magnetic Materials*, 539, 168400. <https://doi.org/10.1016/j.jmmm.2021.168400>
- Liao, M., Su, L., Deng, Y., Xiong, S., Tang, R., Wu, Z., Ding, C., Yang, L., & Gong, D. (2021). Strategies to improve WO_3 -based photocatalysts for wastewater treatment: a review. *Journal of Materials Science*, 56(26), 14416–14447. <https://doi.org/10.1007/s10853-021-06202-8>
- Lim, J. J. Y., & Kay Lup, A. N. (2022). Heterostructural TiO_2/Ti_3C_2 MXene aerogel composite for photocatalytic degradation of palm oil mill effluent. *Environmental Science: Advances*, 1(4), 570–583. <https://doi.org/10.1039/D2VA00108J>
- Lin, E., Huang, R., Wu, J., Kang, Z., Ke, K., Qin, N., & Bao, D. (2021). Recyclable $CoFe_2O_4$ modified $BiOCl$ hierarchical microspheres utilizing photo, photothermal and mechanical energy for organic pollutant degradation. *Nano Energy*, 89, 106403. <https://doi.org/10.1016/j.nanoen.2021.106403>
- Liu, C., Liu, Y., Feng, C., Wang, P., Yu, L., Liu, D., Sun, S., & Wang, F. (2021). Distribution characteristics and potential risks of heavy metals and antimicrobial resistant *Escherichia coli* in dairy farm wastewater in Tai'an, China. *Chemosphere*, 262. <https://doi.org/10.1016/j.chemosphere.2020.127768>
- Liu, F., Wang, Y., Xu, D., Sun, F., Zhang, S., Wang, W., Li, X., Yu, W., Yu, H., & Dong, X. (2022). Full-spectrum-responsive 1D/2D $BiVO_4:Er^{3+},Yb^{3+}/BiOCl$ core-shell S-scheme heterostructure with boosted charge transport and redox capacity for the efficient removal of organic pollutants. *Ceramics International*. <https://doi.org/10.1016/j.ceramint.2022.12.212>
- Liu, H., Wang, C., & Wang, G. (2020). Photocatalytic Advanced Oxidation Processes for Water Treatment: Recent Advances and Perspective. *Chemistry – An Asian Journal*, 15(20), 3239–3253. <https://doi.org/10.1002/asia.202000895>
- Liu, H., Ye, M., Ren, Z., Lichtfouse, E., & Chen, Z. (2022). Towards synergistic combination of biochar/ultrasonic persulfate enhancing removal of natural humic acids from water. *Journal of Environmental Chemical Engineering*, 10(3), 107809. <https://doi.org/10.1016/j.jece.2022.107809>
- Liu, J., Wang, H., Chang, M.-J., Sun, M., He, Z.-W., Zhang, C.-M., Zhu, W.-Y., Chen, J.-L., Du, H.-L., Peng, L.-G., Luo, Z.-M., & Zhang, L. (2022). Magnetically separable $CoFe_2O_4/BiOCl$: Controllable synthesis, superior photocatalytic performance and mechanism towards decomposing RhB, NOR and Cr(VI) under visible light. *Colloids and Surfaces A: Physicochemical and Engineering Aspects*, 648, 129299. <https://doi.org/10.1016/j.colsurfa.2022.129299>
- Liu, Y., Xu, J., & Chen, M. (2021). Synthesis of direct Z-Scheme $Bi_3NbO_7/BiOCl$ photocatalysts with enhanced activity for CIP degradation and Cr(VI) reduction under visible light irradiation. *Separation and Purification Technology*, 276, 119255. <https://doi.org/10.1016/j.seppur.2021.119255>

- Lokman, N. A., Ithnin, A. M., Yahya, W. J., & Yuzir, M. A. (2021). A brief review on biochemical oxygen demand (BOD) treatment methods for palm oil mill effluents (POME). *Environmental Technology & Innovation*, 21, 101258. <https://doi.org/10.1016/j.eti.2020.101258>
- Long, Z., Li, Q., Wei, T., Zhang, G., & Ren, Z. (2020). Historical development and prospects of photocatalysts for pollutant removal in water. *Journal of Hazardous Materials*, 395, 122599. <https://doi.org/10.1016/j.jhazmat.2020.122599>
- Long, Z., Xian, G., Zhang, G., Zhang, T., & Li, X. (2020). BiOCl-Bi₁₂O₁₇Cl₂ nanocomposite with high visible-light photocatalytic activity prepared by an ultrasonic hydrothermal method for removing dye and pharmaceutical. *Chinese Journal of Catalysis*, 41(3), 464–473. [https://doi.org/10.1016/S1872-2067\(19\)63474-1](https://doi.org/10.1016/S1872-2067(19)63474-1)
- Lu, G., Song, B., Li, Z., Liang, H., & Zou, X. (2020). Photocatalytic degradation of naphthalene on CeVO₄ nanoparticles under visible light. *Chemical Engineering Journal*, 402, 125645. <https://doi.org/10.1016/j.cej.2020.125645>
- Lu, T., Gao, Y., Yang, Y., Ming, H., Huang, Z., Liu, G., Zheng, D. D., Zhang, J., & Hou, Y. (2021). Efficient degradation of tetracycline hydrochloride by photocatalytic ozonation over Bi₂WO₆. *Chemosphere*, 283. <https://doi.org/10.1016/j.chemosphere.2021.131256>
- Lu, Y., Feng, S., Shen, R., Xu, Y., Hao, Z., Yan, Y., Zheng, H., Yu, X., Gao, Q., Zhang, P., & Lin, S. (2019). Tunable Dynamic Black Phosphorus/Insulator/Si Heterojunction Direct-Current Generator Based on the Hot Electron Transport. *Research*, 2019. <https://doi.org/10.34133/2019/5832382>
- Ma, D., Yang, L., Sheng, Z., & Chen, Y. (2021). Photocatalytic degradation mechanism of benzene over ZnWO₄: Revealing the synergistic effects of Na-doping and oxygen vacancies. *Chemical Engineering Journal*, 405, 126538. <https://doi.org/10.1016/j.cej.2020.126538>
- Ma, W., Chen, L., Zhu, Y., Dai, J., Yan, Y., & Li, C. (2016). Facile synthesis of the magnetic BiOCl/ZnFe₂O₄ heterostructures with enhanced photocatalytic activity under visible-light irradiation. *Colloids and Surfaces A: Physicochemical and Engineering Aspects*, 508, 135–141. <https://doi.org/10.1016/j.colsurfa.2016.08.066>
- Mahmod, S. S., Arisht, S. N., Jahim, J. M., Takriff, M. S., Tan, J. P., Luthfi, A. A. I., & Abdul, P. M. (2022). Enhancement of biohydrogen production from palm oil mill effluent (POME): A review. *International Journal of Hydrogen Energy*, 47(96), 40637–40655. <https://doi.org/10.1016/j.ijhydene.2021.07.225>
- Mahmoodi, N. M., & Saffar-Dastgerdi, M. H. (2019). Zeolite nanoparticle as a superior adsorbent with high capacity: Synthesis, surface modification and pollutant adsorption ability from wastewater. *Microchemical Journal*, 145, 74–83. <https://doi.org/10.1016/j.microc.2018.10.018>

- Maleki, A., Moradi, F., Shahmoradi, B., Rezaee, R., & Lee, S.-M. (2020). The photocatalytic removal of diazinon from aqueous solutions using tungsten oxide doped zinc oxide nanoparticles immobilized on glass substrate. *Journal of Molecular Liquids*, *297*, 111918. <https://doi.org/10.1016/j.molliq.2019.111918>
- Mandizadeh, S., Salavati-Niasari, M., & Sadri, M. (2017). Hydrothermal synthesis, characterization and magnetic properties of BaFe₂O₄ nanostructure as a photocatalytic oxidative desulfurization of dibenzothiophene. *Separation and Purification Technology*, *175*, 399–405. <https://doi.org/10.1016/j.seppur.2016.11.071>
- Mansor, E. S., Geioushy, R. A., & Fouad, O. A. (2021). PANI/BiOCl nanocomposite induced efficient visible-light photocatalytic activity. *Journal of Materials Science: Materials in Electronics*, *32*(2), 1992–2000. <https://doi.org/10.1007/s10854-020-04966-4>
- Mao, L., Cai, X.-Y., & Zhu, M.-S. (2021). Hierarchically 1D CdS decorated on 2D perovskite-type La₂Ti₂O₇ nanosheet hybrids with enhanced photocatalytic performance. *Rare Metals*, *40*(5), 1067–1076. <https://doi.org/10.1007/s12598-020-01589-w>
- Martinson, J. N. v., & Walk, S. T. (2020). *Escherichia coli* Residency in the Gut of Healthy Human Adults. *EcoSal Plus*, *9*(1). <https://doi.org/10.1128/ecosalplus.ESP-0003-2020>
- Mecha, A. C., & Chollom, M. N. (2020). Photocatalytic ozonation of wastewater: a review. *Environmental Chemistry Letters*, *18*(5), 1491–1507. <https://doi.org/10.1007/s10311-020-01020-x>
- Miao, F., Wang, Q., Zhang, L.-C., & Shen, B. (2021). Magnetically separable Z-scheme FeSiB metallic glass/g-C₃N₄ heterojunction photocatalyst with high degradation efficiency at universal pH conditions. *Applied Surface Science*, *540*, 148401. <https://doi.org/10.1016/j.apsusc.2020.148401>
- Misrol, M. A., Wan Alwi, S. R., Lim, J. S., & Manan, Z. A. (2021). Integrated water and resource recovery network for combined domestic and industrial wastewater. In *Integrated and Hybrid Process Technology for Water and Wastewater Treatment* (pp. 35–59). Elsevier. <https://doi.org/10.1016/B978-0-12-823031-2.00020-3>
- Mohamad, N. A., Hamzah, S., Che Harun, M. H., Ali, A., Rasit, N., Awang, M., Rahman, W. R. W. Abd., Azmi, A. A. Abd. R., Abu Habib, A. A., Amri Zahid, M. S., Fahmi Mustofa, A. A., Latfi, S. A., Aripin, S. M., & Saad, R. (2021). Integration of copperas and calcium hydroxide as a chemical coagulant and coagulant aid for efficient treatment of palm oil mill effluent. *Chemosphere*, *281*, 130873. <https://doi.org/10.1016/j.chemosphere.2021.130873>
- Mohammed, N. A., Alwared, A. I., & Salman, M. S. (2020). Photocatalytic Degradation of Reactive Yellow Dye in Wastewater using H₂O₂/TiO₂/UV Technique. *Iraqi Journal of Chemical and Petroleum Engineering*, *21*(1), 15–21. <https://doi.org/10.31699/IJCPE.2020.1.3>

- Mohan, H., Ramalingam, V., Adithan, A., Natesan, K., Seralathan, K.-K., & Shin, T. (2021). Highly efficient visible light driven photocatalytic activity of zinc/ferrite: Carbamazepine degradation, mechanism and toxicity assessment. *Journal of Hazardous Materials*, *416*, 126209. <https://doi.org/10.1016/j.jhazmat.2021.126209>
- Mohsen Padervand, Mojtaba Mazloum, Alireza Bargahi, & Naser Arsalani. (2021). CQDs/BiOCl Photocatalysts for the Efficient Treatment of Congo Red Aqueous Solution under Visible Light. *Journal of Nanostructures*, *11*(4), 790–801.
- Monga, D., & Basu, S. (2021). Single-crystalline 2D BiOCl nanorods decorated with 2D MoS₂ nanosheets for visible light-driven photocatalytic detoxification of organic and inorganic pollutants. *FlatChem*, *28*, 100267. <https://doi.org/10.1016/j.flatc.2021.100267>
- Moradi, M., Vasseghian, Y., Khataee, A., Harati, M., & Arfaeina, H. (2021). Ultrasound-assisted synthesis of FeTiO₃/GO nanocomposite for photocatalytic degradation of phenol under visible light irradiation. *Separation and Purification Technology*, *261*, 118274. <https://doi.org/10.1016/j.seppur.2020.118274>
- Mustafa, F. S., & Oladipo, A. A. (2021). Photocatalytic degradation of metronidazole and bacteria disinfection activity of Ag-doped Ni_{0.5}Zn_{0.5}Fe₂O₄. *Journal of Water Process Engineering*, *42*, 102132. <https://doi.org/10.1016/j.jwpe.2021.102132>
- Nahar, S., Hasan, M. R., Kadhum, A. A. H., Hasan, H. A., & Zain, M. F. M. (2019). Photocatalytic degradation of organic pollutants over visible light active plasmonic Ag nanoparticle loaded Ag₂SO₃ photocatalysts. *Journal of Photochemistry and Photobiology A: Chemistry*, *375*, 191–200. <https://doi.org/10.1016/j.jphotochem.2019.02.025>
- Naidua, T., Qadir, D., Nasir, R., Mannan, H. A., Mukhtar, H., Maqsood, K., Ali, A., & Abdulrahman, A. (2021). Utilization of moringa oleifera and nanofiltration membrane to treat palm oil mill effluent (POME). *Materialwissenschaft Und Werkstofftechnik*, *52*(3), 346–356. <https://doi.org/10.1002/mawe.202000084>
- Narang, S. B., & Pubby, K. (2021). Nickel Spinel Ferrites: A review. *Journal of Magnetism and Magnetic Materials*, *519*, 167163. <https://doi.org/10.1016/j.jmmm.2020.167163>
- Nasrollahzadeh, M., Atarod, M., Sajjadi, M., Sajadi, S. M., & Issaabadi, Z. (2019). *Plant-Mediated Green Synthesis of Nanostructures: Mechanisms, Characterization, and Applications* (pp. 199–322). <https://doi.org/10.1016/B978-0-12-813586-0.00006-7>
- Nasrullah, M., Singh, L., Krishnan, S., Sakinah, M., Mahapatra, D. M., & Zularisam, A. W. (2020). Electrocoagulation treatment of raw palm oil mill effluent: Effect of operating parameters on floc growth and structure. *Journal of Water Process Engineering*, *33*, 101114. <https://doi.org/10.1016/j.jwpe.2019.101114>

- Nawaz, R., Haider, S., Ullah, H., Akhtar, M. S., Khan, S., Junaid, M., & Khan, N. (2022a). Optimized remediation of treated agro-industrial effluent using visible light-responsive core-shell structured black TiO₂ photocatalyst. *Journal of Environmental Chemical Engineering*, 10(1), 106968. <https://doi.org/10.1016/j.jece.2021.106968>
- Neelgund, G. M., & Oki, A. (2020). ZnO conjugated graphene: An efficient sunlight driven photocatalyst for degradation of organic dyes. *Materials Research Bulletin*, 129, 110911. <https://doi.org/10.1016/j.materresbull.2020.110911>
- Nekooie, R., Shamspur, T., & Mostafavi, A. (2021). Novel CuO/TiO₂/PANI nanocomposite: Preparation and photocatalytic investigation for chlorpyrifos degradation in water under visible light irradiation. *Journal of Photochemistry and Photobiology A: Chemistry*, 407, 113038. <https://doi.org/10.1016/j.jphotochem.2020.113038>
- Nemiwal, M., Zhang, T. C., & Kumar, D. (2021). Recent progress in g-C₃N₄, TiO₂ and ZnO based photocatalysts for dye degradation: Strategies to improve photocatalytic activity. *Science of The Total Environment*, 767, 144896. <https://doi.org/10.1016/j.scitotenv.2020.144896>
- Ng, K. H. (2021). Adoption of TiO₂-photocatalysis for palm oil mill effluent (POME) treatment: Strengths, weaknesses, opportunities, threats (SWOT) and its practicality against traditional treatment in Malaysia. *Chemosphere*, 270, 129378. <https://doi.org/10.1016/j.chemosphere.2020.129378>
- Ng, K. H., & Cheng, C. K. (2017). Photocatalytic degradation of palm oil mill effluent over ultraviolet-responsive titania: Successive assessments of significance factors and process optimization. *Journal of Cleaner Production*, 142, 2073–2083. <https://doi.org/10.1016/j.jclepro.2016.11.077>
- Ng, K. H., Cheng, Y. W., Khan, M. R., & Cheng, C. K. (2016). Optimization of photocatalytic degradation of palm oil mill effluent in UV/ZnO system based on response surface methodology. *Journal of Environmental Management*, 184, 487–493. <https://doi.org/10.1016/j.jenvman.2016.10.034>
- Ng, K. H., Yuan, L. S., Cheng, C. K., Chen, K., & Fang, C. (2019). TiO₂ and ZnO photocatalytic treatment of palm oil mill effluent (POME) and feasibility of renewable energy generation: A short review. *Journal of Cleaner Production*, 233, 209–225. <https://doi.org/10.1016/j.jclepro.2019.06.044>
- Niu, J., Albero, J., Atienzar, P., & García, H. (2020). Porous Single-Crystal-Based Inorganic Semiconductor Photocatalysts for Energy Production and Environmental Remediation: Preparation, Modification, and Applications. *Advanced Functional Materials*, 30(15), 1908984. <https://doi.org/10.1002/adfm.201908984>
- Niu, S., Zhang, R., & Guo, C. (2020). Oxygen vacancy induced superior visible-light-driven photo-catalytic performance in the BiOCl homojunction. *Materials Chemistry Frontiers*, 4(8), 2314–2324. <https://doi.org/10.1039/D0QM00187B>

- Oda, A. M., Naji, H. K., Lafta, A. J., Salih, A., Ahmed, L., Jawad, H., & Falah, K. (2019). Congo red Dye Removal from Simulated Textile Wastewaters over a neat and silver Doped Zinc Oxide Nanoparticles. A Kinetics Study. *Research Journal of Pharmacy and Technology*, 12(6), 2669. <https://doi.org/10.5958/0974-360X.2019.00446.3>
- Okocha, R. C., Olatoye, I. O., & Adedeji, O. B. (2018). Food safety impacts of antimicrobial use and their residues in aquaculture. In *Public Health Reviews* (Vol. 39, Issue 1). BioMed Central Ltd. <https://doi.org/10.1186/s40985-018-0099-2>
- Owodunni, A. A., & Ismail, S. (2021). Revolutionary technique for sustainable plant-based green coagulants in industrial wastewater treatment—A review. *Journal of Water Process Engineering*, 42, 102096. <https://doi.org/10.1016/j.jwpe.2021.102096>
- Patial, S., Kumar, A., Raizada, P., Le, Q. van, Nguyen, V.-H., Selvasembian, R., Singh, P., Thakur, S., & Hussain, C. M. (2022). Potential of graphene based photocatalyst for antiviral activity with emphasis on COVID-19: A review. *Journal of Environmental Chemical Engineering*, 10(3), 107527. <https://doi.org/10.1016/j.jece.2022.107527>
- Petala, A., Arvaniti, O. S., Travlou, G., Mantzavinos, D., & Frontistis, Z. (2021). Solar light induced photocatalytic removal of sulfamethoxazole from water and wastewater using BiOCl photocatalyst. *Journal of Environmental Science and Health, Part A*, 56(9), 963–972. <https://doi.org/10.1080/10934529.2021.1948271>
- Pham, P. T. D., Bui, P. Q. T., Nong, L. X., Nguyen, V. H., Bach, L. G., Vu, H. T., Nguyen, H. T., & Nguyen, T. D. (2019). Synthesis of the BIVO₄ nanoparticle as an efficient photocatalyst to activate hydrogen peroxide for the degradation of methylene blue under visible light irradiation. *IOP Conference Series: Materials Science and Engineering*, 479, 012036. <https://doi.org/10.1088/1757-899X/479/1/012036>
- Phang, Y.-K., Aminuzzaman, M., Akhtaruzzaman, Md., Muhammad, G., Ogawa, S., Watanabe, A., & Tey, L.-H. (2021a). Green Synthesis and Characterization of CuO Nanoparticles Derived from Papaya Peel Extract for the Photocatalytic Degradation of Palm Oil Mill Effluent (POME). *Sustainability*, 13(2), 796. <https://doi.org/10.3390/su13020796>
- Phang, Y.-K., Aminuzzaman, M., Akhtaruzzaman, Md., Muhammad, G., Ogawa, S., Watanabe, A., & Tey, L.-H. (2021b). Green Synthesis and Characterization of CuO Nanoparticles Derived from Papaya Peel Extract for the Photocatalytic Degradation of Palm Oil Mill Effluent (POME). *Sustainability*, 13(2), 796. <https://doi.org/10.3390/su13020796>
- Phuruangrat, A., Kuntalue, B., Thongtem, S., & Thongtem, T. (2021). Characterization of Black-Light-Driven CeVO₄ Photocatalysts Synthesized by Sol-Gel Method Using Citric Acid as Complexing Agent with Subsequent High

Temperature Calcination. *Russian Journal of Inorganic Chemistry*, 66(3), 332–339. <https://doi.org/10.1134/S0036023621030128>

- Prabhu, S., Megala, S., Harish, S., Navaneethan, M., Maadeswaran, P., Sohila, S., & Ramesh, R. (2019). Enhanced photocatalytic activities of ZnO dumbbell/reduced graphene oxide nanocomposites for degradation of organic pollutants via efficient charge separation pathway. *Applied Surface Science*, 487, 1279–1288. <https://doi.org/10.1016/j.apsusc.2019.05.086>
- Puri, S., & Verma, A. (2022). Color removal from secondary treated pulp & paper industry effluent using waste driven Fe–TiO₂ composite. *Chemosphere*, 303, 135143. <https://doi.org/10.1016/j.chemosphere.2022.135143>
- Qi, S., Liu, X., Ma, N., & Xu, H. (2021). Construction and photocatalytic properties of WS₂/MoS₂/BiOCl heterojunction. *Chemical Physics Letters*, 763, 138203. <https://doi.org/10.1016/j.cplett.2020.138203>
- Qin, Q., Guo, R., Lin, S., Jiang, S., Lan, J., Lai, X., Cui, C., Xiao, H., & Zhang, Y. (2019). Waste cotton fiber/Bi₂WO₆ composite film for dye removal. *Cellulose*, 26(6), 3909–3922. <https://doi.org/10.1007/s10570-019-02345-9>
- Qureshi, F., Nawaz, M., Rehman, S., Almofty, S. A., Shahzad, S., Nissapatorn, V., & Taha, M. (2020). Synthesis and characterization of cadmium-bismuth microspheres for the catalytic and photocatalytic degradation of organic pollutants, with antibacterial, antioxidant and cytotoxicity assay. *Journal of Photochemistry and Photobiology B: Biology*, 202, 111723. <https://doi.org/10.1016/j.jphotobiol.2019.111723>
- Rachmadona, N., Quayson, E., Amoah, J., Alfaro-Sayes, D. A., Hama, S., Aznury, M., Kondo, A., & Ogino, C. (2021). Utilizing palm oil mill effluent (POME) for the immobilization of *Aspergillus oryzae* whole-cell lipase strains for biodiesel synthesis. *Biofuels, Bioproducts and Biorefining*, 15(3), 804–814. <https://doi.org/10.1002/bbb.2202>
- Rahman, M. E., bin Halmi, M. I. E., bin Abd Samad, M. Y., Uddin, M. K., Mahmud, K., Abd Shukor, M. Y., Sheikh Abdullah, S. R., & Shamsuzzaman, S. M. (2020). Design, Operation and Optimization of Constructed Wetland for Removal of Pollutant. *International Journal of Environmental Research and Public Health*, 17(22), 8339. <https://doi.org/10.3390/ijerph17228339>
- Rahman, S., Nawaz, R., Khan, J. A., Ullah, H., Irfan, M., Glowacz, A., Lyp-Wronska, K., Wzorek, L., Asif Khan, M. K., Jalalah, M., Alsaiani, M. A., & Almawgani, A. H. (2021). Synthesis and Characterization of Carbon and Carbon-Nitrogen Doped Black TiO₂ Nanomaterials and Their Application in Sonophotocatalytic Remediation of Treated Agro-Industrial Wastewater. *Materials*, 14(20), 6175. <https://doi.org/10.3390/ma14206175>
- Rahman, S., Nawaz, R., Khan, J. A., Ullah, H., Irfan, M., Glowacz, A., Lyp-Wronska, K., Wzorek, L., Khan, M. K. A., Jalalah, M., Alsaiani, M. A., & Almawgani, A. H. (2021). Synthesis and characterization of carbon and carbon-nitrogen doped black TiO₂ nanomaterials and their application in sonophotocatalytic

- remediation of treated agro-industrial wastewater. *Materials*, 14(20). <https://doi.org/10.3390/ma14206175>
- Rashid, J., Karim, S., Kumar, R., Barakat, M. A., Akram, B., Hussain, N., Bin, H. bin, & Xu, M. (2020). A facile synthesis of bismuth oxychloride-graphene oxide composite for visible light photocatalysis of aqueous diclofenac sodium. *Scientific Reports*, 10(1), 14191. <https://doi.org/10.1038/s41598-020-71139-y>
- Razali, N. A. M., Salleh, W. N. W., Aziz, F., Jye, L. W., Yusof, N., Jaafar, J., & Ismail, A. F. (2022). Influence of g-C₃N₄ and PANI onto WO₃ photocatalyst on the photocatalytic degradation of POME. *Materials Today: Proceedings*, 65, 3054–3059. <https://doi.org/10.1016/j.matpr.2022.04.118>
- Rosu, M.-C., Coros, M., Pogacean, F., Magerusan, L., Socaci, C., Turza, A., & Pruneanu, S. (2017). Azo dyes degradation using TiO₂-Pt/graphene oxide and TiO₂-Pt/reduced graphene oxide photocatalysts under UV and natural sunlight irradiation. *Solid State Sciences*, 70, 13–20. <https://doi.org/10.1016/j.solidstatedsciences.2017.05.013>
- Salari, H., & Zahiri, Z. (2022). Design of S-scheme 3D nickel molybdate/AgBr nanocomposites: Tuning of the electronic band structure towards efficient interfacial photoinduced charge separation and remarkable photocatalytic activity. *Journal of Photochemistry and Photobiology A: Chemistry*, 426, 113751. <https://doi.org/10.1016/j.jphotochem.2021.113751>
- Sansenya, T., Masri, N., Chankhanittha, T., Senasu, T., Piriyanon, J., Mukdasai, S., & Nanan, S. (2022). Hydrothermal synthesis of ZnO photocatalyst for detoxification of anionic azo dyes and antibiotic. *Journal of Physics and Chemistry of Solids*, 160, 110353. <https://doi.org/10.1016/j.jpcs.2021.110353>
- Sayadi, M. H., Ahmadpour, N., & Homaeigohar, S. (2021). Photocatalytic and Antibacterial Properties of Ag-CuFe₂O₄@WO₃ Magnetic Nanocomposite. *Nanomaterials*, 11(2), 298. <https://doi.org/10.3390/nano11020298>
- Shahid-ul-Islam, Butola, B. S., & Verma, D. (2019). Facile synthesis of chitosan-silver nanoparticles onto linen for antibacterial activity and free-radical scavenging textiles. *International Journal of Biological Macromolecules*, 133, 1134–1141. <https://doi.org/10.1016/j.ijbiomac.2019.04.186>
- Shanmugam, V., Muppudathi, A. L., Jayavel, S., & Jeyaperumal, K. S. (2020). Construction of high efficient g-C₃N₄ nanosheets combined with Bi₂MoO₆-Ag photocatalysts for visible-light-driven photocatalytic activity and inactivation of bacteria. *Arabian Journal of Chemistry*, 13(1), 2439–2455. <https://doi.org/10.1016/j.arabjc.2018.05.009>
- Shanmugam, V., Jeyaperumal, K.S., Mariappan, P., Muppudathi, A.L., (2020). Fabrication of novel g-C₃N₄ based MoS₂ and Bi₂O₃ nanorod embedded ternary nanocomposites for superior photocatalytic performance and destruction of bacteria. *New J. Chem.* 44, 13182-13194. <http://doi:10.1039/d0nj02101f>

- Shariah Ghazali, S., Jusoh, R., & Haslinda Shariffuddin, J. (2019). Parameter Affecting Photocatalytic Degradation of POME using LaCa as Photocatalyst. *Materials Today: Proceedings*, 19, 1173–1182. <https://doi.org/10.1016/j.matpr.2019.11.120>
- Sharma, K., Raizada, P., Hasija, V., Singh, P., Bajpai, A., Nguyen, V.-H., Rangabhashiyam, S., Kumar, P., Nadda, A. K., Kim, S. Y., Varma, R. S., Le, T. T. N., & Le, Q. van. (2021). ZnS-based quantum dots as photocatalysts for water purification. *Journal of Water Process Engineering*, 43, 102217. <https://doi.org/10.1016/j.jwpe.2021.102217>
- Shi, J.-L., & Lang, X. (2020). Assembling polydopamine on TiO₂ for visible light photocatalytic selective oxidation of sulfides with aerial O₂. *Chemical Engineering Journal*, 392, 123632. <https://doi.org/10.1016/j.cej.2019.123632>
- Sin, J. C., Lim, C. A., Lam, S. M., Zeng, H., Lin, H., Li, H., & Mohamed, A. R. (2020). Fabrication of novel visible light-driven Nd-doped BiOBr nanosheets with enhanced photocatalytic performance for palm oil mill effluent degradation and Escherichia coli inactivation. *Journal of Physics and Chemistry of Solids*, 140, 109382. <https://doi.org/10.1016/J.JPCS.2020.109382>
- Sin, J.-C., Lam, S.-M., Zeng, H., Lin, H., Li, H., Kugan Kumaresan, A., Mohamed, A. R., & Lim, J.-W. (2020). Z-scheme heterojunction nanocomposite fabricated by decorating magnetic MnFe₂O₄ nanoparticles on BiOBr nanosheets for enhanced visible light photocatalytic degradation of 2,4-dichlorophenoxyacetic acid and Rhodamine B. *Separation and Purification Technology*, 250, 117186. <https://doi.org/10.1016/j.seppur.2020.117186>
- Sin, J.-C., Lam, S.-M., Zeng, H., Lin, H., Li, H., & Mohamed, A. R. (2020). Constructing magnetic separable BiOBr/MnFe₂O₄ as efficient Z-scheme nanocomposite for visible light-driven degradation of palm oil mill effluent and inactivation of bacteria. *Materials Letters*, 275, 128112. <https://doi.org/10.1016/j.matlet.2020.128112>
- Singh, A., & Mishra, B. K. (2021). *Solar Light-Driven Photocatalysis Using BaFe₂O₄/rGO for Chlorhexidine Digluconate Contaminated Water: Comparison With Artificial UV and Visible Light-Mediated Photocatalysis*. <https://doi.org/10.21203/rs.3.rs-386420/v1>
- Singh, A., & Mishra, B. K. (2022). Solar light-driven photocatalysis using BaFe₂O₄/rGO for chlorhexidine digluconate-contaminated water: comparison with artificial UV and visible light-mediated photocatalysis. *Environmental Science and Pollution Research*, 29(20), 30739–30753. <https://doi.org/10.1007/s11356-021-17689-8>
- Singh, H., Kumar, A., Thakur, A., Kumar, P., Nguyen, V.-H., Vo, D.-V. N., Sharma, A., & Kumar, D. (2020). One-Pot Synthesis of Magnetite-ZnO Nanocomposite and Its Photocatalytic Activity. *Topics in Catalysis*, 63(11–14), 1097–1108. <https://doi.org/10.1007/s11244-020-01278-z>

- Smazna, D., Shree, S., Polonskyi, O., Lamaka, S., Baum, M., Zheludkevich, M., Faupel, F., Adelung, R., & Mishra, Y. K. (2019). Mutual interplay of ZnO micro- and nanowires and methylene blue during cyclic photocatalysis process. *Journal of Environmental Chemical Engineering*, 7(2), 103016. <https://doi.org/10.1016/j.jece.2019.103016>
- Soo, P. L., Bashir, M. J. K., & Wong, L.-P. (2022). Recent advancements in the treatment of palm oil mill effluent (POME) using anaerobic biofilm reactors: Challenges and future perspectives. *Journal of Environmental Management*, 320, 115750. <https://doi.org/10.1016/j.jenvman.2022.115750>
- Su, C., Cheng, M., Tian, F., Chen, F., & Chen, R. (2022). Anti-oil-fouling Au/BiOCl coating for visible light-driven photocatalytic inactivation of bacteria. *Journal of Colloid and Interface Science*, 628, 955–967. <https://doi.org/10.1016/j.jcis.2022.08.087>
- Subramanian, S., Ganapathy, S., Dharmalingam, S., & Jayavel, R. (2023). Enhanced photocatalytic activities of GO nanosheets-decorated NiTiO₃ NFs composites for the environmental remediation of industrial dye. *Bulletin of Materials Science*, 46(1), 19. <https://doi.org/10.1007/s12034-022-02880-5>
- Sun, M., Su, Y., Yang, W., Zhang, L., Hu, J., & Lv, Y. (2019). Organosiloxane and Polyhedral Oligomeric Silsesquioxanes Compounds as Chemiluminescent Molecular Probes for Direct Monitoring Hydroxyl Radicals. *Analytical Chemistry*, 91(14), 8926–8932. <https://doi.org/10.1021/acs.analchem.9b00637>
- Surendra, B. S., Shashi Shekhar, T. R., Veerabhadraswamy, M., Nagaswarupa, H. P., Prashantha, S. C., Geethanjali, G. C., & Likitha, C. (2020). Probe sonication synthesis of ZnFe₂O₄ NPs for the photocatalytic degradation of dyes and effect of treated wastewater on growth of plants. *Chemical Physics Letters*, 745, 137286. <https://doi.org/10.1016/j.cplett.2020.137286>
- Syahin, M. S., Karim Ghani, W. A. A. B., & Loh, S. K. (2020). DECOLOURISATION OF PALM OIL MILL EFFLUENT (POME) TREATMENT TECHNOLOGIES: A REVIEW. *Journal of Oil Palm Research*. <https://doi.org/10.21894/jopr.2020.0008>
- Tamaddon, F., Mosslemin, M. H., Asadipour, A., Gharaghani, M. A., & Nasiri, A. (2020). Microwave-assisted preparation of ZnFe₂O₄@methyl cellulose as a new nano-biomagnetic photocatalyst for photodegradation of metronidazole. *International Journal of Biological Macromolecules*, 154, 1036–1049. <https://doi.org/10.1016/j.ijbiomac.2020.03.069>
- Tan Ai Wei, I., Nur Syakina Jamali, & Winnie Huang Tien Ting. (2019). Phytoremediation of Palm Oil Mill Effluent (POME) Using Eichhornia crassipes. *Journal of Applied Science & Process Engineering*, 6(1), 340–354. <https://doi.org/10.33736/jaspe.1349.2019>
- Tan, J. B., Lutpi, N. A., Wong, Y. S., Rahmat, N. R., & Siripatana, C. (2021). Study on the effect of headspace on biohydrogen production using palm oil mill effluent (POME) via immobilized and suspended growth. *IOP Conference*

Series: Earth and Environmental Science, 920(1), 012037.
<https://doi.org/10.1088/1755-1315/920/1/012037>

- Tan, Y. D., & Lim, J. S. (2019). Feasibility of palm oil mill effluent elimination towards sustainable Malaysian palm oil industry. *Renewable and Sustainable Energy Reviews*, 111, 507–522. <https://doi.org/10.1016/j.rser.2019.05.043>
- Tang, X., Liu, H., Yang, C., Jin, X., Zhong, J., & Li, J. (2020). In-situ fabrication of Z-scheme CdS/BiOCl heterojunctions with largely improved photocatalytic performance. *Colloids and Surfaces A: Physicochemical and Engineering Aspects*, 599, 124880. <https://doi.org/10.1016/j.colsurfa.2020.124880>
- Teow, Y. H., Chong, M. T., Ho, K. C., & Mohammad, A. W. (2021). Comparative environmental impact evaluation using life cycle assessment approach: a case study of integrated membrane-filtration system for the treatment of aerobically-digested palm oil mill effluent. *Sustainable Environment Research*, 31(1), 15. <https://doi.org/10.1186/s42834-021-00089-5>
- Ungureanu, N., Vlăduț, V., & Voicu, G. (2020). Water Scarcity and Wastewater Reuse in Crop Irrigation. *Sustainability*, 12(21), 9055. <https://doi.org/10.3390/su12219055>
- Vaiano, V., Sacco, O., & Sannino, D. (2019). Electric energy saving in photocatalytic removal of crystal violet dye through the simultaneous use of long-persistent blue phosphors, nitrogen-doped TiO₂ and UV-light emitting diodes. *Journal of Cleaner Production*, 210, 1015–1021. <https://doi.org/10.1016/j.jclepro.2018.11.017>
- Vignesh, S., Muppudathi, A. L., & Sundar, J. K. (2018). Multifunctional performance of gC₃N₄-BiFeO₃-Cu₂O hybrid nanocomposites for magnetic separable photocatalytic and antibacterial activity. *Journal of Materials Science: Materials in Electronics*, 29(13), 10784–10801. <https://doi.org/10.1007/s10854-018-9144-7>
- Vítězová, M., Kohoutová, A., Vítěz, T., Hanišáková, N., & Kushkevych, I. (2020). Methanogenic Microorganisms in Industrial Wastewater Anaerobic Treatment. *Processes*, 8(12), 1546. <https://doi.org/10.3390/pr8121546>
- V.N. Nikolic. (2020). Magnetic Nanomaterials for Electrocatalysis. In Inamuddin, B. Rajender, & Abdullah M. Asiri (Eds.), *Magnetochemistry: Materials and Applications* (Vol. 66, pp. 34–86). Materials Research Forum LLC. <https://doi.org/10.21741/9781644900611-2>
- Wahyono, Y., Hadiyanto, H., Budihardjo, M. A., & Adiansyah, J. S. (2020). Assessing the Environmental Performance of Palm Oil Biodiesel Production in Indonesia: A Life Cycle Assessment Approach. *Energies*, 13(12), 3248. <https://doi.org/10.3390/en13123248>
- Wang, M., Lu, G., Jiang, R., Dang, T., & Liu, J. (2022). Degradation and detoxification of broad-spectrum antibiotics by small molecular intercalated

- BiOCl under visible light. *Journal of Colloid and Interface Science*, 622, 995–1007. <https://doi.org/10.1016/j.jcis.2022.04.179>
- Wang, Y., Yang, H., Sun, X., Zhang, H., & Xian, T. (2020). Preparation and photocatalytic application of ternary n-BaTiO₃/Ag/p-AgBr heterostructured photocatalysts for dye degradation. *Materials Research Bulletin*, 124, 110754. <https://doi.org/10.1016/j.materresbull.2019.110754>
- Wei, X., Li, K., Zhang, X., Tong, Q., Ji, J., Cai, Y., Gao, B., Zou, W., & Dong, L. (2022). CeO₂ nanosheets with anion-induced oxygen vacancies for promoting photocatalytic toluene mineralization: Toluene adsorption and reactive oxygen species. *Applied Catalysis B: Environmental*, 317, 121694. <https://doi.org/10.1016/j.apcatb.2022.121694>
- Wong, K.-A., Lam, S.-M., & Sin, J.-C. (2019a). Wet chemically synthesized ZnO structures for photodegradation of pre-treated palm oil mill effluent and antibacterial activity. *Ceramics International*, 45(2), 1868–1880. <https://doi.org/10.1016/j.ceramint.2018.10.078>
- Wong, K.-A., Lam, S.-M., & Sin, J.-C. (2019b). Shape-Controlled Fabrication of ZnO Architectures for Palm Oil Mill Effluent Degradation. *Journal of Nanoscience and Nanotechnology*, 19(8), 5271–5278. <https://doi.org/10.1166/jnn.2019.16816>
- Wu, L., Jiang, G., Wang, X., Wang, Y., Zhou, Y., & Wu, Z. (2022). Amorphous iron oxides anchored on BiOCl nanoplates as robust catalysts for high-performance photo-Fenton oxidation. *Journal of Colloid and Interface Science*, 622, 62–74. <https://doi.org/10.1016/j.jcis.2022.04.092>
- Xiang, W., Yuan, J., Wu, Y., Luo, H., Xiao, C., Zhong, N., Zhao, M., Zhong, D., & He, Y. (2022). Working principle and application of photocatalytic optical fibers for the degradation and conversion of gaseous pollutants. *Chinese Chemical Letters*, 33(8), 3632–3640. <https://doi.org/10.1016/j.ccllet.2021.11.074>
- Xiao, J., Xie, Y., Rabeah, J., Brückner, A., & Cao, H. (2020). Visible-Light Photocatalytic Ozonation Using Graphitic C₃N₄ Catalysts: A Hydroxyl Radical Manufacturer for Wastewater Treatment. *Accounts of Chemical Research*, 53(5), 1024–1033. <https://doi.org/10.1021/acs.accounts.9b00624>
- Xie, R., Fang, K., Liu, Y., Chen, W., Fan, J., Wang, X., Ren, Y., & Song, Y. (2020). Z-scheme In₂O₃/WO₃ heterogeneous photocatalysts with enhanced visible-light-driven photocatalytic activity toward degradation of organic dyes. *Journal of Materials Science*, 55(26), 11919–11937. <https://doi.org/10.1007/s10853-020-04863-5>
- Xie, X., Li, S., Qi, K., & Wang, Z. (2021). Photoinduced synthesis of green photocatalyst Fe₃O₄/BiOBr/CQDs derived from corncob biomass for carbamazepine degradation: The role of selectively more CQDs decoration and Z-scheme structure. *Chemical Engineering Journal*, 420, 129705. <https://doi.org/10.1016/j.cej.2021.129705>

- Xu, D., & Ma, H. (2021). Degradation of rhodamine B in water by ultrasound-assisted TiO₂ photocatalysis. *Journal of Cleaner Production*, 313, 127758. <https://doi.org/10.1016/j.jclepro.2021.127758>
- Xu, J., Zhang, M., Li, X., & Chen, M. (2022). Efficient photocatalytic performance of direct Z-scheme photocatalyst Bi₃TaO₇/Mn_{0.5}Cd_{0.5}S for levofloxacin degradation under visible light irradiation. *Journal of Environmental Chemical Engineering*, 10(3), 107484. <https://doi.org/10.1016/j.jece.2022.107484>
- Xu, Y., He, X., Zhong, H., Singh, D. J., Zhang, L., & Wang, R. (2019). Solid salt confinement effect: An effective strategy to fabricate high crystalline polymer carbon nitride for enhanced photocatalytic hydrogen evolution. *Applied Catalysis B: Environmental*, 246, 349–355. <https://doi.org/10.1016/j.apcatb.2019.01.069>
- Yan, H., & Yang, H. (2011). TiO₂-g-C₃N₄ composite materials for photocatalytic H₂ evolution under visible light irradiation. *Journal of Alloys and Compounds*, 509(4), L26–L29. <https://doi.org/10.1016/j.jallcom.2010.09.201>
- Yan, P., Mo, Z., Dong, J., Chen, F., Qian, J., Xia, J., Xu, L., Zhang, J., & Li, H. (2020). Construction of Mn valence-engineered MnO₂/BiOCl heterojunction coupled with carriers-trapping effect for enhanced photoelectrochemical lincomycin aptasensor. *Sensors and Actuators B: Chemical*, 320, 128415. <https://doi.org/10.1016/j.snb.2020.128415>
- Yan, Z., Dai, Z., Zheng, W., Lei, Z., Qiu, J., Kuang, W., Huang, W., & Feng, C. (2021). Facile ammonium oxidation to nitrogen gas in acid wastewater by in situ photogenerated chlorine radicals. *Water Research*, 205, 117678. <https://doi.org/10.1016/j.watres.2021.117678>
- Yang, Y., Liu, B., Xu, J., Wang, Q., Wang, X., Lv, G., & Zhou, J. (2022). The Synthesis of h-BN-Modified Z-Scheme WO₃/g-C₃N₄ Heterojunctions for Enhancing Visible Light Photocatalytic Degradation of Tetracycline Pollutants. *ACS Omega*, 7(7), 6035–6045. <https://doi.org/10.1021/acsomega.1c06377>
- Yin, J., Cogan, N. M. B., Burke, R., Hou, Z., Sowers, K. L., & Krauss, T. D. (2019). Size dependence of photocatalytic hydrogen generation for CdTe quantum dots. *The Journal of Chemical Physics*, 151(17), 174707. <https://doi.org/10.1063/1.5125000>
- Yosefi, L., & Haghghi, M. (2019). Sequential precipitation design of p-BiOCl-p-Mn₃O₄ binary semiconductor nanoheterojunction with enhanced photoactivity for acid orange 7 removal from water. *Ceramics International*, 45(7), 8248–8257. <https://doi.org/10.1016/j.ceramint.2019.01.130>
- Yuan, X., Yang, J., Yao, Y., Shen, H., Meng, Y., Xie, B., Ni, Z., & Xia, S. (2022). Preparation, characterization and photodegradation mechanism of 0D/2D Cu₂O/BiOCl S-scheme heterojunction for efficient photodegradation of tetracycline. *Separation and Purification Technology*, 291, 120965. <https://doi.org/10.1016/j.seppur.2022.120965>

- Zahra, H., Kurniawan, I., & Hakim, A. (2020). The Efficiency of Melanoidin Based-Waste Degradation with Different Biological Methods. *Current Biochemistry*, 7(2), 52–60. <https://doi.org/10.29244/cb.7.2.2>
- Zainuri, N. Z., Hairom, N. H. H., Sidik, D. A. B., Desa, A. L., Misdan, N., Yusof, N., & Mohammad, A. W. (2018). Palm oil mill secondary effluent (POMSE) treatment via photocatalysis process in presence of ZnO-PEG nanoparticles. *Journal of Water Process Engineering*, 26, 10–16. <https://doi.org/10.1016/j.jwpe.2018.08.009>
- Zangeneh, H., Zinatizadeh, A. A., Feyzi, M., Zinadini, S., & Bahnemann, D. W. (2018). Photomineralization of recalcitrant wastewaters by a novel magnetically recyclable boron doped-TiO₂-SiO₂ cobalt ferrite nanocomposite as a visible-driven heterogeneous photocatalyst. *Journal of Environmental Chemical Engineering*, 6(5), 6370–6381. <https://doi.org/10.1016/j.jece.2018.10.001>
- Zangeneh, H., Zinatizadeh, A. A., Zinadini, S., Feyzi, M., Rafiee, E., & Bahnemann, D. W. (2019). A novel L-Histidine (C, N) codoped-TiO₂-CdS nanocomposite for efficient visible photo-degradation of recalcitrant compounds from wastewater. *Journal of Hazardous Materials*, 369, 384–397. <https://doi.org/10.1016/j.jhazmat.2019.02.049>
- Zhang, D., Tan, G., Wang, M., Li, B., Dang, M., Wang, Y., Zhang, B., Ren, H., & Xia, A. (2020). The formation of direct Z-scheme Ag/BiOCl/AgIO₃ heterojunction and its degradation stability. *Applied Surface Science*, 530, 147228. <https://doi.org/10.1016/j.apsusc.2020.147228>
- Zhang, G., Wang, Z., & Wu, J. (2021). Construction of a Z-scheme heterojunction for high-efficiency visible-light-driven photocatalytic CO₂ reduction. *Nanoscale*, 13(8), 4359–4389. <https://doi.org/10.1039/D0NR08442E>
- Zhang, J., Fu, J., Wang, Z., Cheng, B., Dai, K., & Ho, W. (2018). Direct Z-scheme porous g-C₃N₄/BiOI heterojunction for enhanced visible-light photocatalytic activity. *Journal of Alloys and Compounds*, 766, 841–850. <https://doi.org/10.1016/j.jallcom.2018.07.041>
- Zhang, J., Zhu, K., Zhu, Y., Qin, C., Liu, L., Liu, D., Wang, Y., Gan, W., Fu, X., & Hao, H. (2020). Enhanced photocatalytic degradation of tetracycline hydrochloride by Al-doped BiOCl microspheres under simulated sunlight irradiation. *Chemical Physics Letters*, 750, 137483. <https://doi.org/10.1016/j.cplett.2020.137483>
- Zhang, S., Zhao, F., Yasin, G., Dong, Y., Zhao, J., Guo, Y., Tsiakaras, P., & Zhao, J. (2023). Efficient photocatalytic hydrogen evolution: Linkage units engineering in triazine-based conjugated porous polymers. *Journal of Colloid and Interface Science*, 637, 41–54. <https://doi.org/10.1016/j.jcis.2023.01.066>
- Zhang, T., Qing, D., Jiang, Z., Xu, L., Liu, C., Yang, Z., & Huang, G. (2022). Reduced graphene oxide modified BiOCl/Co-doped SrFe₁₂O₁₉ composite for photocatalytic degradation of Rhodamine B. *Optical Materials*, 129, 112547. <https://doi.org/10.1016/j.optmat.2022.112547>

- Zhao, W., She, T., Zhang, J., Wang, G., Zhang, S., Wei, W., Yang, G., Zhang, L., Xia, D., Cheng, Z., Huang, H., & Leung, D. Y. C. (2021). A novel Z-scheme CeO₂/g-C₃N₄ heterojunction photocatalyst for degradation of Bisphenol A and hydrogen evolution and insight of the photocatalysis mechanism. *Journal of Materials Science & Technology*, 85, 18–29. <https://doi.org/10.1016/j.jmst.2020.12.064>
- Zhou, A., Liao, L., Wu, X., Yang, K., Li, C., Chen, W., & Xie, P. (2020). Fabrication of a Z-scheme nanocomposite photocatalyst for enhanced photocatalytic degradation of ibuprofen under visible light irradiation. *Separation and Purification Technology*, 250, 117241. <https://doi.org/10.1016/j.seppur.2020.117241>
- Zhu, D. and Zhou, Q. (2021) “Nitrogen doped G-C₃N₄ with the extremely narrow band gap for excellent photocatalytic activities under Visible light,” *Applied Catalysis B: Environmental*, 281, p. 119474. Available at: <https://doi.org/10.1016/j.apcatb.2020.119474>.
- Zhu, P., Wu, X., Chen, D., Zeng, Q., Cao, R., & Zhang, S. (2022). Z-type BiO–BiOCl/WO₃ heterojunction photocatalyst with SPR effect enhanced photocatalytic activity for the degradation of ciprofloxacin under visible light. *Optical Materials*, 132, 112844. <https://doi.org/10.1016/j.optmat.2022.112844>
- Zhu, Z., Zhong, W., Zhang, Y., Dong, P., Sun, S., Zhang, Y., & Li, X. (2021). Elucidating electrochemical intercalation mechanisms of biomass-derived hard carbon in sodium-/potassium-ion batteries. *Carbon Energy*, 3(4), 541–553. <https://doi.org/10.1002/cey2.111>
- Zia, J., & Riaz, U. (2020). Studies on the spectral, morphological and magnetic properties of PCz-PPy copolymer encapsulated BaFe₂O₄ nanohybrids. *Journal of Materials Science: Materials in Electronics*, 31(24), 22856–22865. <https://doi.org/10.1007/s10854-020-04812-7>

APPENDIX



Figure A1: *Vigna radiata* seeds germination in (a) distilled water (control), (b) untreated POME and (c) photocatalytically treated POME.

LIST OF PUBLICATION

- Lam, S.M., Yong, Z.J., Choong, M.K., Sin, J.C., Chin, Y.H., Tan, J.H., (2022) “Construction of MXene-Based Photocatalysts,” in *MXene-based photocatalysts: Fabrication and applications*. Boca Raton: CRC Press, Taylor & Francis Group, p. 33.
- Tan, J.H., Sin, J.C., Lam, S.M., Lin, H., Li, H.X., Huang, L.L., Mohamed, A.R., (2023) “Fabrication of novel Z-scheme BaFe₂O₄/BiOCl nanocomposite with promoted visible light photocatalytic palm oil mill effluent treatment and pathogens destruction,” *Inorganic Chemistry Communications*, 152, p. 110659. Available at: <https://doi.org/10.1016/j.inoche.2023.110659>.
- Tan, J.H., Sin, J.C., and Lam, S.M. (2021) “Synthesis of Z-scheme BiOCl/CuFe₂O₄ composite with enhanced visible light photodegradation of palm oil mill effluent,” *IOP Conference Series: Earth and Environmental Science*, 945(1), p. 012034. Available at: <https://doi.org/10.1088/1755-1315/945/1/012034>.